DEVELOPMENT OF AN ENCAPSULATION STRATEGY FOR AN IMPLANTABLE OPTICAL GLUCOSE SENSING TECHNOLOGY COMPATIBLE WITH A SELF-CLEANING MEMBRANE

A Dissertation

by

ALEXANDER ANIL ABRAHAM

Submitted to the Office of Graduate and Professional Studies of
Texas A&M University
in partial fulfillment of the requirements for the degree of

DOCTOR OF PHILOSOPHY

Chair of Committee,	Gerard L. Coté
Co-Chair of Committee,	Melissa A. Grunlan
Committee Members,	Michael J. McShane
	Michael V. Pishko
	Fred J. Clubb, Jr.
Head of Department,	Gerard L. Coté

May 2015

Major Subject: Biomedical Engineering

ABSTRACT

The concerning rate of diabetes mellitus prevalence and its associated chronic complications accentuates the urgency for continuous glucose monitoring. Optical techniques, especially fluorescence-affinity assays, offer a strategy that transcends current transcutaneous sensors by enabling subcutaneous implantation and interrogation. Biosensors can initiate an immune response that ultimately leads to a dense fibrous capsule surrounding the sensor. This biological interference, termed "biofouling," severely limits implantable sensor lifetimes by slowing analyte diffusion and decreasing optical signal propagation. In an effort to control biofouling, a thermoresponsive, "self-cleaning," hydrogel membrane based on poly(*N*-isopropylacrylamide) (PNIPAAm) has been proposed. Further, a continuous glucose monitoring system based on a competitive binding assay using Concanavalin A (ConA) as a component in a Förster resonance energy transfer (FRET) approach is being developed for encapsulation within the thermoresponsive hydrogel. In this research, a double network nanocomposite PNIPAAm (DNNC) hydrogel's glucose diffusion, thermosensitivity, cytocompatibility, *in vitro* cellular release, and *in vivo* compatibility and efficacy were thoroughly investigated. Further, an encapsulation strategy was developed for retaining the glucose assay within the hydrogel and yet allowing glucose diffusion. The methods and systems for obtaining the *in vitro* and *in vivo* results of the hydrogel are presented along with the glucose encapsulation strategies. In general, the research showed that the hydrogel could adequately diffuse glucose at temperatures associated with subcutaneous implantation, maintain a stable thermal cycling profile, promote cellular release without toxic effects

in vitro, and decrease the extent of biofouling *in vivo*. Furthermore, the hydrogel revealed its feasibility to be embedded with layer-by-layer (LbL) microsphere assemblies, which exhibited the ability to encapsulate the components of a competitive binding glucose assay. Overall, the results of this research demonstrate that the hydrogel combined with the encapsulated glucose assay is a promising approach for an implantable continuous glucose monitoring biosensor.

DEDICATION

A dissertation is not the outcome of the efforts from a sole individual,

but the collaboration of many:

To My Wife, Joy

Thank you for your radiating strength, love, and support that continuously inspires so that dreams may become a reality. I love you more.

Amor Vincit Omnia.

To Our Daughter, Evianna

The road of life is never without bumps and twists. Just remember, the harder the path is to walk, the more rewarding it will be in the end. I missed and thought of you every moment I was away. I love you more.

To My Dad, Mom, Justin, & Bluwin

Times in my life when I have felt inadequate, you have provided wisdom, love, and encouragement so that I may achieve success. I love you.

Per Angusta Ad Augusta.

To Charles, Mitzi, Christie, Hayes, Mckinley, Addison, & Brennan

Thank you for your enduring support, love, and care. I love you.

May the Lord bless you all.

ACKNOWLEDGEMENTS

I would like to thank my advisors, Dr. Coté and Dr. Grunlan, as well as my committee members, Dr. Clubb, Dr. McShane, and Dr. Pishko, for their guidance and support throughout the course of this research. In addition, I want to thank my friends and fellow lab mates, past and present, in the Optical Bio-Sensing Laboratory. Your constant source of levity and spunk have made this an exhilarating and frequently unpredictable journey. Furthermore, I would like to express my appreciation to Ryan Butcher, whose research dedication was absolutely impressive. I am notably grateful for the assistance of Andrea Locke, whose work ethic and chocolate addiction are nothing short of admirable, and to my roommate and friend, Tony Akl, for the never-ending source of jokes.

I also would like to thank my numerous sources of funding including the Department of Biomedical Engineering, the Dwight Look College of Engineering, the Center for Integration of Medicine and Innovative Technology (CIMIT), and the NIH/NIDDK (1R21DK082930-01A1) NIH/NIDDK (1R01DK095101-01A1).

Finally, it is imperative that I thank all my family and friends for the continuous support, for enduring various frustrating moments, and for generating countless joyful memories throughout my studies and my life. Thank you for *always* being there.

NOMENCLATURE

ADA	American Diabetes Association
APTS-MT	8-Aminopyrene-1,3,6-Trisulfonic Acid Trisodium Salt-Trimannose
BIS	*N*,*N*'-methylenebisacrylamide
BSA	Bovine Serum Albumin
CGM	Continuous Glucose Monitor
ConA	Concanavalin A
CTL	Cytotoxic T Lymphocytes
D_4	Octamethylcyclotetrasiloxane
D_4^{Vi}	1,3,5,7-Tetramethyl-1,3,5,7-Tetravinylcyclotetrasiloxane
Darocur 1173	2-Hydroxy-2-Methyl-1-Phenyl-1-Propanone
DBSA	Dodecylbenzenesulfonic Acid
DiI	Lipophilic Indocarbocyanine Dye
DI H_2O	Deionized Water
DMEM	Dulbecco's Modified Eagle's Medium
DN	Double Network
DNNC	Thermoresponsive Double Network Nanocomposite PNIPAAm
DP	Degree of PEGylation
DSC	Differential Scanning Calorimetry
EDTA	Ethylenediaminetetraacetic acid disodium salt dehydrate

FBR	Foreign Body Response
FGF	Fibroblast Growth Factor
Fn	Fibronectin
FRET	Förster Resonance Energy Transfer
GDH	Glucose Dehydrogenase
GDM	Gestational Diabetes Mellitus
GFP	Green Fluorescent Protein
GOx	Glucose Oxidase
HCl	Hydrochloric Acid
IDDM	Insulin Dependent Diabetes Mellitus
IL	Interleukin
NIDDM	Insulin/Non-Insulin Dependent Diabetes Mellitus
Irgacure 2959	1-[4-(2-Hydroxy)-Phenyl]-2-Hydroxy-2-Methyl-1-Propane-1-One
ISF	Interstitial Fluid
ISO	International Organization for Standardization
KCl	Potassium Chloride
KH_2PO_4	Potassium Phosphate-Monobasis
$K_2S_2O_8$	Potassium Persulfate
LbL	Layer-By-Layer
LDH	Lactate Dehydrogenase
MAC	Membrane Attach Complex
MADM	Methyl α-D-Mannopyranoside

MARD	Mean Absolute Relative Difference
mPEG-NHS(SC)	Monomethoxy-Poly(Ethylene Glycol)-N-Hydroxylsuccinimide(Succinimidyl Carbonate)
MWCO	Molecular Weight Cut-Off
NP	Nanoparticles
NaCl	Sodium Chloride
Na_2HPO_4	Sodium Phosphate-Dibasis
NaOH	Sodium Hydroxide
NCS	Newborn Calf Serum
NH_4OH	Ammonium Hydroxide
NIPAAm	*N*-isopropylacrylamide
NVP	*N*-vinylpyrrolidone
PAH	Poly(Allylamine Hydrochloride)
PAMP	Pathogen-Associated Molecular Patterns
PBS	Phosphate Buffered Saline
PEG-DA	Poly(ethylene glycol)diacrylate
PHEMA	Poly(Hydrocyethylmethacrylate)
PLA/PLGA	Poly(Lactic Acid)/Poly(Lactic co-Glycolic Acid)
PMN	Polymorphonuclear Neutrophilic Leukocytes
PNIPAAm	Poly(*N*-isopropylacrylamide)
PS	Polystyrene
PSS	Poly(Styrene Sulfonate)

PTFE	Poly(tetrafluoroethylene)
PVA	Poly(Vinyl Alcohol)
RT	Room Temperature
SMBG	Self-Monitoring Blood Glucose
SN	Single Network
SNNC	Thermoresponsive Single Network Nanocomposite PNIPAAm
T	Temperature
T_o	Initial Temperature
T_{max}	Peak Temperature
TGF-β	Transforming Growth Factor-β
TRITC	Tetramethylrhodamine Isothiocyanate
TNF-α	Tumor Necrosis Factor-α
USPTO	United States Patent and Trademark Office
UV	Ultraviolet
VPTT	Volume Phase Transition Temperature

TABLE OF CONTENTS

Page

LIST OF FIGURES

Page

LIST OF TABLES

Page

CHAPTER I

INTRODUCTION

1.1. Motivation

1.1.1. Diabetes Mellitus

Glucose is a monosaccharide, a simple sugar, which is the key carbohydrate in the human physiology. Its name stems from the Greek word “glykys,” meaning “sweet.” Its structure comes in two forms: D- and L-glucose. However, only D-glucose may be metabolized by mammalian cells, and thus hereinafter, the term “glucose” will refer to this biologically active D-isoform[1, 2].

Insulin is a central anabolic hormone produced by pancreatic islet beta cells and essential for glucose metabolism[2, 3]. The disease, diabetes mellitus, refers to a condition in which the body lacks the ability to produce or effectively utilize insulin that results in abnormal blood glucose concentrations. The word “diabetes,” a Greek conjugate of “dia” and “betes” that means “to go through,” was first composed by Araetus of Cappodocia (81-133 AD). It referred to the excessive urination, insatiable thirst, and tissue degradation experienced by those affected by the disease[4, 5]. The term “mellitus,” Latin for “honey,” was later added by Thomas Willis in 1675 to describe the sweet taste of urine and blood of its patients[4].

There are three subclasses of diabetes, type I (insulin dependent diabetes mellitus [IDDM]), type II (insulin/non-insulin dependent diabetes mellitus [I/NIDDM]), and

gestational diabetes mellitus (GDM). IDDM arises due to the obliteration of beta-cells in the pancreatic islets of Langerhans. This halts the production of insulin, and ultimately causes a patient to become hyperglycemic[2]. In order to survive, patients with type I diabetes require daily insulin injections. I/NIDDM stems from a combination of multiple disorders that include cellular insulin inefficiency, the inability of pancreatic cells to produce adequate insulin, and the failure of insulin to impede glucose fabrication within the liver[2]. Finally, GDM usually transpires during pregnancy, when numerous hormones emitted by a woman's placenta interferes with the body's normal response to insulin. This increased insulin resistance is usually compensated by placing the pancreas into overdrive to produce ample insulin, but occasionally, a woman's pancreas falls short causing an abnormally high blood glucose concentration[2].

1.1.2. Occurrence of Diabetes

The chronic and potentially debilitating disease, diabetes mellitus, was estimated by the Centers for Disease Control and Prevention (CDC) to affect roughly 29.1 million children and adults in the United States (i.e. 9.3% of the U.S. population) in 2012[6]. Globally, it is approximated that 381.8 million people between the ages of 20-79 have been diagnosed with diabetes in 2013 with an estimated projection of 591.9 million by 2035[7, 8]. **Figure 1.1.** conveys the extent of affected populations and their respective growth predictions[7, 8]. In high-income countries, the majority of people with diabetes are over the age of 50 (74%) while those in the low- to middle-income countries are predominantly under 50 (59%)[8]. As life expectancy increases, especially within

developing countries, rising trends within all income groups are expected. In essence, diabetes is escalating at an alarming rate and raising concerns within the health care industry.

According to the CDC, diabetes associated costs (direct and indirect) in the United States totaled USD 245 billion in 2012. It was further determined, upon adjusting for population age and gender differences, that the mean medical expenditures amid people diagnosed with diabetes were ~2.3 times higher than those without the disease[6]. **Figure 1.2.** exhibits international regional costs associated with diabetes mellitus for 2013 and future estimates[7, 8]. Unfortunately, Guariguata et al. fear that these predictions are underestimated as it depends on the accuracy of the estimated undiagnosed population[8]. The seriousness of this mounting epidemic has impelled the United Nations Resolutions on diabetes in 2006 to designate November 14th as World Diabetes Day in an effort "to raise public awareness of diabetes and related complications, as well as its prevention and care, including through education and the mass media"[9, 10].

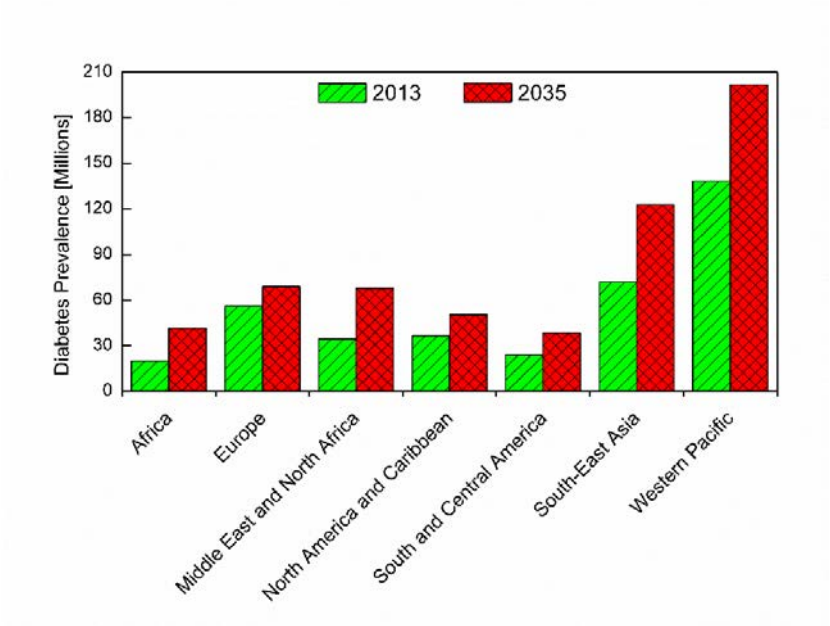

Figure 1.1. | Incidence of diabetes mellitus. Estimated prevalence of diabetes throughout the world in 2013 and projections for 2035[7, 8].

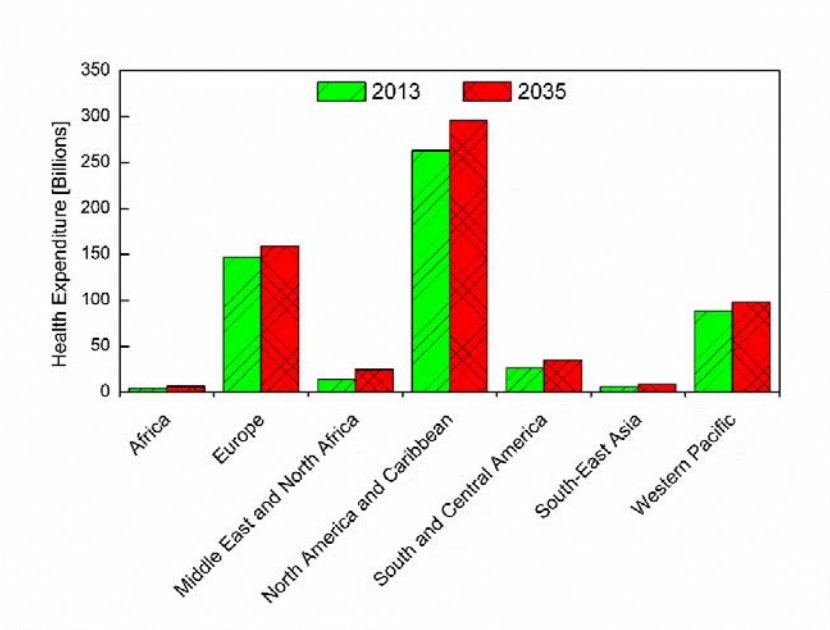

Figure 1.2. | Health care expenditure due to diabetes mellitus. Estimated current expenditures throughout international regions for 2013 and projections for 2035[7, 8].

1.1.3. Diabetes-related Complications

Uncontrolled glucose levels may cause adverse secondary complications to arise. As such, this disorder, along with its related complications, has been ranked the seventh leading cause of death in the United States as it claims over 72 thousand lives per year [6, 11]. Between 2009 and 2012, approximately 71% of adults with diabetes had elevated blood pressures (≥140/90 mmHg) and about 65% had high blood LDL cholesterol levels (≥100 mg dL^{-1})[6]. For this adult population, the hospitalization rate due to a heart attack or stroke is 1.5-1.8 times greater, and the cardiovascular disease death rate is 1.7 times higher[6]. Eye issues and potential blindness are also increased. An estimated 4.2 million adults with diabetes were diagnosed with diabetic retinopathy, a degradation to small blood vessels within the retina that may facilitate blindness[6]. Diabetes has also been listed as the leading source of kidney failure that accounted for 44% of all new cases in 2011[6]. In addition, it accounts for roughly 60% of all adult non-traumatic lower-limb amputations. Those diagnosed with diabetes may develop other complications such as neuropathy, non-alcoholic fatty liver disease, periodontal disease, hearing loss, erectile dysfunction, and depression. For woman, diabetes may also impact pregnancy as uncontrolled diabetes can cause birth defects and unplanned abortions[6]. The prevention of secondary complications is possible by preserving a narrow glycemic range (70-120 mg dL^{-1}), which may be accomplished by routine blood glucose monitoring[12-14].

1.1.4. Controlling Glucose Levels

The present standard and advocated point of care is the self-monitoring of one's blood glucose level. The results from the Diabetes Control and Complications Trial prove that the intensive management of blood sugar levels is an efficient process to avoid or at minimum, delay the onset of secondary diabetic complications[12-15].

The aim of DM therapy is to approximate the blood glucose profile of an individual and control its concentration to near-normal levels. Without proper regulation, a patient could fall victim to hypoglycemia, a condition where the blood glucose level falls significantly below the normal physiological range, which may place the patient in a coma and ultimately death. Its opposing condition, hyperglycemia, occurs when the blood glucose level rises substantially above normal levels. If left unsupervised and untreated, a prolonged, irregular high blood glucose level may cause long-term complications such as neuropathy, retinopathy, nephropathy, cardiovascular disease as well as death. The appropriate treatment of DM is near-constant monitoring of blood glucose levels (more than four times per day) so that insulin, food, and exercise levels may be adjusted. As such, well-regulated blood sugar levels have shown to significantly lessen secondary complications and slow the advancement of DM. Presently, the most common and commercially available methods for glucose-sensing are founded upon electrochemical or colorimetric designs. These techniques require pricking of a finger with a lancet to obtain a blood droplet anywhere between 0.6 µL to 10 µL in volume[2, 16].

1.1.5. Self-monitoring Glucose Instruments

The blood glucose-sensing market has been growing a rapid rate over the last decade. Presently, there are over 80 commercially available self-monitoring blood glucose (SMBG) meters[15, 17]. Although the market is highly competitive, Abbott Laboratories, Roche Diagnostics, Johnson & Johnson's LifeScan, and Bayer AG represent the majority[15]. The vast majority of glucometers rely on an enzymatic assay that converts glucose into a quantifiable end product, a process first described in 1962 by Clark and Lyons[18]. The prevailing enzymes (e.g. glucose dehydrogenase [GDH] and glucose oxidase [GOx]) encompass redox groups that alter the redox state amidst the reaction. These type of sensors are categorized as amperometric systems as they assess electrical current streaming from an oxidative reaction at a charged electrode to a reduction reaction at an adjacent electrode. For instance, GOx may be adhered to an electrode where it will catalyze the conversion of glucose into gluconolactone and hydrogen peroxide. As hydrogen peroxide interacts with the electrode, a measurable electrical current is produced. Essentially, a modification in the current flow, triggered by a change in the oxidation of glucose and the enzyme catalyzed production of hydrogen peroxide, will impart a similar adjustment in the glucose concentration[19, 20].

Notably, environmental elements (e.g. altitude, temperature, and humidity) and internal, biological interferens (e.g. vitamin C, hematocrit, glutathione, and uric acid) may affect the reported results since these tests transpire *ex vivo*[21]. In addition, the self-monitoring analytical quality may not meet the American Diabetes Association (ADA) error standards when executed by a patient rather than a trained specialist[22]. Although

the ADA has previously stated that SMBG devices should contain less than ±10% error, the FDA allows for ±20%[22, 23]. In 2013, the International Organization for Standardization (ISO) announced its intentions to implement a revised blood glucose meter standard (ISO 15197:2013) for which mandatory compliance will be recommended in 2016. Essentially, this revised standard will demand enhanced accuracy and precision as 95% of results ≥100 $mg \cdot dL^{-1}$ must fall within ±15% of the actual blood glucose concentration and 95% of results <100 $mg \cdot dL^{-1}$ must reside within ±15 $mg \cdot dL^{-1}$ of the reference glucose level. Furthermore, 99% of all the results must be within zones A and B of the consensus error grid[24, 25].

A primary disadvantage of present SMBG devices is that they require a blood sample. Regardless of where on the body this is obtained, this tactic is not only cumbersome and time-consuming, but research has shown that patients are often fearful of self-testing[26]. This fear, in combination with the inability to fully understand the implications of their glycemic results, leads to infrequent testing of a patient's blood glucose level and the failure to commit to an effective DM therapy regiment[15]. According to the ADA, SMBG testing frequency should be molded by the particular needs and goals of a patient. However, generally-speaking, this should be roughly 6-8 tests per day[23]. Although the associated cost of testing if often cited as a main prohibitive hurdle, the inconvenience and obstruction of a patient's lifestyle may be a more influential factor that limits testing frequency[27, 28]. Regardless, even when testing 6-8 times per day, this still only provides intermittent readings of continuously changing blood sugar levels[29].

1.2. Continuous Glucose-sensing

1.2.1. Advantages of Continuous Glucose-sensing

There exists numerous advantages for the use of continuous glucose monitoring (CGM) systems. Although, the key reason is the ability to maintain euglycemia. It is well documented that increased SMBG is associated with improved glycemic control, and therefore, a better quality of life[5, 12-15, 30]. In 2005, a clinical study proved that even with nine SMBG measurements per day, patients still spent an average of 2.1 h in hypoglycemia (<70 mg·dL^{-1}) and 4.8 h in hyperglycemia (>180 mg·dL^{-1})[31]. Thus, CGM has the potential to minimize a patient's time spent in either of these physiological states, but especially within the hypoglycemic phase that often occurs when sleeping. It also may decrease hemoglobin A1c (HbA_{1c}) values, which bestow a statistical glucose concentration mean spanning 2-4 weeks and a measure to the degree of risk for glycemic damage to tissues[32-36]. Outfitting alarms to CGM devices may further enhance patient awareness of their blood glucose levels, providing alerts before their condition becomes critical.

With the intention to establish a "closed-looped" system, current CGM devices have been paired with external insulin pumps to automatically maintain euglycemia – thereby, imitating the function of a pancreas. As the CGM quantifies one's blood glucose concentration, the information is relayed to an external insulin pump that implements an algorithm to inject the appropriate amount of insulin based on the

patient's physique. This advanced form of an artificial pancreas has proven to better control glycemic levels in comparison to conventional insulin pump therapy[30].

1.2.2. Transcutaneous Monitors

The first CGM apparatus to be approved for use within the United States as a trending monitor was procured by Medtronic in 2001. Medtronic's latest CGM system, Guardian® REAL-Time, is designed based on amperometry that provides real-time glucose measurements. This sensor relays glucose quantities a patient's interstitial fluid (ISF) every 5 minutes and has the ability to save measurement information to review and analyze. In order for this device to operate at its full potential, it requires recalibration using a standard "finger-prick" blood glucose measurement 2-4 times daily[19, 37-39]. In addition, its lifetime is only 72 hours.

The DexCom™ G4 Platinum CGM by DexCom, Inc. is yet another amperometric-based device that was initially FDA approved in 2006 for use as an appendage to standard "finger-prick" blood glucose measurements. This apparatus includes a small insertable or implantable sensor that aims to quantify glucose within subcutaneous tissue with a lifetime of 7 days. In addition, recalibration was reduced to every once every 12 hours on average with a mean absolute relative difference (MARD) of 9%[2, 19]. Although this CGM has improved sensor lifetime and device management, it still has only been approved as an adjunct to finger stick tests. Thus, any user cannot exclusively rely on the DexCom™ CGM calculated glucose concentrations.

Finally, the FreeStyle Navigator® Continuous Glucose Monitoring System by Abbott Diabetes Care was FDA approved as a certified CGM in 2008. In August 2011, however, the device was discontinued by the FDA due to supply complications that obstructed Abbott Diabetes Care from selling new units or replacing parts of units still under warranty (i.e. quality control). The company, for the time being, has decided to discontinue the FreeStyle Navigator® Continuous Glucose Monitoring System from the U.S. market. It, although, remains available in seven international markets[40, 41]. Regardless, this three-electrode amperometric sensor may be positioned within the subcutaneous adipose tissue for only up to 5 days. However, glucose levels are not reported until approximately 10 hours post insertion as calibration is necessary after 10, 12, 34, and 72 hours. The FreeStyle Navigator® thereby requires fewer calibrations compared to its competitors (Medtronic Guardian® REAL-Time and DexCom™ G4 Platinum)[19, 42]. Recently, Abbott Diabetes Care has announced its the FreeStyle® Libre Flash Glucose Monitoring System for release in European markets. This advanced CGM system requires no "finger-prick" calibrations and lasts up to 14 days. The new CGM system is still amperometric-based, but the precision and accuracy of the manufactured sensors are incredibly stable, which enables minimal variation over the 2 week sensor lifetime and between sensors.

These subcutaneous, GOx-based sensors are transdermally inserted beneath the patient's skin using a trocar-like instrument to generate real-time glucose measurements in the ISF[19, 43]. Since the glucose concentration within the ISF can lag behind blood glucose from 10-15 minutes (may be translated to discrepancies from 30-45 $mg \cdot dL^{-1}$), all

ISF techniques have the potential to have time correlation differences, which need to be considered in any standard of care for diabetic patients[44-47]. However, CGM system accuracy relies heavily on its calibration, which converts the amperometric shifts into a glucose value. This assumes that the plasma to ISF ratio remains fairly constant, which fails to be the case if calibration occurs during swift plasma glucose changes. As glucose sensors may lag 5-10 min during rapid glycemic fluctuations, the key effect on lag is the introduction of error during calibration that may impair long-term CGM performance[21, 48]. Thus, the average percentage of error for CGM devices is approximately 15%[48, 49]. Though these devices demonstrate the potential to attain tighter glycemic control and diminish hypo- and hyperglycemic incidents, there still exists numerous obstacles to conquer in order to improve the sensor's accuracy, precision, and lifetime.

1.2.3. Optical Measuring Approaches

The most enticing benefit of an optical technique is its potential for non-invasive or, at the very least, minimally-invasive sensing to quantify blood glucose concentrations. To this field, an enormous research effort has been implemented as evident by the number of United States patents filed. Since 1976, a total of 4,194 non-invasive/noninvasive/minimal optic glucose patents have been released by the United States Patent and Trademark Office (USPTO) – a number that continues to rise each year[50]. The aforementioned research effort has explored a variety of methods including thermal gradient spectroscopy, polarimetry, Raman spectroscopy, fluorescence spectroscopy, kromoscopy, optical coherence tomography, optoacoustic techniques,

infrared absorption, and near-infrared scattering to successfully measure glycemic levels with accuracy, precision, and longevity[2, 5, 51]. Unfortunately at the present, not one of these techniques is available for commercial use.

Fluorescence-based glucose-sensing offers one potential scheme to accomplish continuous readings. Such a sensor may be intradermally implanted and optically interrogated non-invasively using an external, mobile device. An intradermally implanted sensor would decrease the risk of a chronic infection, which is commonly associated with all present transcutaneous CGM systems (refer to Section 1.2.2.). Furthermore, complete submersion in the ISF may decrease the sensing lag time, and therefore could enhance blood glucose accuracy. Fluorescence describes the phenomenon in which an excited molecule (i.e. a molecule residing in an excited state) releases energy (i.e. photons). As demonstrated in **Figure 1.3.**, the process begins with a fluorescent molecule in its ground state, S_0. As incoming energy (i.e. light source) is absorbed by the fluorescent molecule, it rises to an excited energy state, S_1. When the molecules begin to relax, its vibrational state is lowered via internal conversion. Energy may now be freed in the form of fluorescence (spontaneous photon emission of a longer wavelength) or through a non-radiative pathway (e.g. scattering, quenching, heat) that returns the molecule to S_0[2, 5, 52].

One specific fluorescence method that continues to be utilized for glucose-sensing is Förster Resonance Energy Transfer (FRET). FRET is the non-radiative transfer of excited-state energy between two fluorophores, a donor (D) and an acceptor (A), in close proximity to each other. The energy transfer occurs due to dipole-dipole

interactions between the donor and acceptor molecules, which reduces the fluorescence of the donor when both fluorophores are between 20 and 70 Å apart[53, 54]. Therefore, when D and A are physically close, energy transfer from D to A occurs, and results in a smaller donor emission. However, as D and A move apart, approximately beyond 70 Å, the energy transfer does not transpire, and thus, the donor emission intensity will rise. Now, the energy transfer rate is contingent upon the degree of spectral overlap between the donor emission with the acceptor absorption, the donor quantum yield, the donor and acceptor transition dipole relative orientation, and the physical distance between D and A[2, 5, 52]. Using the following equation, the energy transfer rate, k_T, may be determined:

$$k_T = \frac{1}{\tau_D}\left(\frac{R_0}{r}\right)^6$$

where τ_D is the donor decay time without the acceptor present, R_0 is the Förster distance when k_T is only 50% efficient, and r is the donor-to-acceptor distance. The energy transfer efficiency (E), the fraction of photons absorbed by D that are transferred to A (i.e. the ratio of the transfer rate to total decay rate), may be calculated by:

$$E = \frac{R_0^6}{R_0^6 + r^6}$$

This relationship is demonstrated in **Figure 1.4.**, where it is apparent that a decrease in intermolecular distance is associated with a swift increase in energy transfer efficiency. This principle affiliation has been well researched and executed for the purpose of glucose-sensing[54-56]. Through the proper chemistry arrangement, the donor-to-acceptor distance widens when glucose enters the FRET system. Since k_T is inversely

proportional to r^6, the fluorescence intensity will also increase proportionally, and thereby provides a method to measure glucose concentrations.

Since glucose is not fluorescent, exogenous reagents are therefore necessary to implement a FRET glucose-sensing system. These reagents will require direct contact with biological fluid. As mentioned earlier, subcutaneous placement has its advantages for continuous sensing. However, the reagent encapsulating material must encompass properties that enhance its biocompatibility in order to minimize the host's immune reaction – a reaction that could substantially decrease the sensor's lifetime.

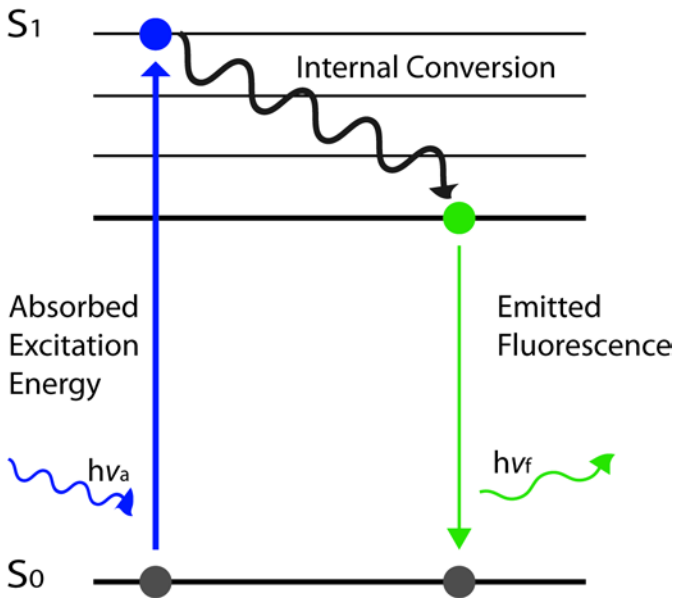

Figure 1.3. | Jablonski diagram. An energy diagram conveying the energy, electronic states of a molecule, its transitions, and release of photon energy as fluorescence[52].

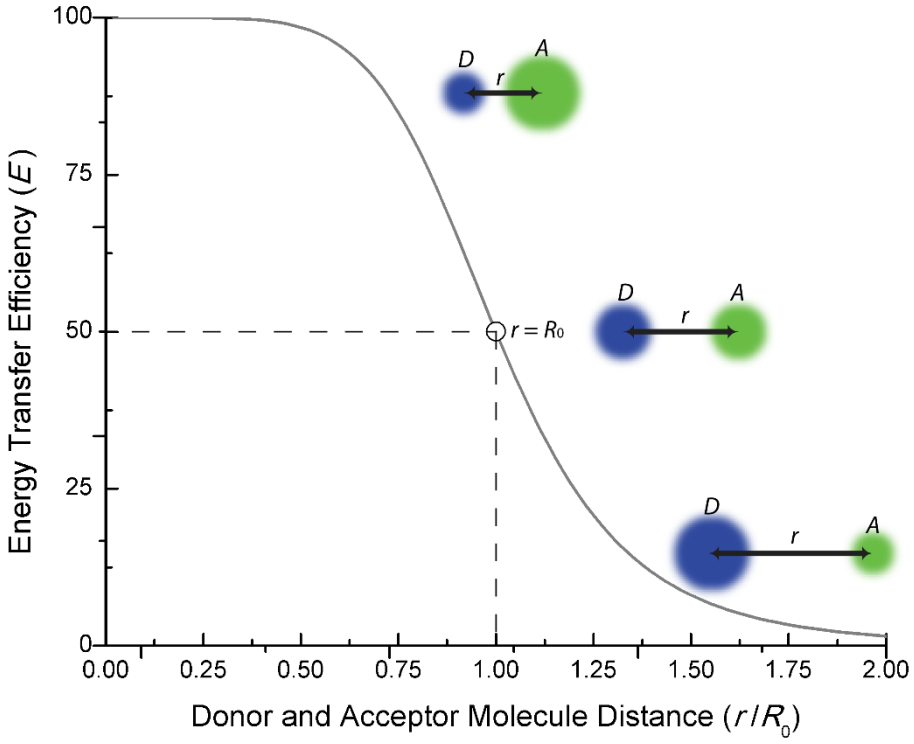

Figure 1.4. | Distance-dependent energy transfer efficiency. A graphical representation exhibiting the energy transfer efficiency dependency on the intermolecular distance, r, to Förster distance ratio for a pair of fluorescent molecules[2].

1.3. The Host Immune Response & Biofouling

1.3.1. The Immune System

The human immune system encompasses two primary components: the innate and the adaptive. The innate immune system serves two main purposes. First, it acts as the initial response to microbes or antigens in order to prevent, control, or eliminate

infection(s) to the body. Secondly, it functions as a stimulus to the adaptive immune system so that the nature of the adaptive response is more efficient against specific types of microbes. The main elements of the innate immune system include polymorphonuclear neutrophilic leukocytes (PMN), macrophages, and natural killer (NK) cells. The pattern recognition receptors among the cells within the innate immune system is fairly limited (~10^3) since these receptors are encoded within the germline DNA. Therefore, any foreign antigens or microbes that present pathogen-associated molecular patterns (PAMPs) that are unrecognized by the innate system will be addressed by the adaptive immune system. The adaptive immune system is the second and last line of defense, but is capable of recognizing ~10^7 or more PAMPs. This system is also vastly more complex in comparison to the innate. The major factors that encompass the adaptive immune system include antigen-specific lymphocytes (T and B lymphocytes), professional antigen-presenting cells (i.e. dendritic cells), and effector cells (i.e. $CD4^+$ helper T lymphocytes, $CD8^+$ cytotoxic T lymphocytes)[57]. A fundamental aspect to understand is that many of the molecules that play a part in the innate system are also, in some way, associated with adaptive immune system. This bridges the gap between the two systems and thus, allows for a continuous immune response.

1.3.2. Host Response to Implanted Foreign Materials

Once a foreign material has been implanted, the host will elicit an immune response due to the foreign material itself as well as the introduction of any pathogens implemented during the implantation procedure. Penetration of the epithelium induces

localized inflammation that stems from the damage incurred and/or the activation of tissue mast cells. The degranulation of mast cell vasoactive amines, histamines, and serotonin, produces a localized increase in blood flow and capillary permeability that results in the discharge of plasma proteins and the migration of PMNs to the implantation site[58].

PMNs are considered to be the first line phagocytic defense against extracellular pathogens as they are the most abundant population of circulating white blood cells. Once having migrated to the implantation site, PMNs will begin to kill microbes non-specifically. These particular cells are the "kamikaze" cells of the immune response. In other words, PMNs kill themselves in the process of destroying microbes. In addition, defensins (small cationic peptides that contain three intrachain disulfide bonds) that are produced by epithelial cells, neutrophils (PMNs), NK cells, and $CD8^+$ cytotoxic T lymphocytes, play a proactive role in direct toxicity to microbes and the activation of other cells involved in the inflammatory response[57]. Now, since the alternative pathway of the complement system can be activated by the binding of C3b to the walls a present microbe, the activation of this system can produce additional inflammatory mediators due to the release of C3a and C5a. C5a further stimulates PMNs to migrate to the site of the implantation. In addition, C3b can opsonize pathogens so that they may be easily phagocytosed and destroyed[58]. The activation of the complement system, however, depends on a continuous low-level breakdown of C3. If the C3b element of C3 binds to a self-cell, regulatory mechanisms within that cell will deactivate it, but if C3b binds to a microbe, Factor B is activated, and its cleavage product Bb will bind to C3b. The C3bBb

complex stimulates the breakdown of C3 to C3b. Furthermore, C3b aids in cleaving C5 into C5a and C5b, which have crucial immunological functions: C5a facilitates inflammation while C5b is a vital factor for the assembly of the “membrane attack complex” (MAC). Now although PMNs are usually the first to respond to the implantation site, they are soon followed by monocytes, NK cells, and eventually T and B lymphocytes[58, 59].

The mononuclear phagocyte system is widely known for its development of macrophages. The development of a macrophage begins as a stem cell that matures to a monoblast within the bone marrow. Once it leaves the bone marrow and enters the blood stream, it is referred to as a monocyte. Finally, monocytes will fully mature into macrophages when they are activated. The main cytokine that evokes macrophage activation is IFN-gamma. IFN-gamma is produced in a variety of different ways, but most noticeably by NK cells and T cells. Furthermore, IFN-gamma increases the expression of Fc receptors for IgG on macrophages and PMNs. It also increases the expression of MHC Class II. The enhanced expression augments the phagocytic functions of these cells along with improving the abilities of professional antigen-presenting cells[59, 60]. Now, macrophages, unlike PMNs, survive for longer periods at the site of implantation since they are not terminally differentiated and encompass the ability to undergo cellular division while at the implant site. Furthermore, macrophages secrete other cytokines such as TNF-alpha (which increases inflammation) and IL-12 (which activates NK cells)[57]. Natural killer cells (NK cells), although categorized as a lymphocyte, have the ability to terminate numerous target cells without acquiring any

additional activation. These cells recognize infected or stressed cells and react by killing them. NK cells also possess an Fc receptor for IgG, which allows them to contribute in antibody-dependent cell-mediated cytotoxicity. This line of defense functions before specific cytotoxic T lymphocytes (CTLs) can be either recruited or activated[58].

The purpose of CTLs is to terminate infected cells much like NK cells or macrophages. CTLs, however, operate through a network of various elements within the adaptive immune system, and therefore, are antigen-specific. The development of CTLs begins with a professional antigen-presenting cell (APC), such as a dendritic cell, recognizing and ingesting a foreign antigen. Once ingested, the APC will migrate to lymph nodes, where it will exhibit the antigen to T cells residing in the parafollicular zones. Now, MHC Class I molecules will present peptides to and that are recognized by $CD8^+$ T cells, while MHC Class II molecules display peptides to $CD4^+$ T cells. If the APC exhibits the antigen to a T cell in the presence of a B7 costimulator, it will enable the differentiation of the T cell into a CTL. Furthermore, cross-presentation could potentially transpire, where the APC binds to both a $CD8^+$ cytotoxic T lymphocyte and a $CD4^+$ helper T lymphocyte. For this particular situation the $CD4^+$ helper T lymphocyte will secrete cytokines that enable a second signal for CTL assembly[57].

At this point, any pathogens (besides the actual medical device) that were introduced during the implantation process should hopefully have been addressed. Furthermore, to quicken and enhance the immune response to subsequent exposures to similar antigens, memory B and T cells may have been produced through antigen stimulation of naïve lymphocytes. In regards to the implanted medical device, the host's

immune system will ultimately determine that the foreign material and its elements may not be phagocytosed or destroyed. Therefore, the upsurge of macrophages, which are capable of expressing fibronectin along with other various growth factors (e.g. bFGF, TGF-β), will eventually result in the recruitment of fibroblast cells and the development of a fibrous extracellular matrix. The deliverance of these elements plays a key role in the activation of angiogenesis and fibroplasia. More specifically, fibroblast growth factor (bFGF) and transforming growth factor-β (TGF-β) bind to proteoglycans in the progression of the extracellular matrix of collagen formed by fibroblast cells[61-63]. Furthermore, any prolonged inflammation may be problematic with respect to biocompatibility as it increases the potential and severity of a fibrous capsule (i.e. biofouling).

1.3.3. Biocompatibility

The most agreed upon definition of "biocompatibility," also known as the "Williams' definition," was defined in the European Society of Biomaterials Consensus Conference as: "the ability of a material to perform with an appropriate host response in a specific application"[64]. Although this definition is practical, it lacks the perception as to a degree of biocompatibility and fails to offer a foundation of which the biocompatibility of materials could be enhanced[65]. By this definition, material biocompatibility is gauged by its intention at a specific locale. Furthermore, while the definition accounts for "appropriate" effects of the biomaterial on the host, the host's

response on the material must also be reflected in order to lessen the development of health issues and device failure rates[66].

For the purpose of an analytical biosensor, biofouling and especially eventual fibrous formation has the ability to reduce, potentially significantly, the diffusion and perfusion of the target analyte. Such action will result in a decreased sensor response, increased sensor lag time, and diminished accuracy of true blood concentrations[67-69]. The accuracy could be further reduced as the increased local cellular presence, residing in a hypermetabolic state, may alter the analytical (i.e. glucose) concentrations[70]. However, Novak *et al*. disagree. Upon conducting a computation model to the relative impact of capsular tissue effects on lag time and signal attenuation for a glucose-sensor, they determined that the cellular (primarily macrophages) metabolic activity and the capsule diffusion coefficient had minimal to no impact on the modes of sensor failure. Rather, fibrous capsule thickness attributed to longer sensor lag times, and sensor attenuation was predominantly affected by deviations in vessel density and capsule porosity[71]. Nonetheless, cellular proliferation surrounding an optically-based sensor will cause signal reduction due to increased light scattering and absorption. Eventually, this will lead to a sensor failure. To curtail the extent of biofouling, and thereby its effects on an implanted biosensor, the general approach implements a combination of specific material chemistries and microarchitectures.

1.3.4. Key Properties Associated with Biofouling Reduction

An engineered material that controls biofouling is essential to the development of a long-term transdermal or subcutaneously implanted CGM. Designing materials to diminish the degree of biofouling is an interdisciplinary field that combines facets of materials, physiological systems, and cells. It has been shown that surface topography and chemistry (e.g. hydrophobicity, softness and stiffness, roughness, charge) and material microstructure (e.g. porosity, pore size, crosslink density) actuate protein and cellular behaviors[72, 73].

Upon insertion of a foreign material into a host, it has been observed that a similar foreign body reaction occurs independent of the material's surface chemistry. This phenomenon has been attributed to the nonspecific adsorption of proteins, also known as the Vroman effect[72, 74-76]. In 1969, Leo Vroman and Ann Adams first verified that blood plasma proteins adsorption comprises intricate sequences of adsorption and displacement[77, 78]. This effect exhibits an initial adsorption of plentiful, but weakly surface-active proteins (e.g. albumin), which are subsequently dislocated by more robust binding proteins present at a lesser concentration in plasma (e.g. fibrinogen, fibronectin)[79]. More importantly, surface protein adhesion mediates cellular attachment and conducts cellular signals, primarily through integrins[72]. Typically, materials with the following properties have been considered more resistant to proteins: (a) hydrophilic, (b) neutral charge, (c) hydrogen bond acceptor presence, and (d) absence of hydrogen bond donors[80, 81].

Biomaterial hydrophobicity, a property commonly quantified through the contact angle spread of a water droplet on its surface, has been reported as a cell adhesion mediator. The lower the contact angle, the more hydrophilic the material. Contact angles less than 90° are usually considered hydrophilic. Generally, hydrophobic surfaces are regarded as more prone to protein adsorption than hydrophilic due to resilient hydrophobic interactions as opposed to the repulsive solvation effects that occur as a result of strongly bound water molecules[80, 82-84]. Tamada and Ikada demonstrated that maximum protein adsorption arises with a contact angle between 60-100° with either bovine serum albumin (BSA), bovine γ-globulin (IgG), or plasma fibronectin (Fn)[85]. Their results indicate that protein adhesion is favored on hydrophobic surfaces, where hydrophobicity does not necessarily guarantee protein adsorption or the lack there of as there is a dependency on the specific type of protein and/or the particular cell line. Since proteins contain both polar and non-polar residues and depending on their structure, there is potential that any one protein may adhere to a surface regardless of its hydrophobicity[86]. It has also been concluded that given enough time, protein adsorption will increase[84]. Regarding cellular adhesion variability with hydrophobicity, Wei *et al*. witnessed an increase in osteoblast attachment and dispersion as the contact angle was decreased from 106° to 0°[87]. In contrast, Tamada and Ikada reported that fibroblast adhesion improved as the contact angle increased, and peaked at approximately 70°[85]. Ultimately, the optimal material wettability will be contingent on its implant location and specific purpose. However, besides protein polarity, electrostatic charges and their

associated surface functional groups are another common adsorption control mechanism to consider in the material scaffold design.

Biomaterial surface functional groups and their related charges are known to directly affect the material's biocompatibility. Of these groups, the most commonly investigated for protein-biomaterial interactions are carboxyl (-COOH), hydroxyl (-OH), methyl ($-CH_3$), and amine ($-NH_2$). Carboxyl groups convey a negative surface charge, which research has demonstrated to effortlessly deflect proteins, such as fibronectin and albumin[81, 88, 89]. Interestingly, -COOH functionalized surfaces have also exhibited increased cellular growth. However, Ohya *et al*. reported that this effect results from a dependence of carboxyl density[90]. As the density increased, and thereby increased the negative charge, cellular growth was further inhibited. A study by Jung *et al*. also noticed that charge density affected the extent of cellular proliferation[91]. However, rather than a negative charge, Jung et al. saw an increase in surface cell attachment as the positive charge density was increased[91, 92]. Now, the hydroxyl group denotes a neutrally charged, hydrophilic surface. Therefore suggesting that it displays a low protein affinity. According to Lestelius *et al*., that is true. Their group noticed a reduction in plasma protein adsorption on hydroxyl-functionalized self-assembled monolayers[93]. Contrary to this outcome, Fn adsorbed on hydroxyl groups lead to an increase in cell growth and adhesion strength in comparison to methyl functional groups[88]. Methyl functional groups are hydrophobic in nature, and as such, are generally considered to encourage protein adsorption. Fibrinogen, IgG, and albumin have all demonstrated maximum adhesion strength to methyl groups[93, 94]. Similar to methyl, amine groups represent a positive

charge that has shown support for protein adhesion. Fibronectin appears to bind particularly well to amine-functionalized surfaces, and thus, enhances the adhesion, growth, and matrix formation of endothelial and fibroblast cells[88, 95-97]. Essentially, methyl and amine surface groups are apt to tightly bind proteins, which tends to foster cell attachment. Therefore, these two functional groups will probably trigger an undesirable immune reaction.

Material stiffness and surface topography are properties that literature has shown to affect biological responses. Blakney et al. witnessed a change in macrophage morphology and cytoskeletal organization from round to spread as PEG-DA hydrogel stiffness was increased[98]. Their findings suggested that macrophages were less sensitive to softer hydrogels, possibly due to integrin-mediated phenomenon, and that the round morphology with no apparent cytoskeletal arrangement reduced their activation; thereby, decreasing tumor necrosis factor-alpha (TNF-α), interleukin-1beta (IL-1β), and interleukin-6 (IL-6) expression, and forming a thinner surrounding fibrous layer in vivo. These findings correlate with Kim *et al.*, who exhibited diminished human mammary epithelial cellular stretching when their nude dendrimer immobilized polystyrene material surface roughness was increased beyond 4 nm[72, 99], and Dalby, who witnessed decreased F-actin filaments in fibroblasts with increasing surface roughness[100]. A round cellular morphology resulted in each case.

Now, porous (i.e. pore size and porosity density) implantable biomaterials have demonstrated to result in a loose, dis-organized fibrous capsule[101, 102]. In contrast, non-porous biomaterial implants appear more apt to development dense, well-organized,

fibrous shells. Interestingly, porous materials also saw increased vascularization surrounding the implant[101, 103]. Present research has probed implant porosity optimization to curtail the FBR, which appears to indicate that 30~60 μm pore diameters evoke the thinnest fibrous capsules while driving the most extensive level of neovascularization[102, 104-106].

Nano- and micro-scale structures are capable of stimulating and/or dampening various aspects of cellular adhesion by influencing its morphology, gene expression, motility, and differentiation[72, 99, 107]. Research has revealed that the resulting biological response of this property along with the others aforementioned is highly dependent on the type of proteins and cells it interacts with. This stresses the importance to understand the local environment and the intended role of the biomaterial being implanted. Once "tuned", the biomaterial properties may aid to mitigate cell adhesion and thus, lessen the extent of biofouling.

1.3.5. Biomaterials: The Next Generation in Anti-Biofouling

A variety of new materials have been investigated to improve the control of biofouling. The majority of these materials may be categorized as natural, synthetic, or semi-synthetic. Natural materials such as collagen[108, 109], alginate[110], dextran[111], hyaluronan[112], and chitosan[113, 114], provide the benefit of exhibiting similar macromolecular properties that are recognized metabolically. As such, these materials elicit a lessened immunological response. However, the use of these materials is not without its disadvantages including high immunogenic frequency, decomposition, and

normal, natural macromolecular inconsistency[76]. To overcome these limiting obstacles, various synthetic hydrogel materials were developed (e.g. poly(vinyl alcohol) (PVA)[102, 115], poly(lactic acid)/poly(lactic co-glycolic acid) (PLA/PLGA)[116, 117], poly(ethylene glycol)diacrylate (PEG-DA)[63, 118], poly(hydrocyethylmethacrylate) (PHEMA)[119, 120], poly(tetrafluoroethylene) (PTFE)[101, 102, 115, 121], and poly(*N*-isopropylacrylamide) (PNIPAAm)[122-125]). Hydrogels are insoluble, crosslinked, three-dimensional polymer networks that swell in aqueous mediums and can appear similar to the highly hydrated physique of natural tissues. Their permeability may be tailored for the diffusion of analytes, making them wonderful candidates for tissue engineering, drug delivery, or bio-sensors. However, they too have their own drawbacks. Many hydrogels lack the mechanical robustness for certain applications and, more importantly, have demonstrated biocompatibility issues[76, 126, 127]. In an attempt to address these issues, a new generation of "smart" biomaterials is being explored. Generally, these materials experience reversible conformational or phase transitions as a response to specific aspects in their local environment (e.g. pH, temperature, light, ions, analytes, electric fields, pressure)[128-135]. This characteristic is especially attractive for *in vivo* applications (e.g. drug release, bio-sensing) to enhance the parameter control of cell adhesion.

To encourage a reduced FBR, some researchers have focused "smart" biomaterials to either control the inflammatory response chemically or diminish non-specific protein adsorption. For chemical control, drug releasing polymer systems have employed steroidal (corticosteroid, glucocorticoids) anti-inflammatory drugs (e.g. dexamethasone[136]) as they possess the ability to downgrade or inhibit the formation or

secretion of inflammatory mediators like leukotrienes and prostaglandrins. Thus, reducing the FBR locally to the implant[76, 137]. In order to promote angiogenesis for increased blood-analyte concentration, growth factors (e.g. vascular endothelial growth factor [VEGF]) have been implemented concurrently[138]. Regardless, this technique only controls the immune response for a short period of time, essentially based on the polymer's reservoir. Therefore, for long-term analyte sensing, this method is not ideal. In comparison, zwitterionic, net neutral molecules with positive and negative charges, materials such as carboxybetaine, sulfobetaine, and phosphorylcholine, have recently shown to create an ultra-low biofouling hydrogel. Zhang *et al*. demonstrated that this hydrogel has the ability to resist fibrous encapsulation for at least three months *in vivo* while promoting neovascularization[139]. Although encouraging, temperature responsive hydrogels represent another novel approach.

1.3.6. "Self-cleaning" Membrane

Thermoresponsive, crosslinked hydrogels possess the ability to alter their hydrophobicity with complete reversibility. In essence, the properties of these hydrogels allow them to switch from a relatively hydrophilic, swollen state to a relatively hydrophobic, deswollen state when warmed above their volume phase transition temperature (VPTT). More specifically, above the hydrogel's VPTT, hydrogen bonding between water molecules and hydrophilic amide groups is disrupted leading to deswelling[140]. One type of hydrogel that has received attention for its thermoresponsive properties is PNIPAAm. Temperature modulation of PNIPAAm hydrogels has been

widely exercised for the controlled detachment of cell sheets without chelating or enzymatic agents that potentially compromise the integrity of the cultured cells[141-144]. Exploiting this property, thermoresponsive hydrogels can be utilized to self-clean or detach cells from its surface to limit biofouling. In order to implement PNIPAAm-based hydrogels as a self-cleaning membrane for an implanted biosensor, its VPTT, diffusion characteristics, and mechanical properties were evaluated for two designs.

Initially, inorganic polysiloxane nanoparticles (NPs) (~200 nm in diameter) were crosslinked into a single organic PNIPAAm hydrogel mesh, which enhanced the mechanical strength and the extent of swelling/de-swelling[125]. More recently, these characteristics were further developed by the fabrication of a double network (DN) PNIPAAm-based hydrogel. This DN hydrogel consists of a tightly crosslinked first network with a loosely crosslinked second. It was determined that by increasing the crosslinker, *N*,*N'*-methylenebisacrylamide (BIS), concentration (4 wt%) and introducing ~200 nm polysiloxane NPs (2 wt%) within the first PNIPAAm network and adding a lower BIS concentration (0.2 wt%) in the second PNIPAAm network, the storage modulus and swelling ratio were improved[123].

With regards to the VPTT, PNIPAAm has a characteristic VPTT of ~33-34 °C, which, if implanted, would remain in its collapsed state since the host's body temperature is warmer[145, 146]. If the hydrogel were to remain in its de-swollen (hydrophobic) phase, it would increase the likelihood for cellular attachment and proliferation, decrease the target analyte diffusion, and abandon the advantageous thermal modulating property. Research has shown that the VPTT may be increased with

copolymerization of *N*-isopropylacrylamide (NIPAAm) with hydrophilic comonomers[147, 148]. Therefore, Gant *et al* incorporated the hydrophilic comonomer, *N*-vinylpyrrolidone (NVP) (2 wt%), and tailored the transition temperature to ~39 °C[149]. This will allow the implanted hydrogel to remain in a swollen state at body temperature (~37 °C) and essentially reduce cellular attachment by limiting non-specific protein adhesion.

Diffusion of the target analyte is essential for the membrane to function as a self-cleaning membrane for an implanted glucose biosensor. Due to the thermoresponsive nature of the PNIPAAm-based hydrogel, the diffusion coefficient increases or decreases as the hydrogel swells or de-swells, respectively. Therefore, glucose diffusion at multiple environmental temperatures have been performed on single network (SN) versions of the PNIPAAm-based hydrogel. The results indicated that the glucose diffusion coefficients at temperatures of 30 °C, 35 °C, and 39 °C fell within a usable range in comparison to glucose diffusion coefficients in dermal and epidermal tissues[149].

1.4. Summary

With approximately 380 million individuals currently affected by diabetes mellitus and alarming predictions of its growth, the continuous monitoring of blood glucose concentration is critical. Through the years, there has been much progression in CGM system development. As a result, a few systems are currently available worldwide. In the United States, however, only two CGM systems are on the market: the Guardian®

REAL-Time (Medtronic) and the G4 Platinum CGM (DexCom™). Although providing patients' with the ability to monitor their glycemic levels more frequently, these amperometric-based, transdermal sensors are only FDA approved for use up to 7 days with multiple daily "finger-prick" calibrations.

An optical approach, specifically FRET, offers one potential scheme to accomplish continuous readings. Such a sensor may be intradermally implanted and optically interrogated non-invasively using an external, mobile device. An intradermally implanted sensor could decrease the risk of a chronic infection, an issue plaguing current, commercial CGM systems. These transcutaneous devices provide continuous micro-abrasions and an infectious pathway that results in a heightened immune response and a more pronounced level of biofouling.

Biofouling, the biological interference to the function of an implanted device, is the primary cause for the limited lifespan of implanted devices, including biosensors. The triggered acute and chronic immune response to an implanted material, even those considered biocompatible, initiates a complex cascade of events that eventually results in the formation of an encapsulating fibrous tissue. Immense research effort has been put forth to investigate various material properties that may help control protein and cellular attachment, and thereby, minimize or delay the onset of unwelcomed biofouling effects. Other studies have even looked into lacing "smart" hydrogels with anti-inflammatory agents that can temporarily disrupt the host's local immune reaction. However, dynamic, thermoresponsive hydrogels offer a unique method to reduce non-specific protein

adsorption and its cascading suffocating fibrous capsule while entertaining the ability to house a FRET-based, glucose-sensing assay.

CHAPTER II

IN VITRO EXAMINATION OF A "SELF-CLEANING" MEMBRANE*

2.1. Overview

The lifetime and efficacy of a subcutaneously implanted glucose biosensor could be greatly improved by a self-cleaning membrane capable of periodic physical removal of adhered cells associated with the foreign body reaction. Previously, we reported a DNNC membrane comprised of PNIPAAm and embedded polysiloxane nanoparticles. When the membrane was thermally cycled above and below its VPTT (~33-35 °C), the associated deswelling and reswelling, respectively, led to *in vitro* cell release. Herein, this membrane design was tailored to meet the specific demands of a subcutaneously implanted glucose biosensor and critical functional properties were assessed. First, NVP comonomer increased the VPTT to ~38 °C so that the membrane would be swollen and thus more permeable to glucose in the "off-state" (i.e. no heating) while residing in the subcutaneous tissue (~35 °C). Second, glucose diffusion kinetics though the DNNC membrane was experimentally measured in its deswollen and reswollen states. A cylindrical DNNC membrane with dimensions considered suitable for implantation (1.5

---

* Parts of this chapter are reprinted with kind permission from "Self-Cleaning Membrane to Extend the Lifetime of an Implanted Glucose Biosensor" by Alexander A. Abraham, Ruochong Fei, Gerard L. Coté, Melissa A. Grunlan, 2013. *Applied Materials and Interfaces*, 5(24), 12832–12838, Copyright 2013 by ACS Publications.

x 5 mm, diameter x length) was used to model the glucose diffusion lag time. In addition, the DNNC cylinder was used to observe dimensional changes associated with deswelling and reswelling. Non-cytotoxicity was confirmed and self-cleaning was assessed *in vitro* in terms of thermally-driven cell release to confirm the potential of the DNNC membrane to control biofouling.

2.2. Introduction

A subcutaneously implanted glucose biosensor could offer a continuous and more convenient method to monitor glucose levels. Unfortunately, membrane biofouling severely limits the lifetime and accuracy of subcutaneous or transdermal sensors[150, 151]. Upon implantation of a sensor, a foreign body reaction is triggered that results in the attachment of proteins and cells to the surrounding membrane and, eventually, the formation of a fibrous capsule[150, 151] (**Fig. 2.1.**). Membrane biofouling will inhibit glucose diffusion to the sensor thereby causing its failure. In this way, commercially available transdermal CGM systems are limited to a 3-7 day lifetime. Approaches to control membrane biofouling have largely focused on passive or "anti-fouling" membranes such as those based on poly(ethylene glycol)diacrylate (PEG-DA)[63], poly(hydroxyethylmethacrylate) (PHEMA)[152], and poly(tetrafluoroethylene) (PTFE)[153, 154]. In contrast, the self-cleaning membrane reported herein relies on an active or "foul-releasing" mechanism to physically remove adsorbed cells.

Thermoresponsive PNIPAAm hydrogels undergo deswelling and reswelling when heated above and cooled below, respectively, their VPTT (~33-35 °C). This

process has been shown to cause the release of cultured cells *in vitro*[125, 155-159]. If utilized as a membrane for an implanted glucose biosensor, self-cleaning may be accomplished via transdermal thermal cycling. Conventional single network (SN) PNIPAAm hydrogels prepared via copolymerization of NIPAAm and a crosslinker such as BIS exhibit slow deswelling and reswelling kinetics (i.e. thermosensitivity) as well as poor mechanical properties[160, 161]. When used as a self-cleaning membrane, the PNIPAAm hydrogel requires enhanced thermosensitivity (for self-cleaning) as well as robust mechanical properties (for surgical insertion). Recently, we reported a DNNC hydrogel comprised of an interpenetrating, asymmetrically crosslinked PNIPAAm matrix with polysiloxane nanoparticles (~200 nm diameter) embedded during formation of the first network[162]. This DNNC hydrogel exhibited significantly improved thermosensitivity in terms of both the rate and the extent of deswelling and reswelling versus a conventional PNIPAAm hydrogel. Furthermore, the DNNC hydrogel exhibited improved modulus and strength.

Extending the utility of this DNNC hydrogel as a self-cleaning membrane for an implanted glucose biosensor requires further refinement and is addressed in this study. First, the VPTT of the DNNC membrane was increased to ~38°C. In the subcutaneous tissue of the wrist, a likely location for an implanted sensor, the body temperature is ~35 °C[163, 164]. Thus, a membrane with a VPTT ~38°C in the "off-state" will be fully swollen for optimal glucose diffusion. When undergoing self-cleaning ("on-state"), the membrane would begin to deswell via transdermal heating. Copolymerization of NIPAAm with a hydrophilic comonomer is known to increase the VPTT of the resulting

hydrogel[165, 166]. Previously, we demonstrated that addition of 1-2 wt% NVP comonomer (based on NIPAAm wt) produced analogous SNNC hydrogels with a VPTT of ~38°C[167]. Thus, NVP was similarly incorporated into the DNNC hydrogels. Second, glucose diffusion through a planar DNNC membrane was measured at temperatures above and below the VPTT. Third, a membrane with a geometry suitable for implantation was considered to be a cylindrical rod (~1.5 mm x 5 mm, diameter x length) (**Fig. 2.2.**). A finite element model was constructed for the DNNC hydrogel cylinders to estimate the glucose diffusion lag time before achieving equilibrium with its external environment at varying glucose concentrations. Since size and geometry also affect thermosensitivity[168, 169], which are critical to fast and efficient self-cleaning, the thermosensitivity of the DNNC hydrogel cylinders was assessed by measuring the change in diameter with temperature. Finally, cytocompatibility was assessed and thermally-induced *in vitro* cellular detachment was observed using planar DNNC hydrogels.

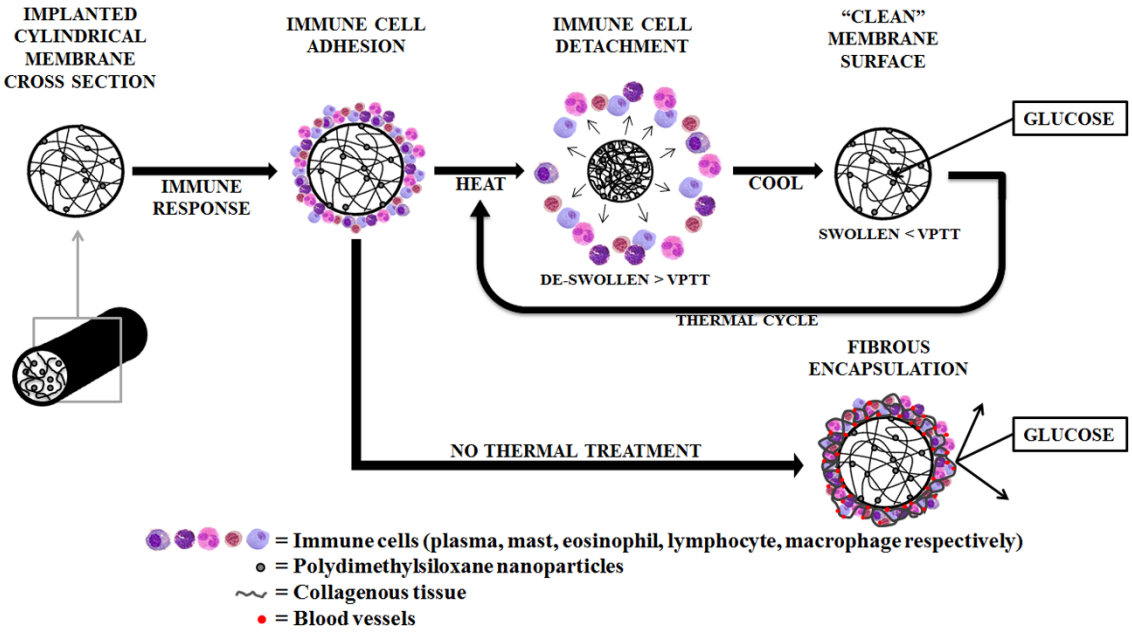

Figure 2.1. | Diagram of "self-cleaning" membrane to minimize biofouling. Fibrous encapsulation of a membrane surrounding an implanted biosensor compromises glucose diffusion. The double network nanocomposite (DNNC) membrane described herein is designed to exhibit "self-cleaning" when thermally cycling above its volume phase transition temperature (VPTT).

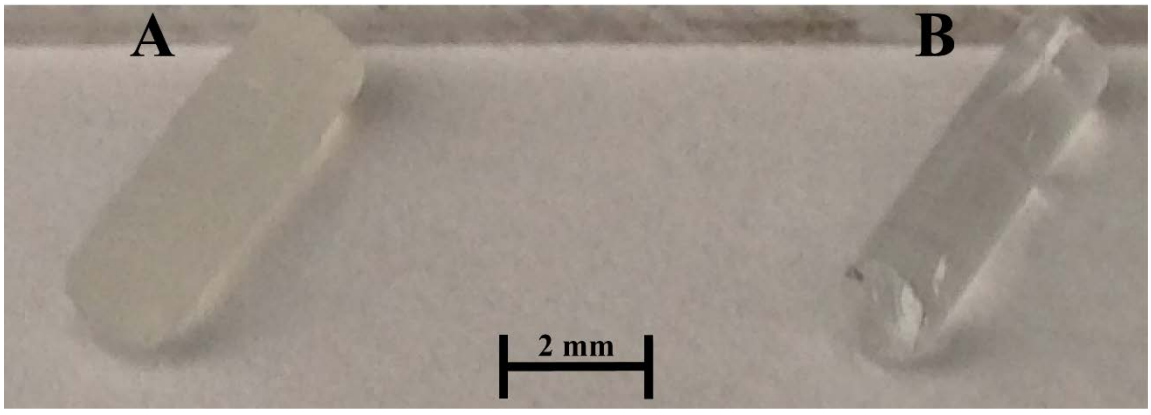

Figure 2.2. | DNNC and PEG-DA cylindrical membranes. a,b, DNNC (**a**) and PEG-DA (**b**) cylindrical membranes fabricated with a diameter of ~1.5 mm and length of 5 mm.

2.3. Materials and Methods

2.3.1. Materials

NIPAAm (97%), NVP, PEG-DA (MW 575 g/mol), ammonium hydroxide (NH_4OH), sodium chloride (NaCl), sodium phosphate-dibasis (Na_2HPO_4), potassium phosphate-monobasis (KH_2PO_4), hydrochloric acid (HCl), sodium hydroxide (NaOH), newborn calf serum (NCS), antibiotic antimycotic solution (100X) - stabilized bioreagent sterile filtered with 10,000 units penicillin and 10 mg streptomycin A, sterile Dulbecco's phosphate buffered saline (PBS), HEPES (≥ 99.5%), and Dulbecco's Modified Eagle's Medium (DMEM) –1000 mg dL^{-1} glucose and L-glutamine without sodium bicarbonate and phenol red were purchased from Sigma-Aldrich (St. Louis, MO). Potassium chloride (KCl) and D-glucose anhydrous was purchased from Fisher Scientific (Pittsburgh, PA). Potassium persulfate ($K_2S_2O_8$) was purchased from Mallinchrodt Chemicals. *N*,*N*'-methylenebisacrylamide (BIS, 99%) was purchased from Acros Organics (Geel, Belgium). 2-Hydroxy-2-methyl-1-phenyl-1-propanone (Darocur 1173) and 1-[4-(2-Hydroxy)-phenyl]-2-hydroxy-2-methyl-1-propane-1-one (Irgacure 2959) was purchased from Ciba Specialty Chemicals (Tarrytown, NY). Octamethylcyclotetrasiloxane (D_4) and 1,3,5,7-tetramethyl-1,3,5,7-tetra-vinylcyclotetrasiloxane (D_4^{Vi}) came from Gelest, Inc. Dodecylbenzenesulfonic acid (DBSA, BIO-SOFT® S-101) came from Stepan Co. (Northfield, IL). The Slide-A-Lyzer dialysis cassettes (MWCO 10,000) and lactate dehydrogenase (LDH) cytotoxicity assay kit were obtained from Pierce (Rockford, IL). For hydrogel fabrication and other

experiments, deionized water (DI H_2O) with a resistance of 18 MΩ·cm (Millipore, Billerica, MA) was used. 3T3 H2B-GFP mouse fibroblast cell line was a kind gift from Peter Ghazal at the Division of Pathway Medicine at the University of Edinburgh. Cell culture media was pH adjusted with 1 M HCl and 1 M NaOH, verified with a pH meter (420 A+, Orion; electrode 5990-30, Cole-Parmer, Vernon Hills, IL) and sterilized by 0.2 μm filtration (sterile 90 mm filter unit, Nalgene Filtration Products).

2.3.2. Polysiloxane Nanoparticle Preparation

Polysiloxane colloidal nanoparticles with an average diameter of ~200 nm were prepared via emulsion polymerization and purified via dialysis as previously reported[125]. The final emulsion was 4.8 wt% solids.

2.3.3. Preparation of PEG-DA Hydrogels

Precursor solutions were formed by votexing DI-H_2O, PEG-DA (100 %v/v) and Darocur 1173 (1% v/v) for 1 min.

Planar sheets. Planar hydrogel sheets (~1 mm thick per electronic caliper measurements) were prepared by pipetting the precursor solution between two clamped glass slides (75 x 50 mm) separated by polycarbonate spacers (1 mm thick) and exposing the mold to longwave ultraviolet (UV) light (UVP UV-Transilluminator, 6 mW cm^{-2}, λ_{peak} = 365 nm) for 2 min at room temperature (RT). Hydrogel sheets were removed from their molds, rinsed with DI H_2O and soaked in a Petri dish containing DI H_2O (60 mL) for 24 hours.

Cylinders. Cylindrical hydrogels (~1.5 mm x 5 mm, diameter x length per electronic caliper) were prepared by pipetting the precursor solution into a hollow cylindrical glass mold (inside diameter = 1.0 mm, length = 15 mm) with one end sealed by Parafilm. After sealing the other end of the mold, it was likewise exposed to longwave UV light as above at RT for 3 sec. The cylindrical hydrogel was removed from the mold, rinsed with DI H_2O and immersed in a Petri dish containing DI H_2O (60 mL) for 24 hours. A clean razor blade was used to equally trim the ends to reduce the length to 5 mm.

2.3.4. Preparation of Thermoresponsive DNNC Hydrogels

DNNC hydrogels were prepared by sequential formation of a relatively tightly crosslinked 1st network containing polysiloxane nanoparticles (2 wt% solid nanoparticles based on NIPAAm weight) and a loosely crosslinked 2nd network.[162] The "1st network precursor solution" was formed by combining NIPAAm monomer (1.0 g), NVP co-monomer (0.16 g), BIS crosslinker (0.04 g), polysiloxane nanoparticle emulsion (0.485 g), Irgacure-2959 photoinitiator (0.08 g) and DI H_2O (6.54 g). The "2nd network precursor solution" was formed by combining NIPAAm (6.0 g), NVP (0.96 g), BIS (0.012 g), Irgacure 2959 (0.24 g), and DI H_2O (21.0 g).

Planar sheets. Planar hydrogel sheets (1 mm thick) were produced by pipetting the 1st network precursor solution into a mold consisting of two clamped glass slides (75 x 50 mm) separated by 1 mm thick polycarbonate spacers. The mold was then immersed into an ice water bath (~7 °C) and exposed to longwave UV light for 30 min. The

resulting single network nanocomposite (SNNC) sheet was removed from the mold, rinsed with DI H_2O and then soaked in DI H_2O at RT for 2 days with daily water changes. The SNNC sheet was then transferred into a covered Petri dish containing the 2^{nd} network precursor solution for 24 hours at RT. Next, the planar hydrogel was placed into a rectangular mold (1.5 mm thick), photocured for 30 min and finally soaked in DI H_2O as above.

Cylinders. Cylindrical hydrogels (~1.5 mm x 5 mm, diameter x length) were prepared by pipetting the precursor solution into a cylindrical glass mold (inside diameter = 1.0 mm, length = 15 mm) as above. The mold was immersed in an ice water bath (~7 °C) and exposed for 10 min to longwave UV light. Cylindrical hydrogels were removed from their molds, rinsed with DI H_2O, and soaked in a Petri dish containing DI H_2O (60 mL) for 2 days at RT with daily water changes. A SNNC cylindrical hydrogel was then transferred into a Petri dish containing the 2^{nd} network precursor solution for 24 hours at RT. The cylindrical hydrogel was then placed into a second cylindrical mold (diameter = 1.5 mm, length = 15 mm), submerged in an ice water bath (~7 °C), exposed for 10 min to longwave UV light and soaked in DI H_2O as above. A clean razor blade was used to trim ends to reduce the cylindrical length to 5 mm. The final diameter was measured via calipers.

2.3.5. Differential Scanning Calorimetry (DSC)

The *VPTT* of swollen hydrogels was determined by differential scanning calorimetry (DSC, TA Instruments Q100). Water-swollen hydrogels were blotted with a

Kim Wipe and a small piece sealed in a hermetic pan. After cooling to -50 °C, the temperature was increased to 50 °C at a rate of 3 °C /min for 2 cycles. The resulting endothermic phase transition peak is characterized by the initial temperature at which the endotherm starts (T_o) and the peak temperature of the endotherm (T_{max}). Reported data are from the 2nd cycle.

2.3.6. Glucose Diffusion

Planar hydrogel strips (1 cm x 1 cm x 1 mm) were placed in a side-by-side diffusion cell (PermeGear, Bethlehem, PA) positioned atop a stir plate. The donor chamber contained 3 mL of glucose solution (~1,000 mg dL^{-1}) and the receptor chamber contained 3 mL of DI H_2O. Chamber solutions were stirred with Teflon-coated stir bars (800 rpm) to maintain constant solution concentrations. A water jacket maintained the designated temperature (25, 35 and 40 °C) throughout the system. Every 20 min (for a total time of 3 hours), 50 µL aliquots were removed via pipette from each chamber and glucose concentration determined with a YSI 2700 Select Biochemistry Analyzer (YSI Incorporated, Yellow Springs, OH). The diffusion coefficients were calculated using Fick's second law of diffusion.

2.3.7. Glucose Diffusion Lag Time

A computational model of the DNNC hydrogels was developed using COMSOL Multiphysics® software (COMSOL, Inc., Los Angeles, CA). Conducting a time-dependent transport of diluted species study, a geometric cylinder (1.5 mm x 5 mm,

diameter x length) was constructed with a maximum and minimum free tetrahedral mesh element size of 0.382 mm and 0.0249 mm, respectively. The simulation began with a DNNC hydrogel internal glucose quantity of 0 mg dL^{-1} and external glucose levels of 60, 80, 160 and 300 mg dL^{-1}. The average glucose concentration within the cylindrical hydrogel was assessed every second for 1 hour for each external glucose concentrations. The diffusion lag time was defined as the time required for the hydrogel internal glucose concentration to fall within 5% of the external glucose concentration.

2.3.8. Thermosensitivity

Three cylindrical DNNC hydrogels (~1.5 mm x 3 mm, diameter x length) were vertically attached to a single Petri dish with a small amount of optical adhesive (Norland Optical Adhesive 61) to the base of one end. To hydrate the affixed cylinders, the Petri dish was filled with DI H_2O for at least 12 hours at RT prior to thermally cycling. The Petri dish was positioned atop a heating plate under a non-inverted bright field microscope (Nikon Eclipse LV 100D, Nikon America Inc., Melville, NY) with a 5X objective. Images were taken every 5 min as the hydrogels were thermally cycled between 25 and 40 °C for 5 cycles. The average rate of heating to 40 °C was ~1.06 °C/min and passive cooling to 25 °C was ~0.28 °C/min. Thus, each cycle consisted of a 1 h heating period followed by 1 hour of passive cooling. Cylinder diameters were recorded with Nikon® NIS Elements imaging software.

2.3.9. Cytocompatibility

DNNC hydrogel cytocompatibility was assessed by measuring LDH concentrations released by 3T3 H2B-GFP mouse fibroblast cells 24 hours after cell seeding versus that of two cytocompatible controls – a PEG-DA hydrogel as well as tissue culture plastic (i.e. polystyrene, PS). Planar DNNC and PEG-DA hydrogel sheets were prepared as described above. Four 6 mm discs were punched from each sheet and then sterilized by immersion in 80% ethanol for 45 min. The hydrogel discs were sequentially washed 3X (30 min each) with sterile DMEM (40% NCS), submerged in DMEM (40% NCS) for 24 hours and transferred to a sterile 12-well plate. Next, 3T3 H2B-GFP mouse fibroblast cells [suspended in DMEM (40% NCS) containing antimycotics and antibiotics], were seeded onto each of the hydrogel surfaces and into the empty tissue culture plastic wells at a concentration of ~6,500 cells cm^{-2}. Cells were allowed to incubate for 24 hours at ~37 °C (T < VPTT; swollen state) with 5% CO_2. Finally, the media surrounding the hydrogel discs or from the empty wells was extracted and assessed for LDH levels per the manufacturer's protocol. The relative LDH activity was calculated by normalizing PEG-DA and DNNC sample absorptions to that of polystyrene.

2.3.10. "Self-cleaning" Behavior In Vitro

Planar DNNC and PEG-DA hydrogel sheets (2 cm x 2 cm x ~1 mm) were sterilized by immersion in 80% ethanol for 45 min. All specimens were then washed 3X for 30 min each with sterile DMEM (40% NCS). DNNC and PEG-DA hydrogel sheets

were submerged for 48 and 96 hours, respectively, in DMEM (40% NCS). Next, in a sterile plastic Petri dish, DNNC and PEG hydrogel sheets were inoculated with 3T3 H2B-GFP mouse fibroblast cells stained with a lipophilic indocarbocyanine dye (DiI) and suspended in DMEM (40% NCS) containing antimycotics and antibiotics at a concentration of ~30,000 cells/mL. For DNNC and PEG hydrogels, cells were allowed to incubate for 4 hours and 72 hours, respectively, at ~35 °C (T < VPTT; swollen state) with 5% CO_2 before imaging. The Petri dish was transferred to the enclosed microscope stage which contained two heating pads (Minco) connected to thermistors controlled via a temperature feedback system (LabView). Hydrogel surface images were captured every 20 sec for 10 min with an inverted bright field microscope (Nikon Eclipse TE 2000-S, Nikon America Inc., Melville, NY) with a 10X objective as the temperature was increased from ~35 °C to ~39.5 °C (T > VPTT) at a rate of ~0.41 °C/min (i.e. ~10 minutes).

2.4. Results and Discussion

2.4.1. VPTT

By incorporating low levels of NVP comonomer (1.6 wt% based on NIPAAm monomer weight) into the 1st and 2nd network precursor solutions, the VPTT of the DNNC hydrogel was successfully increased. Per the DSC thermogram (**Fig. 2.3.**), T_o and T_{max} were equal to 36.5 and 39.5 °C, respectively. Thus, at subcutaneous body

temperature of the wrist (~35 °C), the DNNC hydrogel are expected to be swollen in the absence of external heating (i.e. “off-state”).

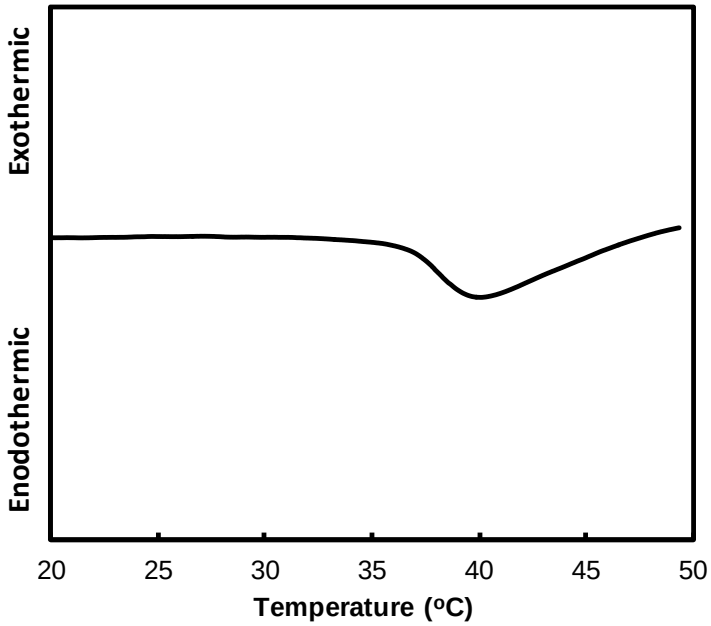

Figure 2.3. | DSC thermogram of the DNNC hydrogel. The DSC thermogram indicates a successful increase in the VPTT of the DNNC hydrogel to ~ 38 °C.

2.4.2. Glucose Diffusion

A side-by-side diffusion cell system was used to study glucose diffusion through the DNNC membrane 25 °C (T < VPTT), 35 °C (body temperature), and 40 °C (T > VPPT). Fick’s second law of diffusion was used to calculate the diffusion coefficients at each temperature:

$$\frac{\partial c}{\partial t} = D\frac{\partial^2 c}{\partial x^2}$$

where c is the concentration within the hydrogel, t is the time, D is the diffusion coefficient and x is the diffusion distance[170-173]. Assuming that each solution preserved a uniform concentration and that each element concentrations were equal at the hydrogel membrane surface as in the bulk volume of each chamber, the equation may be simplified to:

$$Q_t = \frac{ADC_1}{L}\left(t - \frac{L^2}{6D}\right)$$

where Q_t is the overall quantity of glucose transferred through the hydrogel until the specified time, t, A refers to the hydrogel area exposed to the donor or receptor chambers, C_1 is the initial solute concentration of the donor chamber, and L is the measured hydrogel membrane thickness. **Table 2.1.** reveals the influence of temperature on the diffusion coefficients (D) of the DNNC hydrogel. At 25 °C (T < VPTT), the swollen state of the hydrogel facilitates glucose diffusion. In contrast, when heated to 40 °C (T > VPTT), the hydrogel is deswollen and glucose diffusion is thus substantially slowed. While still below the measured T_o of the VPTT (~36.5 °C), glucose diffusion at 35 °C (body temperature) began to decrease somewhat indicating that some deswelling may have occurred. However, D of glucose through the dermis and epidermis has been

reported as 2.64 ± 0.42 x 10^{-6} cm^2/s and 0.075 ± 0.05 x 10^{-6} cm^2/s, respectively[174]. Thus, *D* of glucose through the hydrogel (1.88 ± 0.01 x 10^{-6} cm^2/s) is within the functional range. Furthermore, *D* of a PEG-DA (MW 575 g/mol) hydrogel was previously determined to be 1.59 ± 0.42 x 10^{-6} cm^2/s [175] and such materials are noted to not significantly impede glucose transfer to encapsulated biosensors[176]. Thus, in the "off-state", glucose diffusion through the DNNC hydrogel to the enclosed sensor is expected to be satisfactory.

Temperature (°C)	Membrane Behavior	Diffusion Coefficient (cm^2/s)
25 *(T < VPTT)*	Swollen	2.73 ± 0.01 x 10^{-6}
35 *(body temperature)*	Swollen	1.88 ± 0.01 x 10^{-6}
40 *(T > VPTT)*	Deswollen	1.03 ± 0.01 x 10^{-6}

Table 2.1. | Glucose diffusion coefficients. Glucose diffusion coefficients (*D*) of the DNNC hydrogel (VPTT ~38 °C) at varying temperatures.

2.4.3. Potential Glucose Lag Time

A COMSOL Multiphysics® computational model was utilized to evaluate the glucose diffusion lag time for a DNNC cylindrical hydrogel. The simulation began with an initial glucose quantity of 0 mg dL^{-1} within the hydrogel and the hydrogel then suspended in an environment with a constant glucose level of varying concentrations: 60, 80, 160, and 300 mg dL^{-1}. These concentrations represent low, normal, high and very high physiologically glucose levels, respectively[2]. **Figure 2.4.** expresses the average

glucose concentration within the cylindrical hydrogel cavity every second for 1 hour at each of the external glucose concentrations. Physiological lag times upwards of 15 min have been reported between glucose changes in the interstitial fluid (ISF) and in the blood[177-181]. For the DNNC cylindrical hydrogel (diameter 1.5 mm, length 5 mm), an average lag time of 19.59 ± 0.13 minutes was observed and thus somewhat exceeds physiological lag. To reduce the lag time, the cylinder diameter may be reduced. For instance, when the model was applied to a DNNC cylindrical hydrogel with a reduced diameter (diameter 350 μm, length 5 mm), a lag time of less than 5 min was determined (**Fig. 2.5.**).

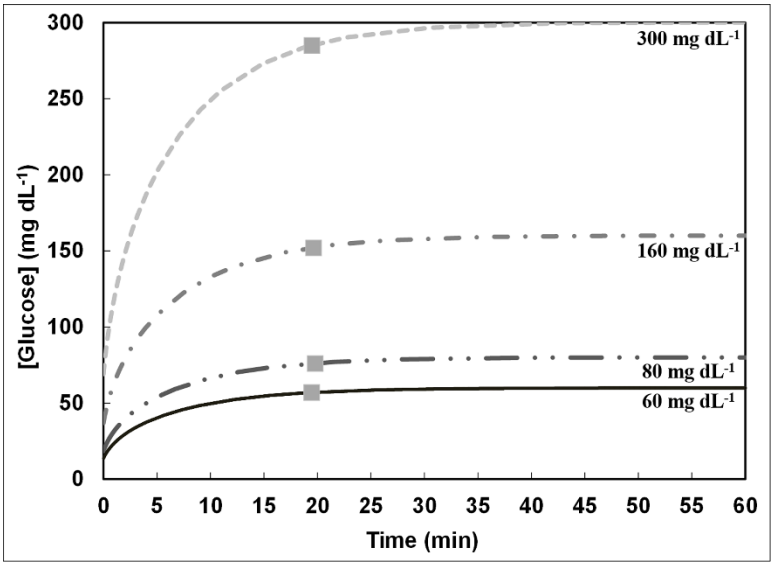

Figure 2.4. | DNNC glucose lag time computational model. A computational model was utilized to determine the average glucose concentration inside a DNNC cylindrical hydrogel at 35 °C for constant environmental glucose levels of 300, 160, 80 and 60 mg dL^{-1}. The glucose diffusion lag time (■) marks when the average internal hydrogel glucose concentration is 95% to that of the external environment.

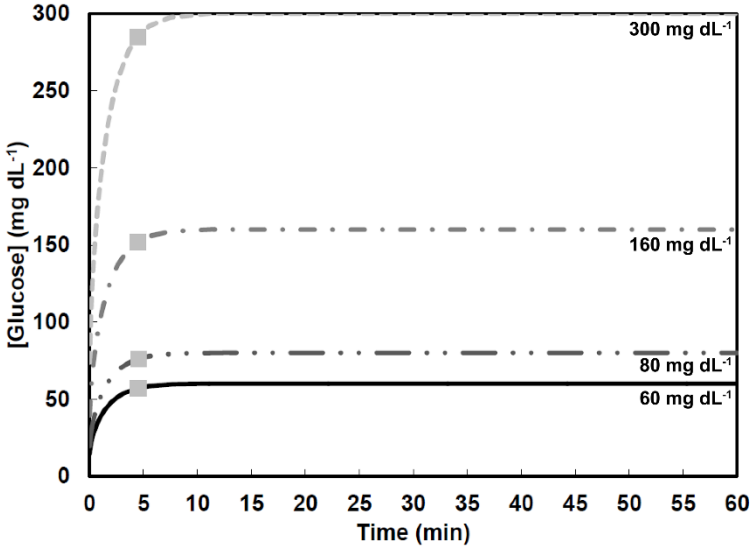

Figure 2.5. | Reduced DNNC glucose lag time computational model. Decreasing the cylindrical diameter to 350 µm, a computational model exhibited the average glucose concentration inside a DNNC hydrogel at 35 °C for constant environmental glucose levels of 300, 160, 80 and 60 mg dL^{-1}. The glucose diffusion lag time (■) marks when the average internal hydrogel glucose concentration is 95% to that of the external environment. The mean glucose lag time was determined as 4.48 ± 0.02 minutes.

2.4.4. DNNC Thermosensitivity

The extent and rate at which the DNNC cylindrical hydrogel deswells and reswells upon cyclically heating ($T > VPTT$) and cooling ($T < VPTT$) is important for its ability to function as a self-cleaning membrane for a subcutaneous glucose biosensor. First, the extent of deswelling is critical as this is the driving force behind physical removal of adhered cells on the membrane.[125, 155] When the temperature was increased and maintained at ~40 °C for 1 hour, the diameter of a vertically affixed DNNC cylinder decreased to ~25% of its initial swollen state diameter at RT (Figure 4). After returning to 25 °C for a period of 1 hour, the diameter returned to within 5% of its initial measured

swollen state diameter. Second, the membrane must be able to undergo cyclical deswelling/reswelling while being thermally cycled. This behavior was confirmed by subjecting a vertically affixed DNNC cylinder to cyclical heating (~1.06 °C/min) and cooling (~0.28 °C/min) over a 10 hour period (Figure 5). Here, diameters achieved in the swollen and deswollen states remained very consistent.

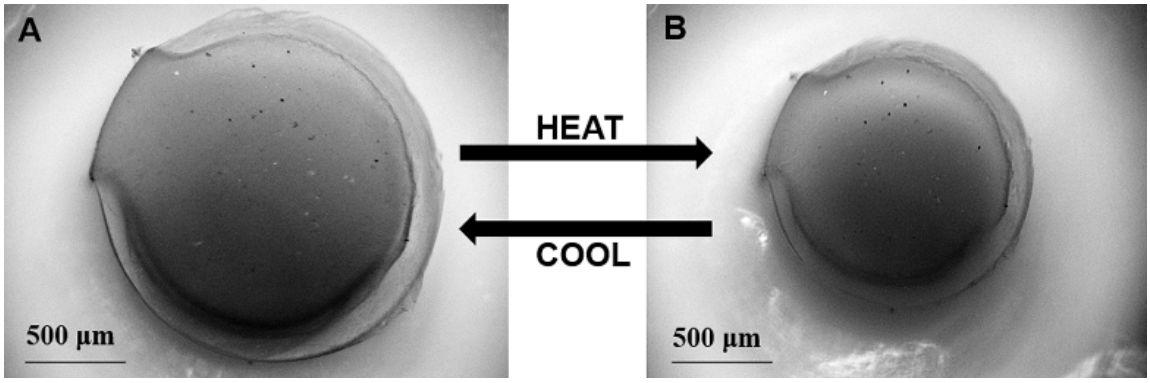

Figure 2.6. | DNNC membrane bright field microscopy. a,b, Bright field microscopy images of a vertically affixed DNNC cylinder in its swollen state at 25 °C (T < VPTT) (**a**) and deswollen state at 40 °C (T > VPTT) (**b**).

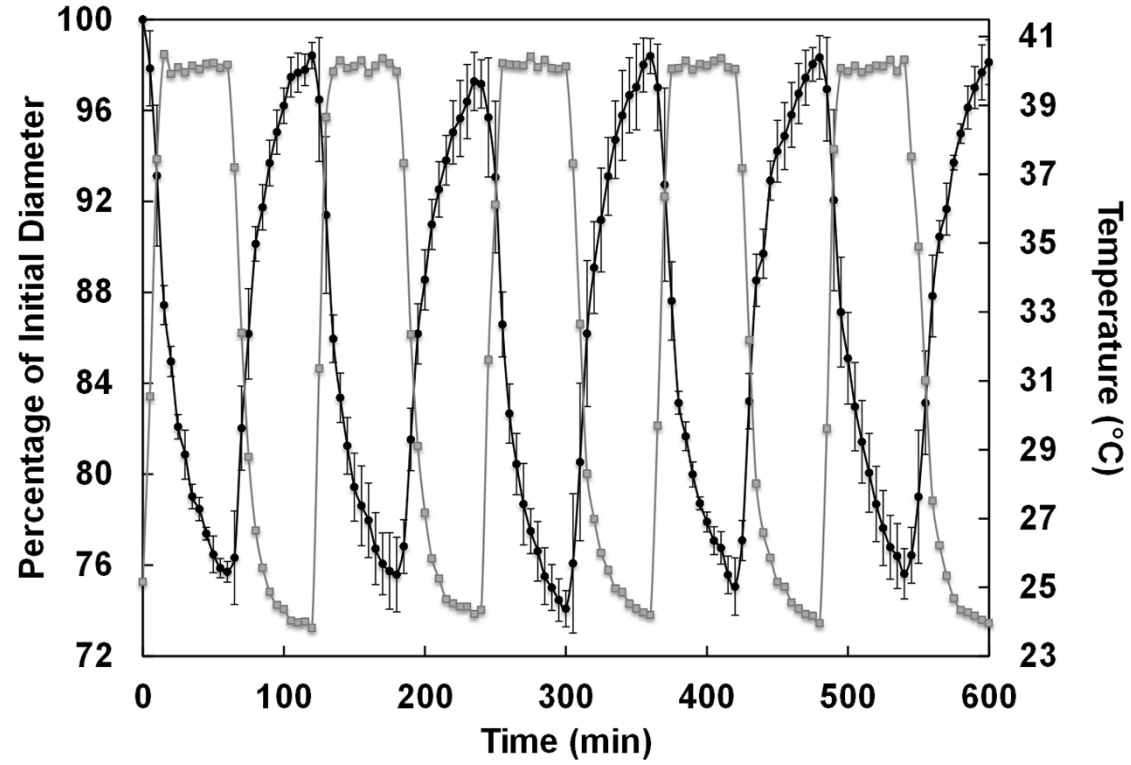

Figure 2.7. | DNNC membrane temperature modulation thermoresponse. Diameter change during thermal cycling of a vertically affixed DNNC cylinder over a 10 hour time period. Diameter change (black) and temperature change (grey).

2.4.5. Cytocompatibility

Cytocompatibility is essential to the utility of a self-cleaning membrane for a subcutaneously implanted glucose biosensor. The cytocompatibility of the DNNC hydrogel was determined via LDH activity assays (**Fig. 2.8**). LDH is a soluble cytosolic enzyme that is released into the culture medium due to apoptosis or necrosis[182]. LDH levels released by 3T3 H2B-GFP mouse fibroblast cells 24 hours post-seeding were measured for the DNNC hydrogel and compared to that of non-cytotoxic PEG-DA hydrogel and tissue culture plastic (i.e. PS). No statistical difference in normalized levels

of exogenous LDH activity was observed. Thus, the DNNC hydrogel exhibits low cytotoxicity toward fibroblast cells similar to that of PEG-DA hydrogels.

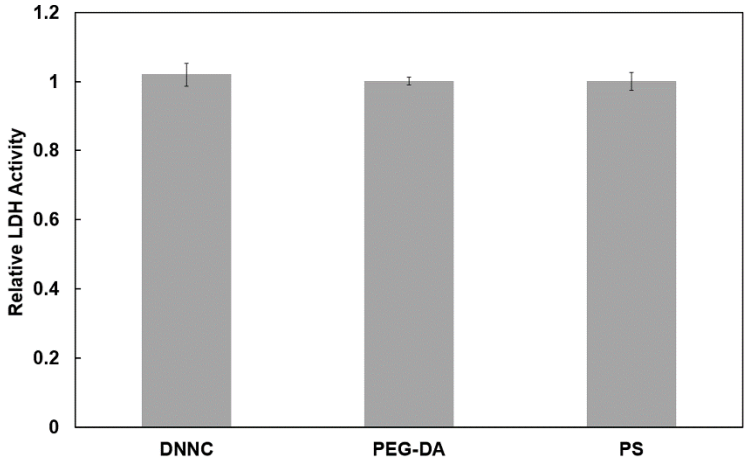

Figure 2.8. | DNNC membrane cytotoxicity study. Relative LDH activity after 24 hours for PEG-DA, DNNC, and polystyrene (PS) inoculated with 3T3 H2B-GFP mouse fibroblast cells.

2.4.6. "Self-cleaning" In Vitro

The ability of the DNNC hydrogel to release adhered cells (i.e. self-clean) when induced to deswell with thermally heating was assessed *in vitro* against a non-thermoresponsive PEG-DA hydrogel control (**Fig. 2.9**). To achieve adequate adhesion of fibroblasts, the DNNC and PEG hydrogel sheets were first exposed to DMEM (40% NCS) for 48 and 96 hours, respectively. Such surface conditioning with protein is a common strategy to facilitate cellular adhesion[183]. This protocol also parallels the way in which an implanted surface first adsorbs proteins prior to the adhesion of cells[150]. A longer conditioning period for PEG hydrogels was determined to be required and can be

attributed to the protein repulsive nature of PEG[184, 185]. Initially, at ~35.4 °C (T < VPTT), both the DNNC and PEG hydrogels were swollen and adhered fibroblasts exhibit a characteristic spread morphology. Heating to a temperature of ~39.5 °C was chosen as it is above the onset of the VPTT of the DNNC hydrogel and is below ~41 °C where protein denaturation may occur. Upon heating, the DNNC hydrogel underwent deswelling and fibroblasts display a round cell morphology indicative of end stages of detachment. In contrast, the PEG hydrogel does not undergo appreciable deswelling and cells remained adhered. The percentage of attached cells on DNNC and PEG-DA hydrogels was assessed from four frames each taken while heating a single membrane from ~35 °C to ~39.5 °C (T > VPTT) over 10 minutes (**Fig. 2.9a-h**). Thus, while the PEG hydrogel was more resistant to cellular adhesion, cell release was thermally triggered for the DNNC hydrogel.

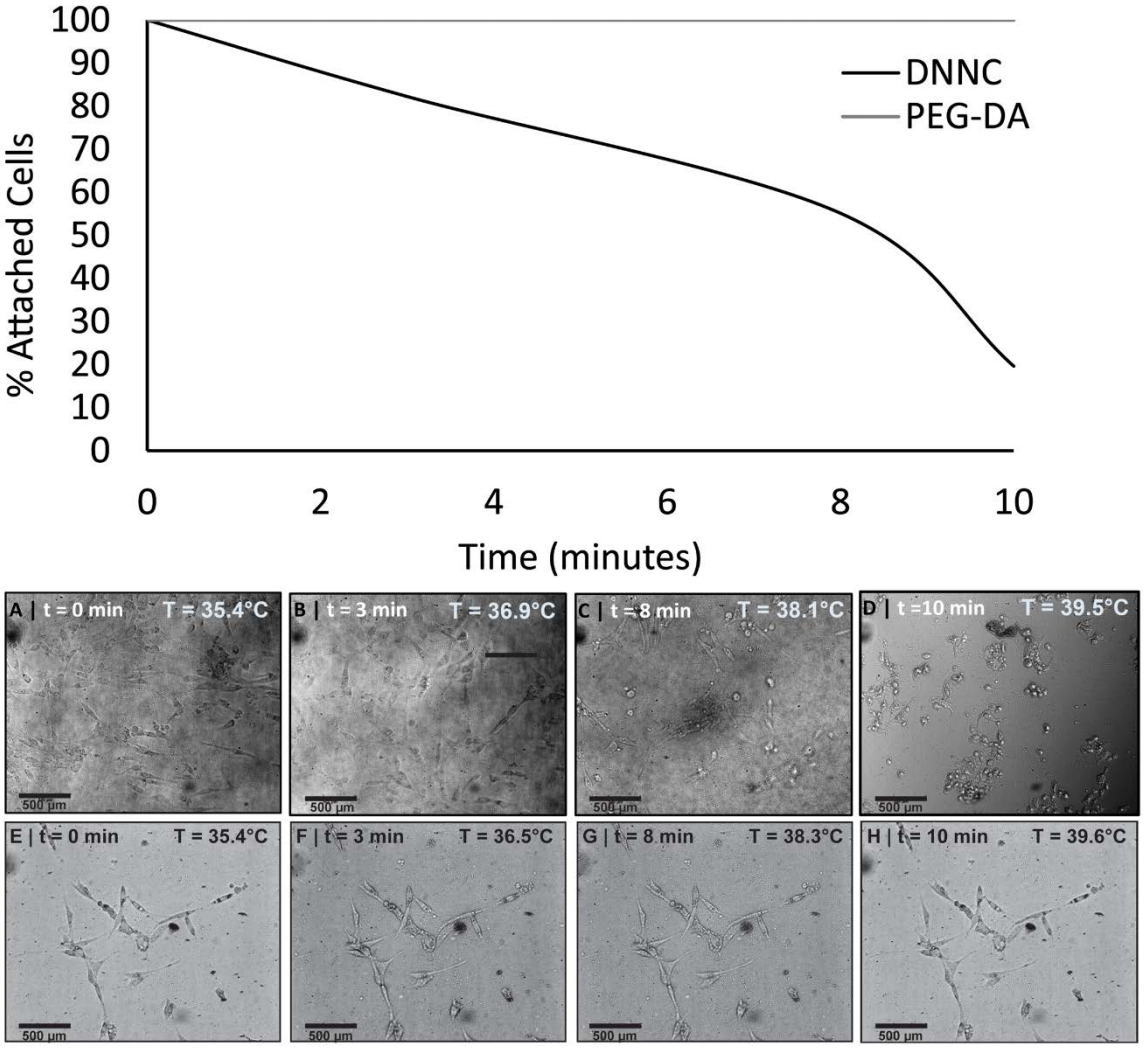

Figure 2.9. | "Self-cleaning" property of the DNNC membrane. a-h, Bright field microscopy frames of DNNC (**a-d**) and PEG-DA (**e-h**) membranes seeded with 3T3 H2B-GFP mouse fibroblast cells incubated at ~35 °C (T < VPTT) and then heated to ~39.5 °C (T > VPTT). **a-d,** Demonstrate the detachment of cells due to deswelling of DNNC membrane. The graph depicts the percentage of attached cells to either DNNC or PEG-DA membranes as the temperature was increased from ~35 °C to ~39.5 °C over a ~10 minute period.

2.5. Summary

A thermoresponsive DNNC hydrogel design was refined and evaluated for its ability to function as a self-cleaning membrane for a subcutaneously implanted glucose biosensor. The VPTT was adjusted to ~38 °C with NVP comonomer such that the membrane would be swollen at body temperature (35 °C, wrist subcutaneous tissue) to maximize glucose diffusion. Thus, when heated about the VPTT, the membrane would undergo reversible deswelling, which should detach adhered cells from its surface. Furthermore, the non-degradable nature of PNIPAAm hydrogels[186, 187] is expected to be advantageous to maintain membrane functionality and to sustain containment of sensing materials.

The measured glucose diffusion coefficient (*D*) for the DNNC membrane was within the physiological range at 35 °C but decreased substantially when the membrane was heated to ~40 °C and deswollen. Consequently, during this phase of self-cleaning, glucose measurements would not be effective. A cylindrical rod (~1.5 mm x 5 mm, diameter x length) was considered to be a suitable geometry for implantation. Based on a finite element model, glucose diffusion lag time for the DNNC hydrogel cylinders was estimated to be ~19 min. However, when a reduced diameter (350 μm) was considered, the lag time was reduced to ~5 min.

Thermosensitivity, critical to self-cleaning efficacy, of the DNNC cylindrical hydrogel was assessed by measuring the change in diameter when in a deswollen (T > VPTT) versus swollen state (T < VPTT). Over a 10 hour period of thermal cycling, the

diameter of the deswollen cylindrical hydrogel returned to within 5% of the original swollen diameter.

In vitro, fibroblast cells exhibited minimal cytotoxicity and release from a planar DNNC hydrogel upon deswelling by heating above the VPTT while cells remained adhered to the non-thermoresponsive PEG-DA surface. Although having demonstrated the ability to minimize cellular adhesion *in vitro, in vivo* systems are significantly more intricate. Therefore in order to progress, the DNNC cellular release efficiency must be evaluated *in vivo*.

CHAPTER III

IN VIVO BIOCOMPATIBILITY OF A "SELF-CLEANING" MEMBRANE

3.1. Overview

Implantable biosensors offer the potential to continuously monitor and communicate measurable data. However, its accuracy and lifetime, however, may be jeopardized by the extent of the host's multi-stage immune response leading to membrane biofouling. Approaches to control membrane biofouling and eventual fibrous encapsulation have largely relied on anti-fouling or passivation approaches or active, therapeutic-based approaches (e.g. anti-inflammatory drug release). Herein, we illustrate a new active, materials-based approach utilizing a thermoresponsive double network nanocomposite (DNNC), poly(*N*-isopropylacrylamide) hydrogel with an adjusted volume phase transition temperature (VPTT) of ~ 38 °C. Cylindrical DNNC hydrogels (~1.5 mm x 5 mm) were fabricated and inserted within the dorsal subcutaneous tissue of CD® Hairless rat models for either 7 or 30 days. Poly(ethylene glycol) diacrylate (PEG-DA) hydrogel cylinders served as non-thermoresponsive controls whose antifouling behavior and biocompatibility is well-established. Upon extraction, DNNC hydrogels exhibited a significantly thinner fibrous capsule than PEG-DA post 30 days while displaying increased microvascular density within 1 mm of the polymer surface. These results reveal an interplay between hydrogel stiffness, enhanced thermosensitivity, and

enlarged average pores that promotes angiogenesis while reducing the degree of fibrous tissue encapsulation – ideal conditions for a biosensor measuring blood analytes.

3.2. Introduction

The medical field has seen significant technological advances especially in the areas of protein/cell/tissue engineering, biotechnology, and biomaterials that have led to the development of implantable devices/materials with various medical or pharmaceutical applications, e.g. biosensors[188-192], heart valves[193], artificial organs[194-196], tissue regeneration[197, 198], and drug delivery[199-202]. However, device efficacy and lifetime may be compromised by the host's immune response to the implanted biomaterial and associated biofouling. For instance, in the case of implanted biosensors, membrane biofouling restricts the diffusion of the target analyte.

The host response to an implantable biomaterial, including a biosensor membrane, is a multiphasic process. It begins with the initial (acute) response that occurs secondary from tissue damage caused by the implantation of the biosensor material. The greater the insertion trauma will result in a more amplified acute response[74]. The acute inflammatory response consists of a humeral and cellular component[57]. Humeral is the initial response and is a vascular driven process with "leakage" of plasma proteins (e.g. albumen, immunoglobulins, and fibrin) into the interstitial compartment that results in the emergence of a provisional matrix formed by dynamic protein cascades known as the Vroman Effect[203, 204]. This bioactive rich environment stimulates the infiltration of a

cellular component that consists primarily of polymorphonuclear leukocytes (PMNs), which generally peak within 24 to 72 hours status post-implantation. PMNs phagocytose microorganisms, and upon degeneration, release cytoplasmic and granular components that conciliate the ensuing inflammatory reaction[205]. Mast cell degranulation also plays a significant role in acute inflammatory response mediation with histamine, interleukin-4 (IL-4), and interleukin-13 (IL-13) release and fibrinogen adsorption[203]. Under ideal conditions, the acute inflammatory response blends into a subacute response where PMNs recede from the exudate and are succeeded by peripheral blood mononuclear cells (PBMCs). Once activated, the admixture of tissue macrophage and lymphocytes may discharge chemotactic factors, cytokines, growth factors, matrix metalloproteinases, and reactive oxygen species that recruit fibroblasts and vascular endothelial cells[118]. If the damaged, necrotic tissue is removed and the biomaterial is neutral (i.e. not antigenic), then the implant site transitions into repair with the initial formation of granulation tissue (admixture of lymphocytes, macrophages, recruited fibroblast [producing collagen fibers] and infiltration with neovascular buds). Granulation tissue undergoes transition into an extracellular matrix that provides an encapsulating scaffold for organizing loose, cellular collagenous connective tissue (composed primarily of fibroblast and to a lesser extent macrophages and lymphocytes) while modulating the biological processes associated with end-stage wound repair[74, 203, 205, 206]. Over time, it remodels into dense, avascular collagenous connective tissue consisting of a collagen substrate with scattered fibrocytes and glycoaminoglycans[207].

Reactive (i.e. antigenic) biomaterial implants can complicate and hinder this healing process. The degree to which healing is interrupted or delayed is dependent on multiple causes including: scale of the injury, the loss of architectural integrity, the level of necrosis, and the biomaterial interactions[57, 74, 203]. The occurrence of these events may facilitate the development of a foreign body response (FBR). This response is based on a sustained inflammatory reaction during the early healing process when there is granulation tissue formation[74]. Generally, the FBR is recognized by transient neutrophil granulocytes and the continued presence of macrophages (both mononuclear and polynuclear [e.g. multinucleated foreign body giant cells (MFBGCs)]) and lymphocytes within the granulation tissue substrate. As long as there is a chronic inflammatory cell presence, the healing process is arrested. Furthermore, this sustained inflammatory reaction, which is believed to be attributed to nonspecific protein adsorption and material independent, may yield a denser tissue compartment. For an implanted biosensor membrane, this compact fibrous capsule may vary from 50-200 μm and could further obstruct the interaction between the biosensor, its external interrogating device, and the target analyte[76, 121, 208, 209].

For either their resistance to protein adsorption or cellular adhesion, numerous studies have concentrated on passive or "anti/non-fouling" polymeric materials to effectively minimize the FBR, including: poly(hydrocyethylmethacrylate) (PHEMA)[119, 120], poly(tetrafluoroethylene) (PTFE)[101, 102, 115, 121], poly(vinyl alcohol) (PVA)[102, 115], and poly(ethylene glycol)diacrylate (PEG-DA)[63, 118]. However, *in vivo* investigations with each of these materials have shown the presence of a fibrous capsule surrounding the

implant of at least 50 μm[115, 118-121, 210]. In contrast, the "self-cleaning", thermoresponsive hydrogel described herein employs an active or "cell-releasing" method to physically detach adsorbed cells from its surface[122, 123, 125, 211].

Thermoresponsive poly(*N*-isopropylacrylamide) (PNIPAAm) hydrogels experience rapid deswelling and reswelling when temperature modulated above and below, respectively, their volume phase transition temperature (VPTT)[125, 144, 155, 158, 211, 212]. Previously, we reported a double network nanocomposite (DNNC) hydrogel composed of an interpenetrating, asymmetrically cross-linked PNIPAAm matrix with polysiloxane nanoparticles (~200 nm diameter) embedded during the formation of the first network[123]. For implantation into subcutaneous tissue, a plausible location for a biosensor, we investigated the thermosensitivity, cytocompatibility, and "self-cleaning" behavior *in vitro* using an external heating system[122]. Although DNNC cellular release displayed promising results *in vitro*, *in vivo* environments are significantly more complex. Thus, the objective of this work is to assess and compare the breadth of the FBR between DNNC and PEG-DA implants *in vivo* under normal temperature fluctuations via physical and environmental conditions - without the need for an external heating system. PEG-DA serves as non-thermoresponsive controls whose antifouling behavior and biocompatibility is well-established.

3.3. Materials and Methods

3.3.1. Materials

N-Isopropylacrylamide (NIPAAm, 97%), *N*-vinylpyrrolidone (NVP), and poly(ethylene glycol)diacrylate (PEG-DA, MW 575 g/mol) were purchased from Sigma-Aldrich (St. Louis, MO). *N*,*N*'-methylenebisacrylamide (BIS, 99%) was purchased from Acros Organics (Geel, Belgium). 2-Hydroxy-2-methyl-1-phenyl-1-propanone (Darocur 1173) and 1-[4-(2-Hydroxy)-phenyl]-2-hydroxy-2-methyl-1-propane-1-one (Irgacure 2959) was purchased from Ciba Specialty Chemicals (Tarrytown, NY). Octamethylcyclotetrasiloxane (D4) and 1,3,5,7-tetra-methyl-1,3,5,7-tetra¬vinylcyclotetrasiloxane (D4Vi) came from Gelest, Inc. Dodecylbenzene-sulfonic acid (DBSA, BIO-SOFT® S-101) came from Stepan Co. (Northfield, IL). For hydrogel fabrication and other experiments, deionized water (DI H2O) with a resistance of 18 MΩ·cm (Millipore, Billerica, MA) was used.

3.3.2. Polysiloxane Nanoparticle Preparation

Polysiloxane colloidal nanoparticles with an average diameter of ~200 nm were prepared via emulsion polymerization and purified via dialysis as previously reported.[125] The final emulsion was 4.8 wt% solids.

3.3.3. PEG-DA Hydrogel Preparation

Precursor solutions were formed by vortexing DI H2O, PEG-DA (100 %v/v) and Darocur 1173 (1% v/v) for 1 min. Cylindrical hydrogels (~1.5 mm x 5 mm, diameter x length per electronic caliper) were prepared by pipetting the precursor solution into a hollow cylindrical glass mold (inside diameter = 1.0 mm, length = 15 mm) with one end sealed by Parafilm. After sealing the other end of the mold, it was likewise exposed to longwave UV light as above at room temperature (RT) for 3 sec. The cylindrical hydrogel was removed from the mold, rinsed with DI H2O and immersed in a Petri dish containing DI H2O (60 mL) for 24 hours. A clean razor blade was used to equally trim the ends to reduce the length to 5 mm.

3.3.4. DNNC Hydrogel Preparation

DNNC hydrogels were prepared by sequential formation of a relatively tightly crosslinked 1st network containing polysiloxane nanoparticles (2 wt% solid nanoparticles based on NIPAAm weight) and a loosely crosslinked 2nd network.[123] The "1st network precursor solution" was formed by combining NIPAAm monomer (1.0 g), NVP co-monomer (0.16 g), BIS crosslinker (0.04 g), polysiloxane nanoparticle emulsion (0.485 g), Irgacure-2959 photoinitiator (0.08 g) and DI H2O (6.54 g). The "2nd network precursor solution" was formed by combining NIPAAm (6.0 g), NVP (0.96 g), BIS (0.012 g), Irgacure 2959 (0.24 g), and DI H2O (21.0 g). Cylindrical hydrogels (~1.5 mm x 5 mm, diameter x length) were prepared by pipetting the precursor solution into a cylindrical glass mold (inside diameter = 1.0 mm, length = 15 mm). The mold was

immersed in an ice water bath (~7 °C) and exposed for 10 min to longwave UV light. Cylindrical hydrogels were removed from their molds, rinsed with DI H2O, and soaked in a Petri dish containing DI H2O (60 mL) for 2 days at RT with daily water changes. A SNNC cylindrical hydrogel was then transferred into a Petri dish containing the 2nd network precursor solution for 24 hours at RT. The cylindrical hydrogel was then placed into a second cylindrical mold (diameter = 1.5 mm, length = 15 mm), submerged in an ice water bath (~7 °C), exposed for 10 min to longwave UV light and soaked in DI H2O as above. A clean razor blade was used to trim ends to reduce the cylindrical length to 5 mm. The final diameter was measured via calipers.

3.3.5. IACUC Approval

NIH guidelines for the care and use of laboratory animals (NIH Publication #85-23 Rev. 1985) have been observed. All animal investigations conducted were approved by the Texas A&M University Institutional Animal Care and Use Committee and fell under the Animal Use Protocol #2012-191.

3.3.6. "Self-Cleaning" In Vivo

Cylindrical PEG-DA (control) and DNNC (diameter~1.5 mm, length~5 mm) membranes were sterilized by exposure to 80% ethanol for 45 minutes. All hydrogel rods were then washed three separate times for 30 minutes with sterile Dulbecco's phosphate buffer solution. Disposable, sterile trocar needles (13G; inner diameter=1.804 mm, Avid Identification Systems, Inc.) were utilized to inject one of each cylindrical

polymer into the subcutaneous tissue (2~3 mm in depth) on the dorsal of CD® Hairless rats (N=20, male, 8 weeks old, Charles River Laboratories). The CD® Hairless rat specie encompasses a normal immune response despite its abnormal, reduced hair growth. The rat's hairless characteristic is ideal to facilitate the membrane implantation without unwarranted skin irritation commonly associated with shaving and Nair™-ing. Using isoflurane by inhalation, animals were anesthetized and anesthesia depth was tested by foot pinch reaction. Following implantation, the injection site was closed with surgical adhesive (3M Vetbond™ Tissue Adhesive, No. 1469SB). Material composition and dorsal placement were recorded for each rat/implant. All animals were immediately returned to individual cages and monitored every 12 hours. A custom designed LabView program (National Instruments) recorded cage temperatures every 5 mins. After either 7 or 30 days post implantation, 10 animals were euthanized by CO_2 asphyxiation, photographed, evaluated for gross changes and immediately fixed in 10% neutral buffered formalin for one week. Finally, implants and their surrounding tissue were removed and processed for histology by serial dehydration, paraffin embedding, sectioning, and staining (hematoxylin and eosin (H&E)).

3.3.7. Implanted DNNC Thermocycling Simulation

A 1-dimensional subcutaneously implanted DNNC computational model was developed using COMSOL Multiphysics software (COMSOL, Inc., Los Angeles, CA). The model accounted for thickness, thermal conductivity, density, specific heat, temperature (air), temperature (body), perfusion rate, and metabolic activity for air,

epidermis, dermis, DNNC hydrogel, subcutaneous tissue, and blood, as outlined in **Table 3.1.**. A 24 h segment of atmospheric cage temperatures recorded over the implant durations was best-fit to a Fourier function and implemented to simulate the atmospheric air temperature oscillations. Conducting a time-dependent, heat transfer study, the average temperature across the implanted DNNC hydrogel diameter was simulated. Previously reported DNNC thermosensitivity data was best-fit to a linear function spanning the simulated implanted DNNC temperature range. This linear function was then used to determine the potential dimensional change with respect to the simulated implanted DNNC temperature.

3.4. Results and Discussion

3.4.1. "Self-Cleaning" In Vivo: Fibrous Encapsulation

One sterile cylindrical PEG-DA (control) and DNNC (diameter~1.5 mm, length~5 mm) membrane were each implanted into the dorsal subcutaneous tissue (1~3 mm in depth) lateral to the spine of CD® Hairless rats (N = 20, male, 8 weeks old, Charles River Laboratories). At 7 and 30 days post implantation, 10 and 10 animals, respectively, were euthanized by CO_2 asphyxiation, photographed, evaluated for gross changes and immediately fixed in 10% neutral buffered formalin for at least one week. The implants and their surrounding tissue were then harvested and processed for histology by serial dehydration, paraffin embedding, sectioning, and staining (hematoxylin and eosin [H&E]). Gross appearances of the DNNC and PEG-DA

membranes confirmed that each hydrogel remained intact following implantation and for the duration of 7 (**Fig. 3.1.a,b**) or 30 (**Fig. 3.2.a,b**) days. Histological evaluation post 7 days conveyed insignificant differences between DNNC and PEG-DA implants. At this time point, cellular presence around both material compositions consisted mainly of fibroblasts followed by macrophages, lymphocytes, eosinophils, and neutrophils (**Fig. 3.3.**). The minute neutrophil population and increased fibroblast presence indicated an atrophying acute inflammatory response and a developing FBR. This further implies that the DNNC hydrogel composition is as inert and biocompatible as PEG-DA. The loose, unorganized collagenous tissue width surrounding the DNNC (**Fig. 3.1.c,e**) and PEG-DA (**Fig. 3.1.d,f**) hydrogels was measured at multiple points that resulted in 42.27 ± 11.78 μm and 51.22 ± 12.06 μm, respectively (**Fig. 3.4.**) across all animals with an average standard deviation of 55.5% (DNNC) and 49.7% (PEG-DA) within an animal.

At 30 days, a subacute FBR was exhibited. Although the total approximate number of cells declined, the percentage of fibroblasts, macrophages, and lymphocytes remained similar between both implants (**Fig. 3.3.**). However, further histological analysis revealed distinct differences between DNNC and PEG-DA membranes. Of particular importance were the fibrous capsule thicknesses and microvascular presence. A matured, organized, and denser fibrous capsule was observed surrounding the DNNC (**Fig. 3.2.c,e**) and PEG-DA (**Fig. 3.2.d,f**) hydrogels. As shown in Fig. 3.4., a thinner fibrous capsule resulted with DNNC membranes (30.06 ± 6.58 μm) in contrast to PEG-DA hydrogels (44.85 ± 11.11 μm) across animals with an average standard deviation of 32.3% (DNNC) and 29.3% (PEG-DA) within an animal. A significant difference was

also noticed regarding the degree of fibrous tissue organization between 7 and 30 day DNNC than between 7 and 30 day PEG-DA.

Blakney et al. witnessed a change in macrophage morphology and cytoskeletal organization from round to spread as PEG-DA hydrogel stiffness was increased[98]. Their findings suggested that macrophages were less sensitive to softer hydrogels, possibly due to integrin-mediated phenomenon, and that the round morphology with no apparent cytoskeletal arrangement reduced their activation; thereby, decreasing tumor necrosis factor-alpha (TNF-α), interleukin-1beta (IL-1β), and interleukin-6 (IL-6) expression, and forming a thinner surrounding fibrous layer *in vivo*.

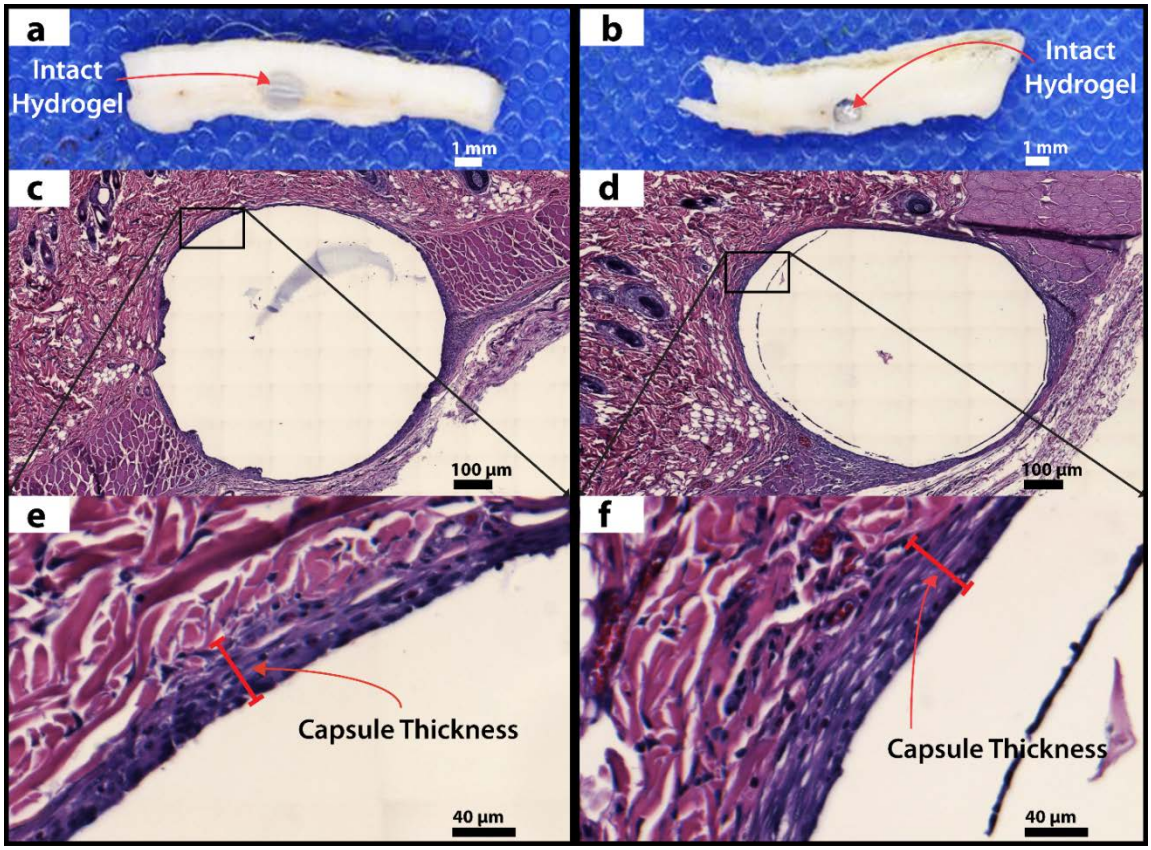

Figure 3.1. | CD® Hairless rat model subcutaneous implanted hydrogel sectioning and histology post 7 days. a,b, Gross sections of extracted dorsal subcutaneous tissue implanted with DNNC **(a)** or PEG-DA **(b)** intact after 7 days. **c,d,** H&E stained histology of tissue surrounding the DNNC **(c)** and PEG-DA **(d)** hydrogels. **e,f,** H&E stained histology conveying the development and degree of fibrous encapsulation for DNNC **(e)** and PEG-DA **(f)**.

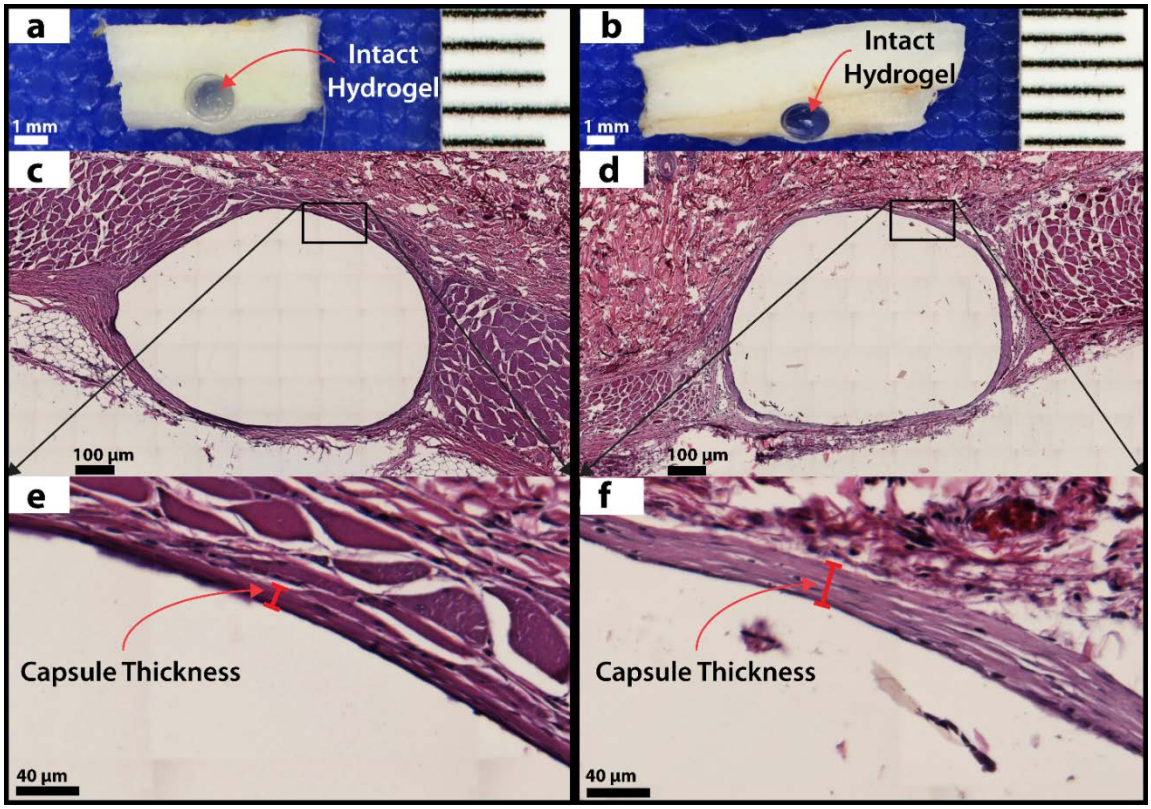

Figure 3.2. | CD® Hairless rat model subcutaneous implanted hydrogel sectioning and histology post 30 days. a,b, Gross sections of extracted dorsal subcutaneous tissue implanted with DNNC **(a)** or PEG-DA **(b)** intact after 30 days. **c,d,** H&E stained histology of tissue surrounding the DNNC **(c)** and PEG-DA **(d)** hydrogels. **e,f,** H&E stained histology displaying the extent of organized fibrous tissue encapsulating DNNC **(e)** and PEG-DA **(f)**.

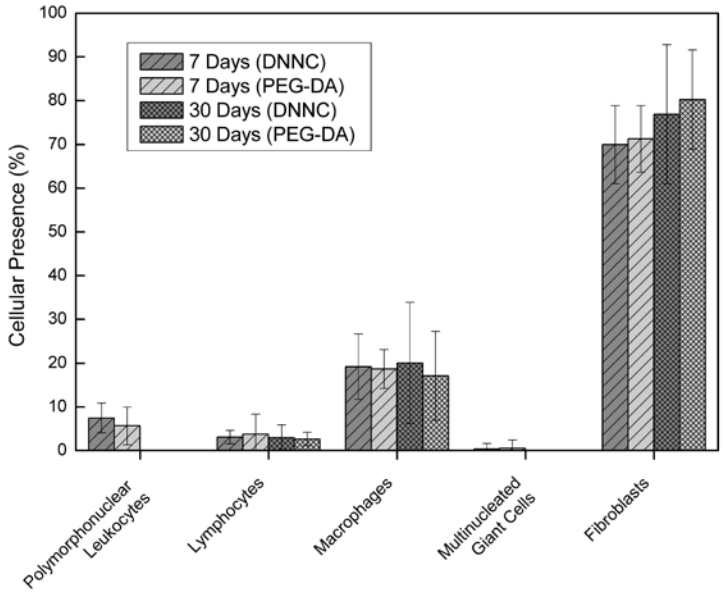

Figure 3.3. | Cellular types surrounding hydrogel implants. Graphical analysis displaying the various cell types and their approximate percentage adjacent to DNNC and PEG-DA hydrogel implants after 7 and 30 days.

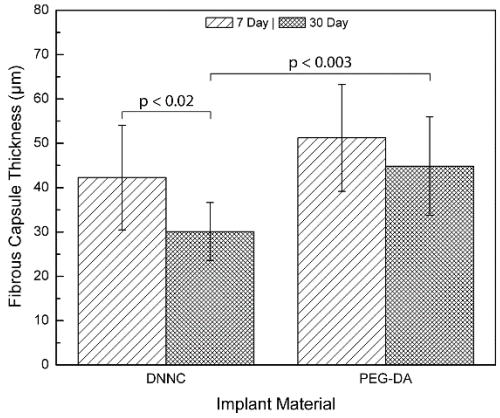

Figure 3.4. | Mean fibrous capsule thicknesses. The average thickness of the fibrous tissue capsules surrounding DNNC (7 days: N=10, M=42.27 μm, SD=11.78 μm; 30 days: N=9, M=30.06 μm, SD=6.58 μm) and PEG-DA (7 days: N=10, M=51.22 μm, SD=12.06 μm; 30 days: N=10, M=44.85 μm, SD=11.11 μm) hydrogels. A statistical two-tail t-test was performed between 7 and 30 day DNNC ($t(17)=2.74$, $p=0.014$) and between 30 day DNNC and PEG-DA ($t(17)=3.48$, $p=0.0029$). Error bars indicate one standard deviation from the mean.

3.4.2. "Self-Cleaning" In Vivo: Angiogenesis

Angiogenesis, the physiological formation of new blood vessels from pre-existing vessels, was quantified by evaluating the presence of blood vessels (10-100 μm in diameter) within 1 mm of the superficial half of the polymer interface (**Fig. 3.5.a-d**). It was determined that DNNC hydrogels had a higher density (vessels per mm^2) than PEG-DA hydrogels post 30 days (**Fig. 3.5.e**).

In 1995, Brauker *et al*. investigated FBRs provoked by numerous polymer membranes with varying pore sizes (0.02-15 μm)[101]. They reported that pore size, regardless of chemical makeup, appeared to be the principal determinant of the FBR, where pore sizes between 5-15 μm elicited a response more closely related to ideal (i.e. normal) wound healing. They also noted that this pore size range exhibited an increase in blood vessels in close proximity to the polymer implant[101, 213, 214]. Padera and Colton explored the vascularization timeframe associated with microporous membranes subcutaneously implanted in rats[215]. Their study revealed vascular growth adjacent to the implant within 10 days. Both groups further reported that neovascularization near the implant interface endured for almost a year in stark contrast to normal wound healing, where vessels usually begin to regress by the second week[214, 215]. Ensuing research has probed implant porosity optimization to curtail the FBR, and has indicated that 30~60 μm pores seem to evoke the thinnest fibrous capsules while driving the most extensive level of neovascularization[102, 104-106]. It has been theorized that inflammatory cells, specifically macrophages, may infiltrate microporous materials, and in doing so, may experience localized reduced oxygen partial pressure. Assuming a sufficiently large pore

size where macrophages seem to preserve a spherical morphology, the hypoxic event may then instigate macrophages to discharge angiogenic factors, some of which have chemotactic and mitogenic activity[214-221]. As macrophages attach and develop a spread morphology, the gene expression pattern deviates to one that encourages fibroblast proliferation, even in a hypoxic state. It is speculated that vascular endothelial growth factor/vascular permeability factor (VEGF/VPF)[222, 223] and TNF-α[224, 225] may be the key components promoting angiogenesis as these factors have been shown to be secreted by macrophages within hypoxic environments. This suggests that the larger DNNC pore sizes reported by Fei *et al*. may further impede macrophage adhesion and spreading, while simultaneously motivating neovascular growth[123].

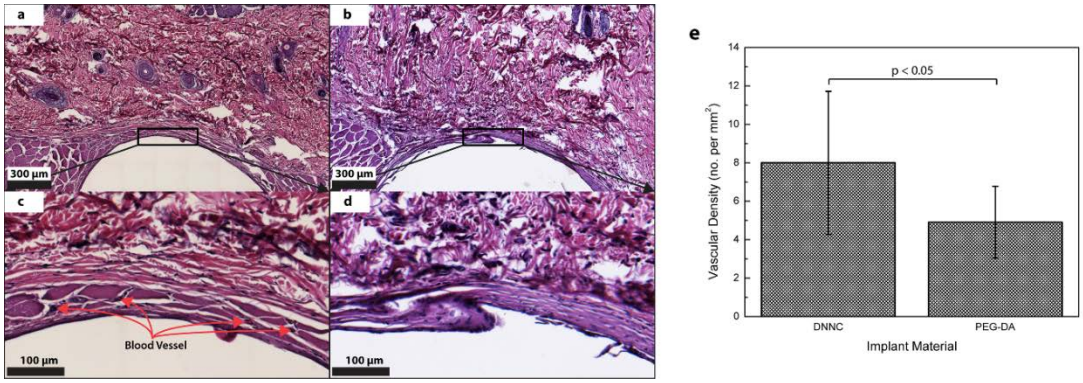

Figure 3.5. | Mean microvascular density. a,b, H&E stained histology of tissue surrounding DNNC **(a)** and PEG-DA **(b)** hydrogel implants post 30 days. **c,d,** Magnified H&E stained sections from similar positions on **a** and **b**, respectively, displaying blood vessels adjacent to the implant surface. **e,** Graphical representation of neovascular density (vessels per mm^2) for vessels with a diameter of 10-100 µm within 1 mm of the superficial half of the DNNC (N=9, M=8.00, SD=3.72) or PEG-DA (N=10, M=4.91, SD=1.87) hydrogel implant interface. A statistical two-tail t-test was conducted ($t(12)=2.25$, $p=0.044$). Error bars indicate one standard deviation from the mean.

3.4.3. Implanted DNNC Thermocycling Simulation

Regarding hydrogel mobility, Fan et al. investigated macrophage behavior on PNIPAAm and observed that as their PNIPAAm film thickness grew to 4 μm, it became "increasingly cell repulsive"[226]. They attributed this increase to the heightened mobility of the polymer's chains, which in turn, augmented hydration. Thus, the increase in hydrophilicity which is unfavorable for protein adsorption that arbitrates cellular adhesion, may decrease cellular activity of the FBR (e.g. MFBGCs), and ultimately, diminish the size of the fibrous capsule[203, 206, 226]. Interestingly, Fan et al. also noticed that initially attached macrophages to the PNIPAAm surface remained inactivated and retained their surface receptor profile after detachment when the temperature was adjusted[226]. This could imply that a continually changing surface may foster perpetual cellular detachment without evoking a more severe FBR. To evaluate the potential DNNC hydrogel dimensional alterations *in vivo*, a COMSOL Multiphysics computational model was developed. Conducting a time-dependent heat transfer study, a 1-dimensional subcutaneously implanted DNNC representation was constructed incorporating air, epidermis, dermis, subcutaneous tissue, DNNC membrane, and blood factors, as outlined in **Table 3.1.**. A 24 h segment of atmospheric animal cage temperatures recorded over the implant durations was best-fit to a Fourier function (**Fig. 3.6.a**) and used to simulate the air temperature fluctuations. The computational model also accounted for rat core body temperature oscillations and metabolic heat production[227-230]. The simulation results conveyed an average temperature of 31.6 °C with an amplitude of 1.2 °C across the DNNC membrane at an implant depth of 2.08

mm, as shown in **Fig. 3.6.b**. Based on the previously reported DNNC hydrogel's thermosensitivity, this maximum 1.2 °C temperature oscillation correlates to a maximum dimensional change of ~26 μm, assuming the DNNC hydrogel's initial diameter after implantation was 1.5 mm (**Fig. 3.6.c,d**)[122]. The simulation demonstrated that over a 24 h period, the DNNC membrane would undergo constant dimensional alterations while remaining in a relatively high hydrophilic state well below its VPTT. This suggests a potential decrease in nonspecific protein adsorption on the DNNC surface, which would prompt a decline in macrophage adhesion. Furthermore, the ceaseless DNNC thermoresponse would hinder attached macrophages from developing a spread morphology and cytoskeletal architecture.

Air	
Thickness	500 μm [231]
Thermal conductivity	0.0263 W m^{-1} K^{-1} [231]
Density	1.3 kg m^{-3} [231]
Specific heat	1004 J kg^{-1} K^{-1} [231]
Temperature	298.05 ± 0.8 K

Epidermis	
Thickness	80 μm [231, 232]
Thermal conductivity	0.23 W m^{-1} K^{-1} [231-233]
Density	1200 kg m^{-3} [231, 232]
Specific heat	3590 J kg^{-1} K^{-1} [231, 232]
Perfusion Rate	0 s^{-1} [231, 232]

Table 3.1. | Heat transfer computational simulation parameters. Input parameters for each layer in the 1-dimensional subcutaneously implanted DNNC representation.

Dermis	
Thickness	2000 μm [231, 232]
Thermal conductivity	0.45 W m^{-1} K^{-1} [231-233]
Density	1200 kg m^{-3} [231, 232]
Specific heat	3300 J kg^{-1} K^{-1} [231, 232]
Perfusion Rate	1.25 x 10^{-3} s^{-1} [231, 232]

DNNC Hydrogel	
Thickness	1500 μm
Thermal conductivity	0.58 W m^{-1} K^{-1}
Density	0.2125 g cm^{-3}
Specific heat	630 J kg^{-1} K^{-1} [234]

Subcutaneous Tissue	
Thickness	16500 μm [231, 232]
Thermal conductivity	0.19 W m^{-1} K^{-1} [231, 232]
Density	1000 kg m^{-3} [231, 232]
Specific heat	2675 J kg^{-1} K^{-1} [231, 232]
Perfusion Rate	1.25 x 10^{-3} s^{-1} [231, 232]

Blood	
Density	1060 kg m^{-3} [231, 232]
Specific heat	3770 J kg^{-1} K^{-1} [231, 232]

Miscellaneous	
Metabolic Activity	5100 W m^{-3} [227, 228, 230]
Core body Temperature	310.59 ± 0.42 K [229]

Table 3.1. Continued

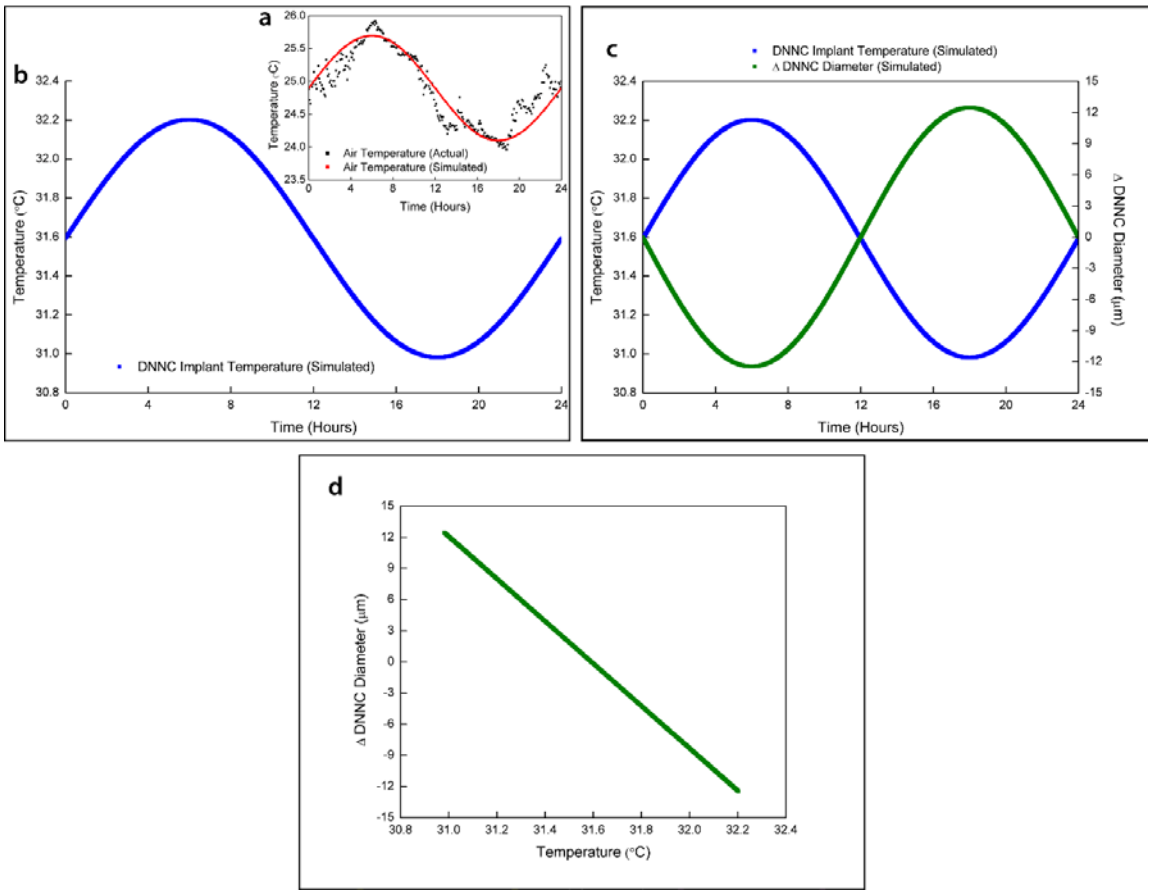

Figure 3.6. | Computational modeling of DNNC dimensional changes due to temperature fluctuations subcutaneously implanted. a, Simulated animal cage air temperature overlaid on actual temperatures collected over a 24 h period. **b,** Simulated temperature at DNNC hydrogel implant depth (2.08 mm) over a 24 h duration. **c,** Modeled DNNC membrane diameter change as a function of the simulated implant depth temperature **(b)**. **d,** DNNC membrane thermosensitivity assuming the initial diameter post implantation was 1500 µm.

3.5. Summary

"Self-cleaning", thermoresponsive DNNC membranes and PEG-DA hydrogels were successfully implanted into the subcutaneous dorsal tissue of a rat model, and post 7 and 30 days, these implants were extracted intact. Histological examination of the

surrounding tissues revealed properties associated with the FBR, which produced a matured fibrous capsule after 30 days. This capsule was significantly less thick encircling DNNC compared to PEG-DA hydrogels. In addition, a noticeable neovascular growth was observed surrounding DNNC membranes in contrast to the PEG-DA. To assess the possible extent of DNNC dimensional fluctuation, a time-dependent, heat transfer, computational model was generated. The simulation conveyed a continuous dimensional shift with a maximum change of ~26 μm which may effectively promote cellular detachment. Although this study did not explore the underlying mechanism(s) triggering a diminished FBR while inducing angiogenesis, it was hypothesized and appears plausible (based on the modeling and the literature) that the DNNC hydrogel's lack of stiffness, augmented hydrophilicity, and enlarged average pore size, essentially, hampered macrophage adhesion, dispersion, and activation to boost the FBR. Further, the increased neovascularization neighboring the DNNC hydrogel gives evidence to an amplified exudation of angiogenic growth factors, most likely stemming from spherically shaped macrophages lying on or potentially infiltrating the surface.

Ultimately, the minimal fibrous capsule formation and maximum neovascular growth around the DNNC hydrogel is ideal for a biosensor membrane in order to decrease sensor lag time and improve its accuracy over the extent of its lifespan. Although the hydrogel shows tremendous potential to deter biofouling, in order to advance as a membrane for a glucose biosensor, its ability to house and enable the functionality of a glucose-sensing chemistry must be investigated.

CHAPTER IV

ENCAPSULATION OF A GLUCOSE-SENSING CHEMISTRY WITHIN A "SELF-CLEANING" MEMBRANE*

4.1. Overview

Toward the development of a continuous glucose monitoring (CGM) system, the lectin, Concanavalin A (ConA), has been utilized as a component in a Förster resonance energy transfer (FRET), competitive, glucose binding assay. However, at physiological pH, native ConA exhibits a net negative charge that contributes to non-specific binding among ConA as well as with potential electrostatically charged, assay-delivery carriers; decreasing its ability to function as part of a glucose-sensing assay. Therefore, to minimize non-specific binding and increase resistance to electrostatic surfaces for a delivery scheme, ConA was conjugated with monomethoxy-poly(ethylene glycol) (mPEG), a process referred to as "PEGylation". Native and fluorescently labeled ConA were successfully PEGylated with monomethoxy-poly(ethylene glycol)-N-hydroxylsuccinimide(succinimidyl carbonate) (mPEG-NHS(SC)), which showed to decrease the electrostatic interactions with a charged layer-by-layer (LbL) assembly

* Parts of this chapter are reprinted with kind permission from "PEGylation of Concanavalin A to decrease nonspecific interactions in a fluorescent glucose sensor" by Alexander A. Abraham, Brian M. Cummins, Andrea K. Locke, Melissa A. Grunlan, and Gerard L. Coté, 2014. *SPIE BiOS*, 2014. p. 895112-895112-895115, Copyright 2014 by International Society for Optics and Photonics.

surface (poly(styrene sulfonate) [PSS] / poly(allylamine hydrochloride) [PAH]) while maintaining a similar binding affinity of native ConA to the competing ligand. The FRET response of APTS labeled ligand (donor) conveyed an increase in fluorescence intensity with increasing glucose concentrations in free solution. Upon conveying its potential, this assay was successfully encapsulated within calcium carbonate-dissolved LbL microspheres and then embedded within a biocompatible SN hydrogel. Although the encapsulated assay lacked a definitive FRET response to varying glucose concentrations, confocal microscopy confirmed the assay's homogenous encapsulation feasibility – conveying the potential of this FRET-based glucose-sensing assay and its delivery systems as an approach for a continuous glucose monitor.

4.2. Introduction

Striving to enhance CGM systems that require fewer calibrations with extended lifetimes, fluorescent affinity biosensors that utilize ConA is one tactic under heavy consideration[54, 235-238]. ConA, a carbohydrate-binding lectin derived from the jack bean, resides as a tetramer with four identical monomer sub-components (MW~25 kDa)[239-241]. With the capacity to reversibly bind to glucose molecules (affinity~400 M^{-1}), ConA is an appealing tool to survey physiological glycemic levels[242].

Although ConA has been used previously in optical competitive binding systems for the continuous detection and quantification of glucose concentrations, its deliverability and especially its stability have remained issues[2, 243-247]. Aggregation is one

well-known cause of its instability. In its tetrameric state, ConA offers four sites that can result the multiple bindings when coupled to multivalent ligands. However, recently a suitable, fluorescent, competing ligand labeled with 8-aminopyrene-1,3,6-trisulfonic acid trisodium salt (APTS) has been engineered that presents a single high affinity trimannose moiety to ConA (APTS-MT)[248]. Though, ConA still has a net negative charge that contributes to non-specific binding among itself as well as with any electrostatically charged surfaces. These forms of uncontrolled binding can produce aggregates that will eventually precipitate out of solution, and thereby reduce the protein's lifetime and efficiency in a competitive binding assay.

A method utilized to improve the stability of ConA was implemented that covalently conjugates mPEG chains to protein surface molecules (i.e. PEGylation)[249-251]. It is believed that this process improves the solubility and stability of proteins as an effect of a hydrophilic cloud that stems from the attached PEG chains[252]. The highly mobile, hydrophilic, neutrally-charged PEG chains also may deliver a steric hindrance effect that could minimize particle-to-particle interactions by essentially masking the protein's surface charges. This, however, is dependent of the chains molecular weight (i.e. size) and the number of chains grafted to the protein's surface[250, 251, 253]. In addition to reducing particle interaction, this technique may provide resistance to non-specific electrostatic interactions between ConA and charged surfaces, which expands the options for a delivery system.

A wide variety of microencapsulating delivery schemes exist using polymers such as PEG[235, 237, 254], agarose[255-257], and alginate[258, 259] for fluorescent assays. However,

the ideal encapsulating method must, at the very least, meet the requirements of the sensing assay. The FRET-based, competitive binding assay employed here between ConA labeled with tetramethylrhodamine isothiocyanate (TRITC) and APTS-MT is spatial displacement dependent and contains both high and low molecular weight components. Therefore, the chosen encapsulation scheme should provide a cavity for assay motility and a barrier that impedes the diffusion of the smallest molecular component (APTS-MT) while permitting the target analyte, glucose, to diffuse freely. Further, since ConA is a protein that can denature, the encapsulation process must limit exposure to any potentially damaging conditions.

Now although PEG, agarose, and alginate polymer matrices have been utilized to contain assay components while simultaneously allowing diffusion of the target analyte, these polymers each have their drawbacks. Mannitol-driven porated PEG microspheres are non-biodegradable, biocompatible, and can provide hollow cavities for the FRET pair to bind and disassociate. However, these randomly positioned pores and the polymer's dense matrix make it difficult to control the assay concentration in and across microspheres and severely impedes glucose diffusion, respectively. Now, agarose and alginate are also biocompatible and capable of entrapping proteins within their matrices. Further, they are biodegradable and have difficulty containing low molecular weight components. In contrast, the method of layer-by-layer (LbL) adsorption appears promising as an entrapping system for both ConA-TRITC and APTS-MT. These polyelectrolyte assemblies, formed by alternating polyanions and polycations, produce an electrostatic, multilayer, thin film, whose permeability can be controlled by simply

adjusting the number of layers in the assembly and the strength of the chosen polyelectrolytes[260, 261]. In order to form an assembly, an initial charged substrate or template is required. Though a variety of templates exist such as silica[262], manganese carbonate[263], cadmium carbonate[264], melamine formaldehyde[265, 266], poly(lactic)[267] or poly(lactic-co-glycolic acid)[267], the biocompatibility of negatively charged calcium carbonate microspheres and their capability for being processed under physiological conditions, makes them a suitable choice to entrap ConA-TRITC and APTS-MT[260, 261]. Once a LbL assembly is placed on the calcium carbonate surface, this template may then be dissolved gently with ethylenediaminetetraacetic acid disodium salt dehydrate (EDTA) and without the addition of an acid, to yield a hollow microsphere with a thin LbL shell encapsulating the assay's components.

Herein, mPEG-NHS(SC) chains, polymer chains reactive toward primary amine groups, were conjugated to the surface of ConA. The extent of PEGylation to ConA, the mPEG-ConA's binding affinity, and the protein's resistance to a charged LbL assembly surface of poly(styrene sulfonate) (PSS) and poly(allylamine hydrochloride) (PAH) were then evaluated. Since PSS/PAH are one of the most studied, stable, robust and commercially available polyelectrolyte pairs, they were chosen for the LbL assembly. Further, mPEG-ConA was labeled with TRITC which produced a FRET response with APTS-MT when the glucose concentrations were varied in free solution. Finally, towards the progression of an implantable glucose biosensor, the assay was encapsulated within dissolved calcium carbonate LbL-assembled microspheres, which were then embedded within a SNNC hydrogel.

4.3. Materials and Methods

4.3.1. Materials

Concanavalin A Type IV lyophilized powder (ConA), poly-(allylamine) solution (PAH), poly-(sodium 4-styrenesulfonate) (PSS), Trizma® hydrochloride (Tris-HCl), manganese(II) chloride tetrahydrate, methyl α-D-mannopyranoside (MADM), hydrochloric acid (HCl), sodium hydroxide (NaOH), sodium bicarbonate ($NaHCO_3$), apoly-(ethyleneimine) (PEI) solution, NIPAAm (97%), sodium carbonate (Na_2CO_3), and ethylenediaminetetraacetic acid disodium salt dehydrate (EDTA) were purchased from Sigma-Aldrich (St. Louis, MO). Monomethoxy-poly(ethylene glycol)-N-hydroxylsuccinimide(succinimidyl carbonate) (mPEG-NHS(SC)) MW: 5 000 Da was obtained from Nanocs (New York, NY). Calcium chloride dehydrate and potassium persulfate ($K_2S_2O_8$) was purchased from Mallinckrodt Chemical, Inc. (St. Louis, MO). *N*,*N*'-methylenebisacrylamide (BIS, 99%) was purchased from Acros Organics (Geel, Belgium). 2-Hydroxy-2-methyl-1-phenyl-1-propanone (Darocur 1173) and 1-[4-(2-Hydroxy)-phenyl]-2-hydroxy-2-methyl-1-propane-1-one (Irgacure 2959) was purchased from Ciba Specialty Chemicals (Tarrytown, NY). Octamethylcyclotetrasiloxane (D_4) and 1,3,5,7-tetramethyl-1,3,5,7-tetravinylcyclotetrasiloxane (D_4^{Vi}) came from Gelest, Inc. Dodecylbenzenesulfonic acid (DBSA, BIO-SOFT® S-101) came from Stepan Co. (Northfield, IL). Fluorescamine, Concanavalin A, Tetramethylrhodamine isothiocyanate conjugate, and tetramethylrhodamine isothiocyanate (TRITC) came from Life Technologies (Grand Island, NY). Regenerative cellulose dialysis membranes (MWCO

8-10 kDa and 20 kDa) were purchased from Spectra/Por® (Rancho Dominguez, CA). Sodium chloride was obtained from J.T.Baker/Avantor Performance Materials (Center Valley, PA). 0.2 μm syringe filters were purchased from VWR (Radnor, PA). For sodium bicarbonate buffer solution, Tris buffer solution, and other experiments, deionized water (DI H2O) with a resistance of 18 MΩ·cm (Millipore, Billerica, MA) was used. Buffer solutions were pH adjusted with 1 M HCl and 1 M NaOH, verified with a pH meter (420 A+, Orion; electrode 599030, Cole-Parmer, Vernon Hills, IL).

4.3.2. PEGylation of Concanavalin A

ConA or ConA-TRITC was conjugated with mPEG-NHS(SC), a primary amine reactive PEG derivative with a succinimidyl carbonate linker that provides stability in aqueous solutions[268]. ConA (10 mg) was fully dissolved in 1 mL of sodium bicarbonate buffer solution (0.1 M sodium bicarbonate, 0.15 M sodium chloride, pH 8.5). To remove any initial aggregates, the solution was filtered using a 0.2 μm syringe filter. MADM was added to the ConA solution at a concentration of 1.9 mg mL^{-1} to protect the sugar binding site on each ConA monomer. Once fully dissolved, mPEG-NHS(SC) was incorporated at a molar ratio of 15:1 to that of ConA (MW 25,500 g/mol). The solution was placed on a rotating plate at room temperature (RT) for 6h and then allowed to sit on a bench top for an additional 18h at RT to slowly agitate the contents without denaturing of the protein. At the end of the reaction, the solution was separated for dialysis in a dialysis tube (MWCO 20 kDa) against either sodium bicarbonate buffer or Tris buffer (10 mM TRIS-HCl, 0.15 M NaCl, 1 mM $CaCl_2$, 1 mM $MnCl_2$, pH 7.4) for 24h with

multiple bath changes. After dialysis, the solutions were extracted from the dialysis membranes and stored in 1.5 mL centrifuge tubes.

4.3.3. Characterization of PEGylation

The extent of conjugation was assessed using fluorescamine (spiro(furan-2(3H),1'(3'H)-isobenzofuran)-3,3'-dione, 4-phenyl), a fluorescent, primary amine-binding dye. Due to the high sensitivity of fluorescamine, it is capable to bind to primary amines in as little as 50 ng of protein[250, 269]. The intensity of fluorescamine decreases as the extent of PEGylation increases since fewer primary amines groups are available. Solutions were prepared in sodium bicarbonate salt solution, pH 8.5. Known ConA and mPEG-ConA concentrations from 0 to 150 μg were placed in a centrifuge tube (1.5 mL) to which 0.5 mL of fluorescamine (0.3 mg mL^{-1} in acetone) was added. After approximately 7-10 mins, the fluorescence intensity of the solutions was measured using a TECAN Infinite 200 PRO (Tecan Group, Ltd, Männedorf, Switzerland) with an excitation and emission wavelength of 390 nm and 475 nm, respectively. The degree of PEGylation (DP) was calculated using the following equation:

$$DP\% = (1 - \frac{m_{mPEG-ConA}}{m_{ConA}}) \times 100$$

where *m* is the slope from the linear regression of the fluorescence intensity as a function of the protein concentration. The number of mPEG chains attached was determined by

distributing the DP to the maximum number of available primary amine groups on the surface of ConA.

4.3.4. Sugar Binding Affinity

Fluorescence anisotropy was utilized to examine the binding affinity of PEGylated ConA in comparison to native, unmodified ConA to a fluorescently labeled ligand, APTS-MT. APTS-MT (APTS, λ_{ex}: 470nm, λ_{em}: 520 nm) was measured in the presence of various protein concentrations up to 10 μM using an Infinite 200 PRO (Tecan Group, Ltd, Männedorf, Switzerland) outfitted with polarizers. A Boltzmann function was used to implement a sigmoidal fit from which the binding (k_a) and disassociation (k_d) constants could be calculated.

4.3.5. Non-Specific Electrostatic Interactions

Native ConA, at physiological pH, has a net negative charge that contributes to non-specific binding among ConA proteins as well as with potential electrostatically charged, assay-delivery carriers. To examine the ability of PEGylated ConA to resist these electrostatic charges, modified and unmodified ConA were introduced to a layer-by-layer (LbL) assembly. Multiple 300 μL polystyrene wells were initially treated with PEI, a highly positively charged polymer, followed by layers of PSS and PAH. LbL assemblies ending with PSS (mainly negatively charged surface) or with PAH (mainly positively charged surface) of 4 or 4.5 bilayers, respectively, were fabricated. PEGylated ConA (3.47 mg mL^{-1}) and native ConA (3.39 mg mL^{-1}) were injected into control

(neutrally charged polystyrene), PSS (negatively charged), and PAH (positively charged) surface wells. After 48h, the solutions were extracted and the protein concentration was measured by absorbance (280 nm).

4.3.6. Layer-By-Layer Microcapsules Entrapping Glucose-Sensing Assay Components

To become the acceptor in a FRET pair with APTS-MT, mPEG-ConA was labeled with TRITC (TRITC, λ_{ex}: 555 nm, λ_{em}: 580 nm). This was achieved by first dialyzing mPEG-ConA against 0.1 M $NaHCO_3$, pH 9.0 for 24h. mPEG-ConA was then removed, placed into a small glass beaker with a Teflon stir bar, and slowly stirred. TRITC (dissolved in DMSO at 10 mg mL^{-1}) was then slowly added at 1 mg mL^{-1} for every 1 mL of mPEG-ConA at a concentration of 10 mg mL^{-1}. This solution was allowed to reaction for 1~2h. Finally, the solution was dialyzed against TRIS buffer for 24h (MWCO 8-10 kDa).

For microencapsulation within a LbL assembly, the initial capsule cores were fabricated by adding 3 μM of mPEG-ConA-TRITC and 400 nM of APTS-MT to 0.33 M $CaCl_2$ while stirring at 300 rpm. 0.33 M Na_2CO_3 with 4 mg mL-1 PSS was then introduced at 1:1 ratio, and the solution was allowed stir for 30s. Afterwards, the stirring was stopped, and the solution was left to react for 15min at RT. The calcium carbonate core solution was transferred into 1 mL centrifuge tubes and centrifuged at 3000 rpm for 5min. The supernatant was extracted, and washed with 0.01 M NaCl (pH 7.5). The resuspended calcium carbonate core solution was centrifuged again (3000 rpm, 5min), and the supernatant was extracted once more. The cores were then alternatively soaked

in 300~500 μL of a 2 mg mL^{-1} solution of PAH or PSS, gently shaken for 30s, and sonicated for 10s. Between each polyelectrolyte layer, the calcium carbonate microspheres (CCMs) were centrifuged at 3000 rpm for 5min, the supernatant was discarded, the microspheres were resuspended in 0.01 M NaCl (pH 7.5), and centrifuged once more. After depositing 15 bilayers (ending with PSS as the outmost layer), the CCMs were suspended in 0.1 M EDTA (pH 7.4) and allowed to mix for 20min to dissolve the calcium carbonate core. The microspheres were then centrifuged (3000 rpm, 5min), the supernatant was discarded, and the spheres were resuspended in 0.1 M EDTA again for 20min. Finally, the microspheres were centrifuged, the supernatant was discarded, and the spheres were resuspended in TRIS buffer. After centrifuging once more and removing the supernatant, the calcium carbonate-dissolved LbL microspheres were resuspended in TRIS buffer.

For imaging, approximately 10 μL of the microsphere solution was smeared on a glass slide on which a slide cover was placed. Images were taken using a confocal microscope (Leica TCS SP5, Leica Microsystems, Inc., Buffalo Grove, IL) using sequential scanning with excitation wavelengths of 476 nm and 543 nm and either a 40x or 63x dry objective.

4.3.7. Thermoresponsive Hydrogel for Microsphere Embedding

Polysiloxane Nanoparticle Preparation. Polysiloxane colloidal nanoparticles with an average diameter of ~200 nm were prepared via emulsion polymerization and purified via dialysis as previously reported[125]. The final emulsion was 4.8 wt% solids.

SNNC Matrix. A SNNC planar hydrogel was used to embed the glucose-sensing microspheres. This hydrogel was formed by combining NIPAAm monomer (1.0 g), NVP co-monomer (0.16 g), BIS crosslinker (0.04 g), polysiloxane nanoparticle emulsion (0.485 g), Irgacure-2959 photoinitiator (0.08 g) and DI H_2O (6.54 g) with ~100 μL of microspheres. Planar hydrogel sheets (1 mm thick) were produced by pipetting the 1st network precursor solution into a mold consisting of two clamped glass slides (75 x 50 mm) separated by 1 mm thick polycarbonate spacers. The mold was then immersed into an ice water bath (~7 °C) and exposed to longwave UV light for 10min. The resulting single network nanocomposite (SNNC) sheet was removed from the mold, rinsed with DI H_2O and then soaked in TRIS buffer at RT for 24h with one buffer exchange.

4.3.8. FRET Responses

Free Solution: mPEG-ConA-TRTIC with APTS-MT. The FRET response between 3 μM mPEG-ConA-TRITC and 100 nM APTS-MT was measured in the presence of various concentrations of glucose (0, 200, and 400 mg dL^{-1}). The fluorescence intensity spectra were recorded using an Infinite PRO 200 (Tecan Group, Ltd, Männedorf, Switzerland).

LbL Encapsulated mPEG-ConA-TRITC with APTS-MT Microspheres. The FRET response between 3 μM mPEG-ConA-TRITC and 400 nM APTS-MT encapsulated within LbL microspheres was measured in the presence of various concentrations of glucose (0, 100, 200, 400, and 600 mg dL^{-1}). The fluorescence intensity spectra were

recorded using an Infinite PRO 200 (Tecan Group, Ltd, Männedorf, Switzerland) after the microspheres had soaked for 5h in each glucose concentration.

4.4. Results and Discussion

4.4.1. Extent of PEGylation

A total of 12 lysine residual groups and one terminal amine group reside on the surface of a ConA monomer. Assuming the majority of mPEG chains conjugate to these surface primary amines, 13 is the maximum number of mPEG chains that produce amide bonds. Introducing fluorescamine to known concentrations of ConA and mPEG-ConA, the extent of PEGylation may be determined by the slope ratio of modified to unmodified ConA. As seen in **Figure 4.1.**, the fluorescence intensities increase linearly as the protein concentration increases. However, the reduced fluorescence from mPEG-ConA samples are assumed to be attributed to the reduced available primary amines. Upon implementing the DP equation, the result indicates that ~27% of the total available surface primary amines on ConA were conjugated. This correlates to 3~4 mPEG chains per ConA monomer.

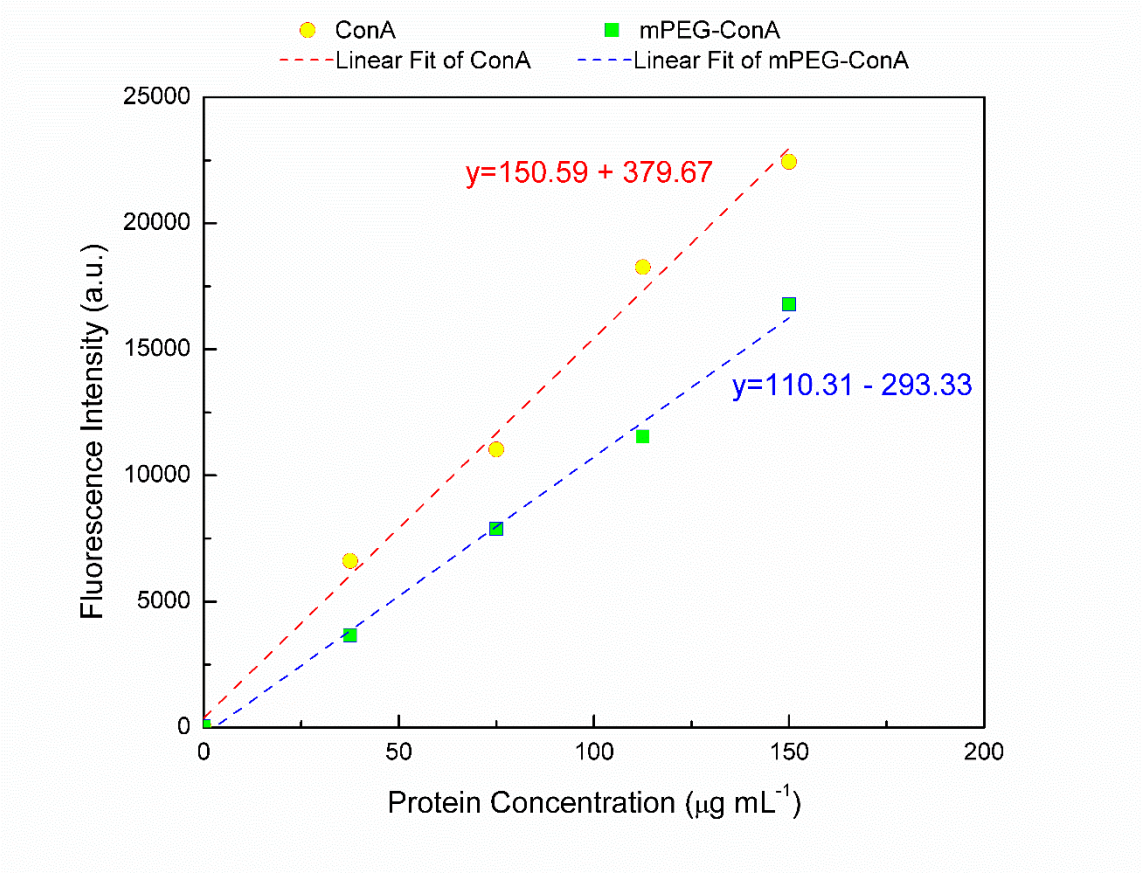

Figure 4.1. | Degree of PEGylation. The graph exhibits the fluorescamine fluorescence intensities of as a function of ConA and mPEG-ConA concentrations. The slope ratio (mPEG-ConA:ConA) is used to calculate the DP and thus approximates the number of conjugated mPEG chains to a ConA monomer.

4.4.2. mPEG-ConA Sugar Binding Affinity

Fluorescence anisotropy is a widely used method to determine the associating and disassociating constants of proteins[270-272]. Here, the anisotropy of the APTS-MT in the presence of mPEG-ConA and ConA was measured. **Figure 4.2.** displays the recorded anisotropy as a function of the logarithmic protein concentration. A Boltzmann function was applied, which produced a sigmoidal curve fit. Based on the function equation:

$$Y = A2 + \frac{(A1 - A2)}{1 + exp^{\frac{V_{50} - X}{m}}}$$

where *A1* is the maximum anisotropy value, *A2* is the minimum anisotropy value, *X* is the protein concentration, *m* is the slope, and V_{50} is the half maximum value as well as the disassociation constant (k_d), the binding or associating constant (k_a) was calculated to be 6.226±1.08 μM^{-1} (mPEG-ConA) and 6.498±1.06 μM^{-1} (ConA). Although the calculated binding constant for mPEG-ConA is lower than ConA while displaying higher anisotropies, the affiliated errors indicate that the affinities between native ConA and PEGylated ConA and are similar.

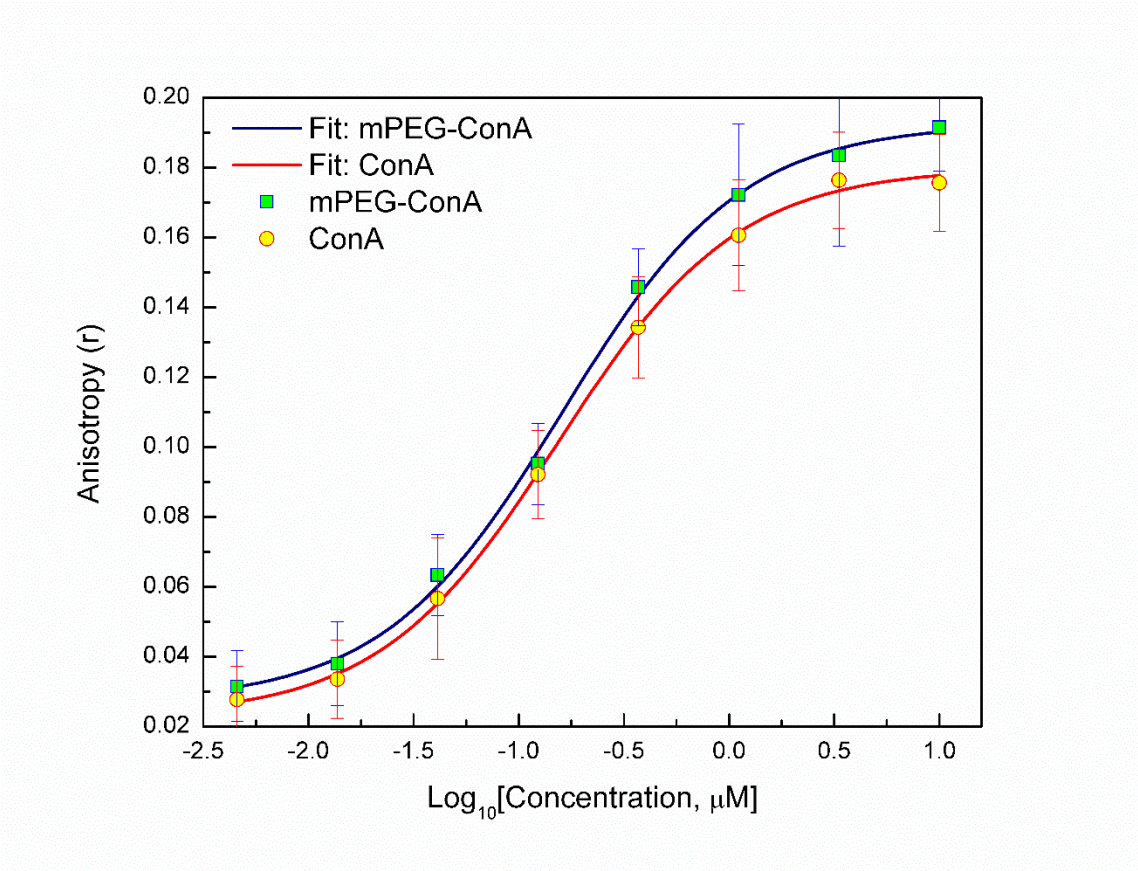

Figure 4.2. | mPEG-ConA and ConA binding affinities. Measured fluorescence anisotropies of APTS-MT in the presence of mPEG-ConA and ConA and their respective Boltzmann sigmoidal fits.

4.4.3. Non-specific Electrostatic Interaction Resistance

Non-specific binding of ConA due to electrostatic interactions reduces the protein's stability, lifetime, and efficiency in a competitive binding assay. To increase resistance to these charges, neutrally charged mPEG chains were grafted to ConA. PEGylated ConA (3.47 mg mL^{-1}) and native ConA (3.39 mg mL^{-1}) were introduced to planar LbL assemblies ending with either a positively or negatively charged surface

layer. After 48h, the exposed solutions were extracted and protein concentrations were measured via absorbance (280 nm) as seen in **Figure 4.3.** ConA and mPEG-ConA maintained their initial concentrations when exposed to a neutrally charged, polystyrene surface (control). In the presence of an electrostatically, mainly positively or negatively surface, mPEG-ConA continued to maintain its initial concentration whereas native ConA's concentration decreased. This decrease signifies the non-specific binding of unmodified ConA to the LbL assembly's charged surface layer.

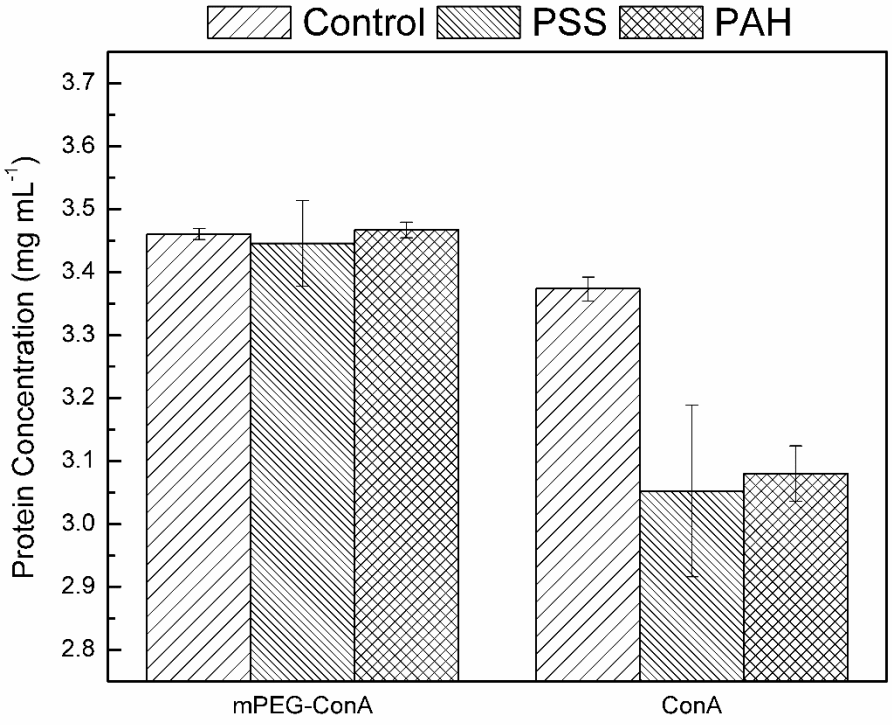

Figure 4.3. | Non-Specific electrostatic interaction. mPEG-ConA and native ConA supernatant concentrations after a 48h exposure to an electrostatically charged surfaces.

4.4.4. Layer-By-Layer Microcapsules Entrapping Glucose-Sensing Assay Components

After dissolving the calcium carbonate core, LbL microspheres, initially encapsulating 3 μM mPEG-ConA-TRITC and 400 nM APTS-MT, were imaged utilizing a confocal microscope (Leica TCS SP5, Leica Microsystems, Inc., Buffalo Grove, IL) using sequential scanning with excitation wavelengths of 476 nm and 543 nm and a 63x dry objective. As exhibited in **Figure 4.4.**, the fluorescence emission of APTS-MT (**Fig. 4.4.a**) and mPEG-ConA-TRITC (**Fig. 4.4.b**) were captured. The microspheres had an approximate diameter of 8~12 μm and conveyed that both assay components were successfully encapsulated. Since the microspheres range in size and reside in different x- ,y-, and z- positions, the confocal image captures various planes of individual spheres. Upon viewing various microsphere planes, mPEG-ConA-TRITC seems to inhabit the entire core. As a previous concern, the net negative charge of ConA would immobilize the protein to the innermost positive layer of the assembly and thereby reduce its ability to reversibly bind with a competing ligand. However, as seen in Figure 4.4., mPEG-ConA-TRITC appears to dwell throughout the microsphere core. This may suggest that the neutral PEG chains conjugated to the ConA's surface are masking the protein's negative charges and thus keeping the protein freely suspended.

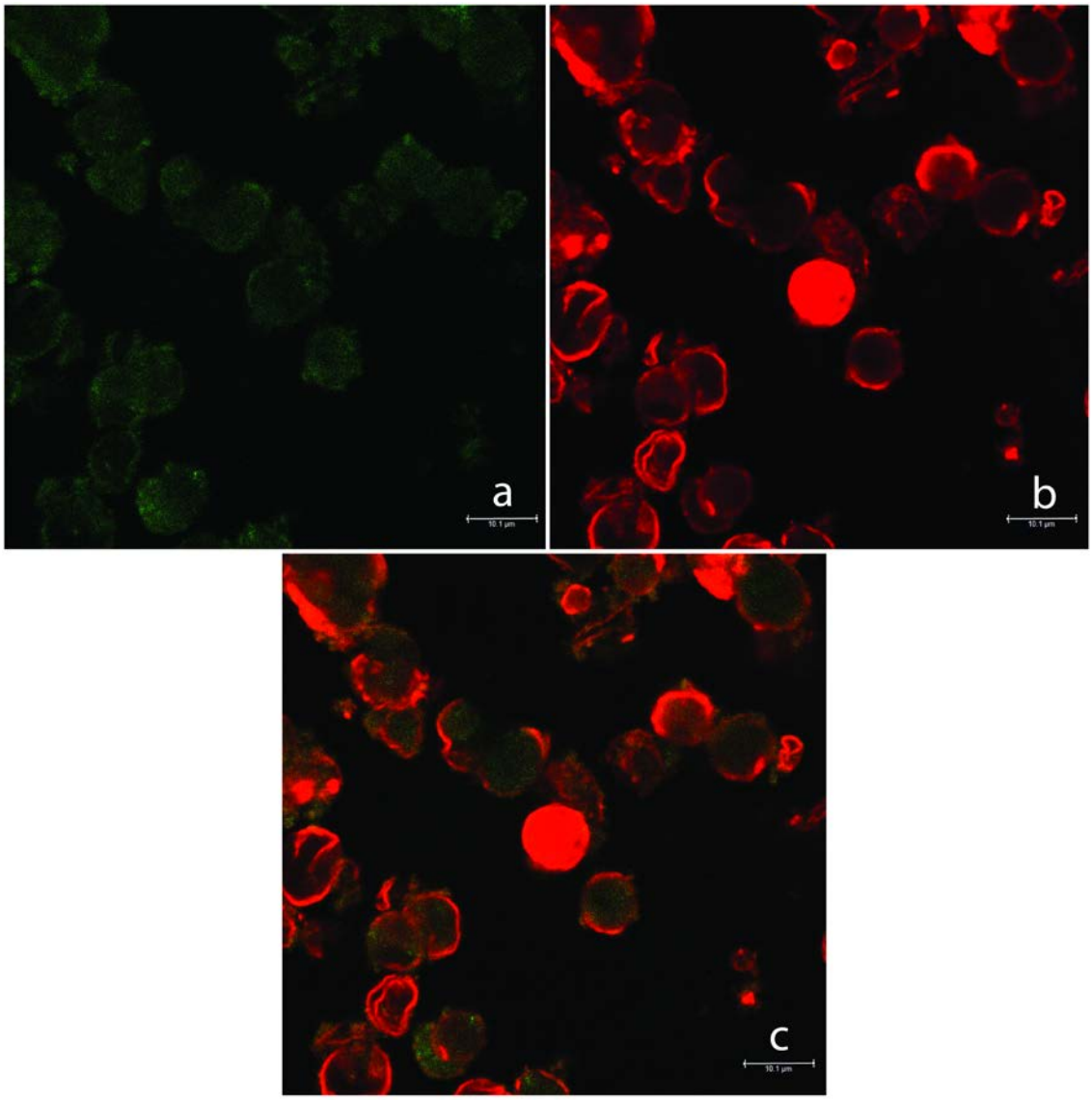

Figure 4.4. | Confocal microscopy: LbL microspheres encapsulating glucose-sensing assay components. Confocal microscopy images of LbL microspheres post calcium carbonate core dissolution. The microspheres display the fluorescence emission of encapsulated **(a)** APTS-MT and **(b)** mPEG-ConA-TRITC. **c,** An overlay of images **a** and **b**. Scale bars are 10.1 μm.

4.4.5. Thermoresponsive Hydrogel for Microsphere Embedding

As a proof of concept in the progression of a biocompatible membrane that contains a glucose sensing assay, the core-dissolved LbL microspheres (initially holding 3 μM mPEG-ConA-TRITC and 400 nM APTS-MT) were embedded within a SNNC hydrogel matrix. The resulting polymer was then imaged utilizing a confocal microscope (Leica TCS SP5, Leica Microsystems, Inc., Buffalo Grove, IL) using sequential scanning with excitation wavelengths of 476 nm and 543 nm and a 40x dry objective. The densely packed matrix shows microspheres inlayed within the SNNC hydrogel (**Fig. 4.5.**). Interestingly, the fluorescence emission from APTS-MT (**Fig. 4.5.**a) was more intense in comparison to the microspheres in free solution. This could suggest that the SNNC hydrogel may aid in the containing the low molecular weight of APTS-MT should it be slowly leaching from the microsphere hollow cavities.

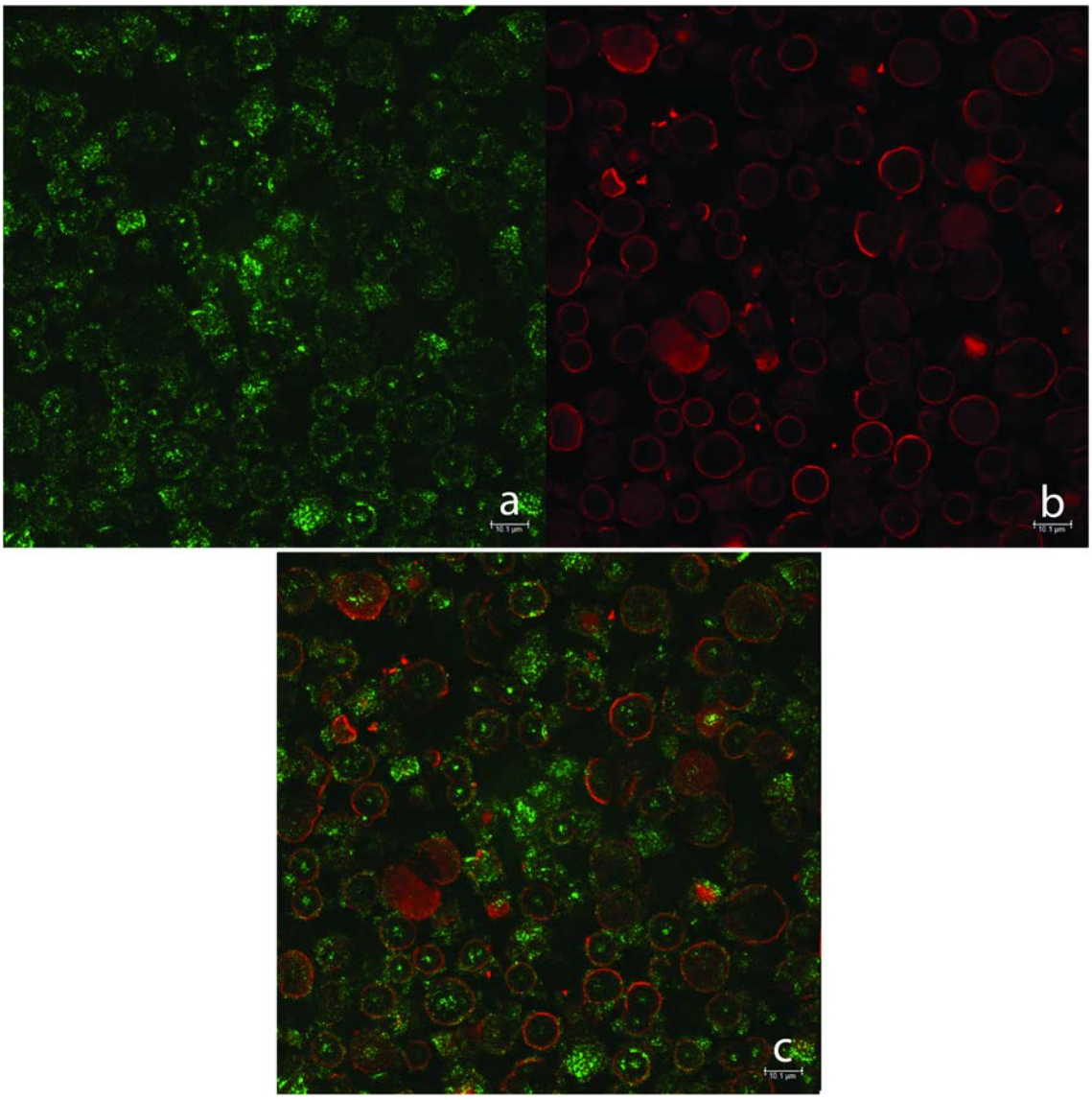

Figure 4.5. | Confocal microscopy: SNNC embedded with LbL microspheres. Confocal microscopy images of core-dissolved LbL microspheres (encapsulating **(a)** APTS-MT and **(b)** mPEG-ConA-TRITC) that are embedded within a SNNC hydrogel matrix. **c,** An overlay of images **a** and **b**. Scale bars are 10.1 μm.

4.4.6. FRET Responses

To function in a competitive binding, glucose sensing assay, mPEG-ConA-TRITC requires a suitable fluorescent pair, APTS-MT, to produce a FRET response. Therefore, mPEG-ConA-TRITC (FRET acceptor) was placed in solution with APTS-MT (FRET donor) at a concentration of 3 μM to 100 nM, respectively. At tiered glucose concentrations (0, 200, and 400 mg dL^{-1}), the fluorescence intensity of the FRET donor was measured (**Fig. 4.6.**). As the glucose concentration was increased in the system, the FRET donor emission also increased. The relation indicates that in the company of glucose, glucose actively binds to mPEG-ConA-TRITC and causes the disassociation of APTS-MT beyond the Förster distance. Thus, the FRET efficiency decreases, which results in an increase in the donor fluorescence emission intensity. The second peak (~580 nm) is believed to be a product of the spectra overlap between the donor and acceptor fluorophores.

Now, the FRET response of the LbL assembled, microsphere encapsulated assay (initially 3 μM mPEG-ConA-TRITC and 400 nM APTS-MT) was also measured at discrete glucose levels (0, 100, 200, 400, and 600 mg dL^{-1}) (**Fig. 4.7.**). These spectra were collected after the LbL microspheres were allowed to soak in the corresponding glucose concentrated solution for 5h. This should have provided adequate time for the glucose to diffuse through the 15 bilayers and cause the disassociation of APTS-MT. However, in contrast to the FRET response in free solution and shown in Figure 4.7. as the glucose concentration increases in the system, the acceptor emission appears to change. This could be misinterpreted as a FRET response since the affiliation implies

that in presence of glucose, mPEG-ConA-TRITC binds to glucose, pushes APTS-MT farther than the Förster distance in which APTS-MT thereby does not transfer energy, and the fluorescence intensity of mPEG-ConA-TRITC declines. However, since the definitive FRET response in free solution demonstrated a change in the donor emission, the acceptor emission change witnessed here is more likely due to a dilution effect. In order to vary the glucose concentrations while maintaining a similar population of microspheres in each microplate well, small highly concentrated aliquots were introduced which increased the sample volumes. Essentially, this diluted the microsphere concentration.

The lack of a FRET response could be a result of an insufficient amount of or an incorrect ratio of mPEG-ConA-TRITC and APTS-MT. It is plausible that during fabrication the retention rate of one or both assay components within the calcium carbonate microspheres is low. Further, if retention is sufficient and the ratio is incorrect, it could indicate that although the LbL assembly is providing resistance, APTS-MT is still slowly leaching out of the hollow microsphere core. Yet another theory points to the use of EDTA to dissolve the calcium carbonate core. EDTA may also interfere with the calcium ions required in ConA to bind with carbohydrates. Although the microspheres are soaked in a calcium rich TRIS solution, it is possible that EDTA may slight alter the protein's structure resulting in its inability to bind with APTS-MT. Regardless, witnessing both the donor and acceptor emission peaks further proves that mPEG-ConA-TRITC and APTS-MT are present within the microspheres and that the LbL assembly appears to be entrapping both components.

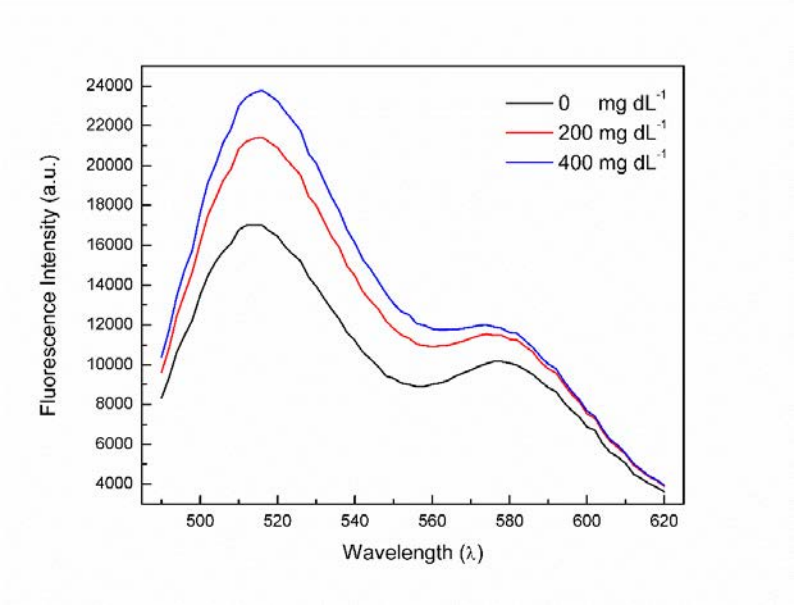

Figure 4.6. | Assay FRET response in free solution. The assay FRET donor response in the presence of various glucose concentrations.

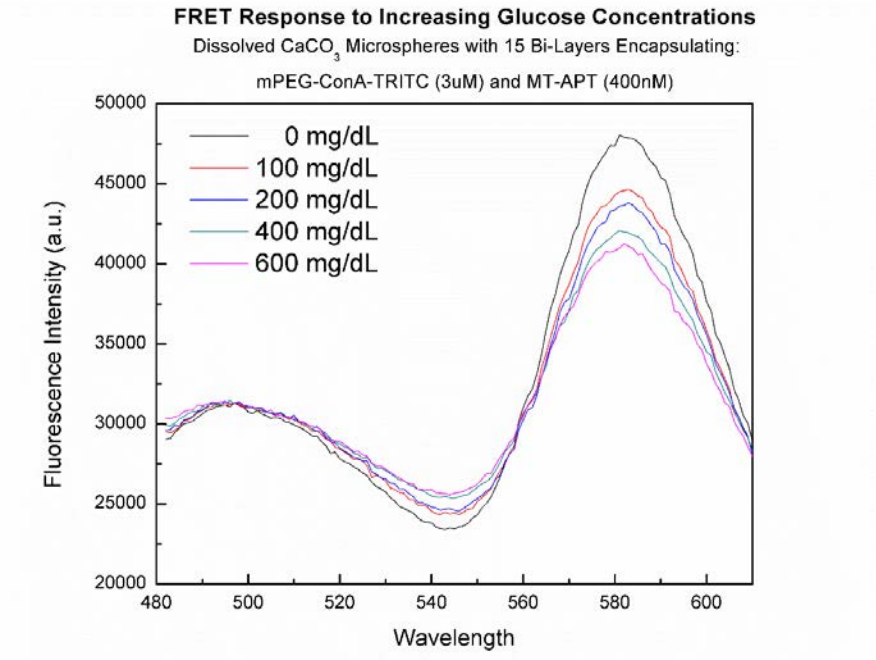

Figure 4.7. | Donor and acceptor emission spectra within LbL microspheres. The donor and acceptor emission spectra from the calcium carbonate core-dissolved LbL microsphere encapsulated FRET pair.

4.5. Summary

PEGylated ConA was evaluated and compared to native ConA for use within a competitive binding, glucose-sensing assay. ConA was successfully grafted with mPEG (5 kDa) chains, and the degree of PEGylation was determined utilizing fluorescamine. The decrease in the fluorescamine fluorescence intensity of mPEG-ConA indicated an increase in PEGylation, as fewer primary amines were available. It was determined that approximately 3~4 chains resided on the surface of a ConA monomer.

To investigate the ligand binding affinity between PEGylated and native ConA, the associating and disassociating constants were measured using fluorescence anisotropy. The calculated affinities indicated that PEGylated and native ConA were similar and thus, it could be assumed that the mobile, conjugated PEG chains were not interfering with ConA's ligand binding site.

mPEG-ConA was then assessed for its resistance to non-specific electrostatic interactions. In comparison to native ConA, mPEG-ConA exhibited the ability to prevent electrostatic, non-specific binding when exposed to charged LbL assembly surfaces. This suggested that the mobile PEG chains masked the protein's net negative charge, and therefore, enabled ConA to remain suspended in free solution. As such, it conveys promise to resist the associated charges within a LbL assembled delivery system.

The successful encapsulation of mPEG-ConA-TRITC and APTS-MT within a LbL assembled, calcium carbonate core-dissolved microsphere with 15 bilayers was demonstrated through confocal images and observing both donor and acceptor emission

peaks. Further, mPEG-ConA-TRITC appeared to maintain homogenous suspension within the LbL microsphere core – resisting the electrostatic charges of the LbL assembly. In addition, it exhibited the LbL assembly's ability to encapsulate both assay components, but especially the low molecular weight of APTS-MT.

Although a definitive FRET response was witnessed with increasing glucose concentrations between mPEG-ConA-TRITC and APTS-MT in free solution, when encapsulated, a misleading FRET response was seen that is likely associated with a dilution effect. Nonetheless, the assay's components were confirmed present within the microsphere cavities, and as a proof of concept, these microspheres were successfully inlayed into a SNNC matrix. Future studies should be completed that consider optimizing the concentration and encapsulating rate of higher molecular weight FRET-pairs to enhance the FRET response within these LbL microspheres and when the spheres are embedded within a thermoresponsive, biocompatible hydrogel.

CHAPTER V

CONCLUSIONS

Diabetes mellitus is a chronic and potentially attenuating disease that results in uncontrolled glycemic concentrations and an elevated risk for long-term secondary complications. To-date, the “finger-prick” is the most common and widely used technique to monitor blood glucose concentration. Unfortunately, it only provides a glance of an ever-changing concentration. Commercial CGM systems have potential, but their transcutaneous, amperometric sensors facilitate a heightened FBR, which limits their lifetimes to an FDA-approved maximum of 7 days. Herein, a “self-cleaning”, thermoresponsive, DNNC hydrogel was evaluated and used as an anti-biofouling membrane to contain LbL microsphere assemblies encapsulating a competitive binding FRET assay composed of mPEG-ConA-TRITC and APTS-MT. This research showed the effectiveness of thermoresponsive DNNC hydrogels to resist biofouling and demonstrated the potential of thermoresponsive hydrogels, when combined with an encapsulated glucose assay, as an implantable continuous glucose monitoring biosensor.

In Chapter II, a “self-cleaning,” thermoresponsive, DNNC hydrogel was developed that modulates its surface hydrophobicity with temperature. The original PNIPAAm hydrogel was designed as a single network (SN). However, to improve its mechanical robustness and swelling capabilities, a double network version was formulated. The improved DNNC hydrogel composition presented glucose diffusion coefficients similar to cutaneous tissue near subcutaneous physiological temperatures, a stable forward and reverse thermosensitivity profile, and cellular release abilities *in vitro*

without toxic, cell-damaging effects. Overall, the new DNNC hydrogel exhibited promising *in vitro* anti-biofouling characteristics and glucose biosensor properties.

In Chapter III, the DNNC hydrogel was assessed *in vivo* for 30 days. Using PEG-DA as a well-established, U.S. F.D.A. approved, biocompatible control, DNNC and PEG-DA hydrogels were subcutaneously implanted on the dorsal of CD® Hairless rats. Excised and assessed post 7 and 30 days, a significant decrease in fibrous capsule formation and increase in neovascular growth was observed around the DNNC hydrogel in comparison to PEG-DA at 30 days. Furthermore, a model of metabolic and environment temperatures conveyed a potential fluctuation range that appeared sufficient to drive the DNNC hydrogel's "self-cleaning" property. Essentially, these results are ideal for a biosensor membrane in order to decrease sensor lag time and improve its accuracy over the extent of its lifespan without the use of an external heat source.

In Chapter IV, a competitive binding, FRET assay was encapsulated within calcium carbonate core-dissolved LbL assembled microspheres. To improve the stability of the carbohydrate-binding protein, ConA, and increase its resistance to electrostatic surfaces without sacrificing its ligand bind affinity, PEG chains were covalently conjugated to the protein's surface through a process known as PEGylation. mPEG-ConA-TRITC and APTS-MT were successfully encapsulated within LBL microsphere assemblies with a dissolved calcium carbonate core, which were also successfully embedded within a SNNC hydrogel. Although the encapsulated assay lacked a definitive FRET response to varying glucose concentrations, confocal microscopy confirmed the assay's homogenous encapsulation feasibility – conveying this FRET-based glucose-

sensing assay and its delivery systems as a promising approach for a continuous glucose monitor.

CHAPTER VI

FUTURE DIRECTIONS

6.1. Implantable Membrane Geometry

The delayed glucose biosensor response results due to a combination of diffusion and assay reaction time lags. It is essential to minimize these parameters to obtain a sensible response time (3-5 min). Therefore, future studies will consider alternative DNNC geometries for the containment of the glucose-sensing LbL microspheres.

As needle-injection simplifies subcutaneous implantation, a hollow cylindrical geometry will be constructed, whose cavity will be injected with glucose-sensing microspheres. A glucose diffusion time lag model was simulated that effectively helps determine the DNNC hydrogel's optimal cylindrical dimensions. Incorporating the glucose diffusion rate ($1.88 \pm 0.01 \times 10^{-6}$ cm^2 s^{-1}, see Chapter II), the maximum and minimum free tetrahedral mesh element size of 0.382 mm and 0.0249 mm, respectively, cylinder end cap thicknesses of 300 μm, and varying the membrane wall thickness, the hollow cavity radius, and the membrane length, the glucose diffusion time lag will be modeled. Based on the following simplified equation that relates the cylinder's surface area to hollow cavity volume:

$$\frac{Surface\ Area}{Volume} = \frac{2(r_1 + L_1)}{r_2^2 L_2}$$

where r_1 is the cylinder outer radius, r_2 is the hollow cavity radius, L_1 is the cylinder outer length, and L_2 is the hollow cavity length, it is expected to result in a decreased surface area to volume ratio as the radii and lengths are increased (**Fig. 6.1.**). Future studies will consider the required mechanical robustness for subcutaneous implantation and necessary glucose-sensing microsphere volume when deciding on a final geometric design.

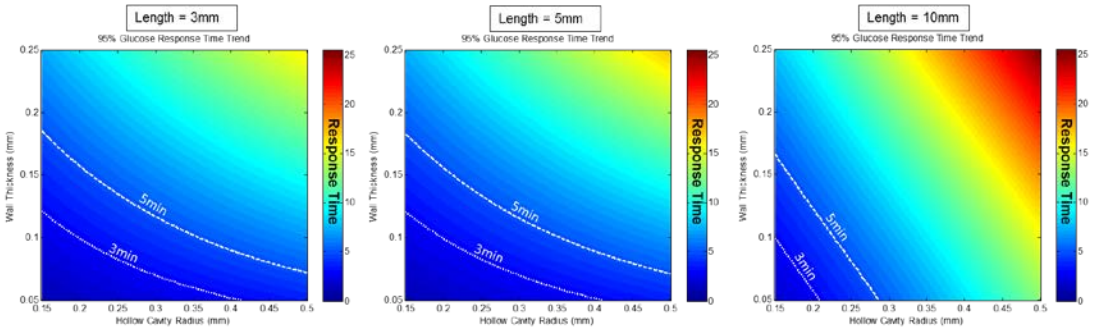

Figure 6.1. | Hollow Cylindrical Glucose Diffusion Model. Glucose diffusion model conveying the necessary cylindrical dimensions to obtain 3 and 5 min lag times.

6.2. Extended *In Vivo* Biocompatibility Evaluation

The human body's immune system is an amazing and intricate organization that provides the best available comprehensive protection. Its synergistic, yet complex, pathways fight the introduction of most foreign elements – even those with physiological benefits (i.e. implantable continuous glucose monitoring biosensor). Future studies will evaluate the DNNC hydrogel's efficacy to minimize biofouling for at least 90 days. This

time point marks the full length of the healing process, and thereby provides greater insight to the extent of the DNNC hydrogel's anti-biofouling property. Furthermore, a DNNC hydrogel containing glucose-sensing LbL microspheres will be evaluated in vivo for at least 90 days to confirm its effectiveness in reducing fibrous encapsulation although the hydrogel's composition has been slightly altered.

REFERENCES

1. Devlin TM. *Textbook of Biochemistry with Clinical Correlations*. Wiley-Liss: N.Y., 2006.

2. Tuchin VV. *Handbook of Optical Sensing of Glucose in Biological Fluids and Tissues*. CRC Press: Boca Raton, 2009.

3. Srikanta S, Ricker AT, McCulloch DK, Soeldner JS, Eisenbarth GS, Palmer JP. Autoimmunity to insulin, beta cell dysfunction, and development of insulin-dependent diabetes mellitus. *Diabetes* 1986, **35**(2)**:** 139-142.

4. Ahmed AM. History of diabetes mellitus. *Saudi Medical Journal* 2002, **23**(4)**:** 373-378.

5. Cunningham DD, Stenken JA. *In Vivo Glucose Sensing*, vol. 174. John Wiley & Sons, Inc.: Hoboken, N. J., 2010.

6. Prevention CfDCa. National Diabetes Statistics Report. 2014 [cited 2014 July 9]Available from: http://www.cdc.gov/diabetes/pubs/statsreport14/national-diabetes-report-web.pdf

7. Aguiree F, Brown A, Cho NH, Dahlquist G, Dodd S, Dunning T, *et al.* IDF Diabetes Atlas. 2013.

8. Guariguata L, Whiting D, Hambleton I, Beagley J, Linnenkamp U, Shaw J. Global estimates of diabetes prevalence for 2013 and projections for 2035. *Diabetes Research and Clinical Practice* 2014, **103**(2)**:** 137-149.

9. United Nations General Assembly sS. UN Resolution 61/225: World Diabetes Day. Signed 20 December 2006.

10. Del Prato S. A call to action–the UN Resolution on diabetes. *International Journal of Clinical Practice* 2007, **61**(s157)**:** 1-4.

11. U.S. Department of Health and Human Services, Centers for Disease Control and Prevention. FastStats. Leading Causes of Death 2013. Available: http://www.cdc.gov/nchs/fastats/leading-causes-of-death.htm.

12. The Diabetes Control and Complications Trial Research Group. The effect of intensive treatment of diabetes on the development and progression of long-term complications in insulin-dependent diabetes mellitus. *New England Journal of Medicine* 1993, **329**(14)**:** 977-986.

13. Rossing P, de Zeeuw D. Need for better diabetes treatment for improved renal outcome. *Kidney International*, **79 Suppl 120:** S28-32.

14. Deckert T, Poulsen JE, Larsen M. Prognosis of diabetics with diabetes onset before the age of thirty-one. I. Survival, causes of death, and complications. *Diabetologia* 1978, **14**(6)**:** 363-370.

15. Newman JD, Turner AP. Home blood glucose biosensors: a commercial perspective. *Biosensors and Bioelectronics* 2005, **20**(12)**:** 2435-2453.

16. Chaubey A, Malhotra BD. Mediated biosensors. *Biosensors and Bioelectronics* 2002, **17**(6-7)**:** 441-456.

17. Wahowiak L. Blood Glucose Meters 2014 - Will meters be more accurate? And getting the most from what you have 2014 [cited 2014 September 27]Available from: http://www.diabetesforecast.org/2014/Jan/blood-glucose-meters-2014.html

18. Clark LC, Lyons C. Electrode systems for continuous monitoring in cardiovascular surgery. *Annals of the New York Academy of Sciences* 1962, **102**(1)**:** 29-45.

19. McGarraugh G. The chemistry of commercial continuous glucose monitors. *Diabetes Technology and Therapeutics* 2009, **11 Suppl 1:** S17-24.

20. Pickup J, Rolinski O, Birch D. In vivo glucose sensing for diabetes management: progress towards non-invasive monitoring. Interview by Judy Jones. *British Medical Journal* 1999, **319**(7220)**:** 1289.

21. Dungan K, Chapman J, Braithwaite SS, Buse J. Glucose measurement: confounding issues in setting targets for inpatient management. *Diabetes Care* 2007, **30**(2)**:** 403-409.

22. Skeie S, Thue G, Nerhus K, Sandberg S. Instruments for self-monitoring of blood glucose: comparisons of testing quality achieved by patients and a technician. *Clinical Chemistry* 2002, **48**(7)**:** 994-1003.

23. Association AD. Standards of medical care in diabetes—2014. *Diabetes Care* 2014, **37**(Supplement 1)**:** S14-S80.

24. Baumstark A, Schmid C, Pleus S, Rittmeyer D, Haug C, Freckmann G. Accuracy Assessment of an Advanced Blood Glucose Monitoring System for Self-Testing With Three Reagent System Lots Following ISO 15197: 2013. *Journal of Diabetes Science and Technology* 2014**:** 1932296814546529.

25. Link M, Pleus S, Schmid C, Freckmann G, Baumstark A, Stolberg E, *et al.* Accuracy Evaluation of Three Systems for Self-monitoring of Blood Glucose With Three Different Test Strip Lots Following ISO 15197. *Journal of Diabetes Science and Technology* 2014, **8**(2)**:** 422-424.

26. Mollema ED, Snoek FJ, Pouwer F, Heine RJ, van der Ploeg HM. Diabetes Fear of Injecting and Self-Testing Questionnaire: a psychometric evaluation. *Diabetes Care* 2000, **23**(6)**:** 765-769.

27. Maran A, Tschoepe D, Di Mauro M, Fisher WA, Loeffler K, Vesper I, *et al.* Use of an integrated strip-free blood glucose monitoring system increases frequency of self-monitoring and improves glycemic control: Results from the ExAct study. *Journal of Clinical & Translational Endocrinology* 2014.

28. Nyomba BLG, Berard L, Murphy L. The cost of self-monitoring of blood glucose is an important factor limiting glycemic control in diabetic patients. *Diabetes Care* 2002, **25**(7)**:** 1244-1245.

29. Cheyne E, Kerr D. Making 'sense' of diabetes: using a continuous glucose sensor in clinical practice. *Diabetes Metabolism Research and Reviews* 2002, **18:** S43-S48.

30. Raccah D, Sulmont V, Reznik Y, Guerci B, Renard E, Hanaire H, *et al.* Incremental Value of Continuous Glucose Monitoring When Starting Pump Therapy in Patients With Poorly Controlled Type 1 Diabetes The RealTrend study. *Diabetes Care* 2009, **32**(12)**:** 2245-2250.

31. Bode BW, Schwartz S, Stubbs HA, Block JE. Glycemic characteristics in continuously monitored patients with type 1 and type 2 diabetes. *Diabetes Care* 2005, **28**(10)**:** 2361-2366.

32. Garg SK, Schwartz S, Edelman SV. Improved glucose excursions using an implantable real-time continuous glucose sensor in adults with type 1 diabetes. *Diabetes Care* 2004, **27**(3)**:** 734-738.

33. Koschinsky T, Heinemann L. Sensors for glucose monitoring: technical and clinical aspects. *Diabetes Metabolism Research and Reviews* 2001, **17**(2)**:** 113-123.

34. Brewer KW, Chase HP, Owen S, Garg SK. Slicing the pie. Correlating HbA-- values with average blood glucose values in a pie chart form. *Diabetes Care* 1998, **21**(2)**:** 209-212.

35. Bunn HF, Haney DN, Kamin S, Gabbay KH, Gallop PM. The biosynthesis of human hemoglobin A1c. Slow glycosylation of hemoglobin in vivo. *Journal of Clinical Investigation* 1976, **57**(6)**:** 1652-1659.

36. Center MDRaT. Hemoglobin A1c Fact Sheet. [cited 2011 November 4]Available from: http://www.med.umich.edu/mdrtc/cores/ChemCore/hemoa1c.htm

37. Garg SK, Campbell RK, Delahanty L, Halvorson M. The role of frequent glucose monitoring in intensive diabetes management. *Diabetes Education* 2000**:** 1-17.

38. Mastrototaro J, Shin J, Marcus A, Sulur G. The accuracy and efficacy of real-time continuous glucose monitoring sensor in patients with type 1 diabetes. *Diabetes Technology and Therapeutics* 2008, **10**(5)**:** 385-390.

39. Medtronic. The Guardian REAL-Time Continuous Glucose Monitoring System. [cited 2011 November 5]Available from: http://www.medtronicdiabetes.net/Products/guardiancgm

40. Care AD. Updated Important Note - FreeStyle Navigator Continuous Glucose Monitoring System U.S. Customers. 2011 [cited 2013 January 06]Available from: https://www.abbottdiabetescare.com/press-room/2011/2011-a.html

41. Switzer SM, Emily G, Moser B, Rockler BE. Intensive Insulin Therapy in Patients with Type 1 Diabetes Mellitus. *Insulin Therapy, An Issue of Endocrinology and Metabolism Clinics* 2012, **41**(1)**:** 5.

42. Weinstein RL, Bugler JR, Schwartz SL, Peyser TA, Brazg RL, McGarraugh GV. Accuracy of the 5-day freestyle navigator continuous glucose monitoring system - Comparison with frequent laboratory reference measurements. *Diabetes Care* 2007, **30**(5)**:** 1125-1130.

43. Henning T. Commercially Available Continuous Glucose Monitoring Systems. *In Vivo Glucose Sensing* 2002, **174:** 113-156.

44. Heinemann L, Koschinsky T. Continuous glucose monitoring: an overview of today's technologies and their clinical applications. *International Journal of Clinical Practice Supplement* 2002(129)**:** 75-79.

45. Wolpert HA. The Nuts and Bolts of Achieving End Points With Real-Time Continuous Glucose Monitoring. *Diabetes Care* 2008, **31:** S146-S149.

46. Dunn TC, Eastman RC, Tamada JA. Rates of glucose change measured by blood glucose meter and the GlucoWatch Biographer during day, night, and around mealtimes. *Diabetes Care* 2004, **27**(9)**:** 2161-2165.

47. Kulcu E, Tamada JA, Reach G, Potts RO, Lesho MJ. Physiological differences between interstitial glucose and blood glucose measured in human subjects. *Diabetes Care* 2003, **26**(8)**:** 2405-2409.

48. Cengiz E, Tamborlane WV. A Tale of Two Compartments: Interstitial Versus Blood Glucose Monitoring. *Diabetes Technology and Therapeutics* 2009, **11:** S11-S16.

49. Wernerman J, Desaive T, Finfer S, Foubert L, Furnary A, Holzinger U, *et al.* Continuous glucose control in the ICU: report of a 2013 round table meeting. *Critical Care* 2014, **18**(226)**:** 10.1186.

50. Office USPaT. Patent Full-Text and Image Database. [cited 2014 October 12]Available from: http://patft.uspto.gov/netacgi/nph-Parser?Sect1=PTO2&Sect2=HITOFF&u=%2Fnetahtml%2FPTO%2Fsearch-adv.htm&r=0&p=1&f=S&l=50&Query=%28noninvasive+or+non-invasive%29+OR+minimal+and+optic+and+glucose%0D%0A&d=PTXT

51. Oliver NS, Toumazou C, Cass AEG, Johnston DG. Glucose sensors: a review of current and emerging technology. *Diabetic Medicine* 2009, **26**(3)**:** 197-210.

52. Lakowicz JR. *Principles of fluorescence spectroscopy*. Springer: New York, 2006.

53. Meadows D, Schultz JS. Fiber-Optic Biosensors Based on Fluorescence Energy-Transfer. *Talanta* 1988, **35**(2)**:** 145-150.

54. Ballerstadt R, Schultz JS. Competitive-binding assay method based on fluorescence quenching of ligands held in close proximity by a multivalent receptor. *Analytica Chimica Acta* 1997, **345**(1-3)**:** 203-212.

55. Pickup JC, Hussain F, Evans ND, Rolinski OJ, Birch DJ. Fluorescence-based glucose sensors. *Biosensors and Bioelectronics* 2005, **20**(12)**:** 2555-2565.

56. Pickup J, McCartney L, Rolinski O, Birch D. In vivo glucose sensing for diabetes management: progress towards non-invasive monitoring. *British Medical Journal* 1999, **319**(7220)**:** 1289.

57. Abbas AK, Lichtman AH, Pillai S. *Cellular and Molecular Immunology*, 6th Edition edn. Saunders Elsevier: Philadelphia, PA, 2007.

58. Leffell MS, Donnenberg AD, Rose NR. *Handbook of Human Immunology*. CRC Press: New York, NY, 1997.

59. Lydyard P, Whelan A, Fanger MW. *Immunology*, Second Edition edn. Garland Science/BIOS Scientific Publishers Limited: New York, NY, 2004.

60. Black J. *Biological Performance of Materials: Fundamentals of Biocompatibility (Fourth Ed.)*. CRC Press: Taylor & Francis Group: Boca Raton, FL, 2006.

61. Frost M, Meyerhoff ME. In vivo chemical sensors: tackling biocompatibility. *Analytical Chemistry* 2006, **78**(21)**:** 7370-7377.

62. Raton B. *Implantation Biology the Host Response and Biomedical Devices (R.S. Greco, Ed.)*. CRC Press: London, 1994.

63. Quinn CA, Connor RE, Heller A. Biocompatible, glucose-permeable hydrogel for in situ coating of implantable biosensors. *Biomaterials* 1997, **18**(24)**:** 1665-1670.

64. Williams DF. *The Williams dictionary of biomaterials*. Liverpool University Press, 1999.

65. Ratner BD. Reducing capsular thickness and enhancing angiogenesis around implant drug release systems. *Journal of Controlled Release* 2002, **78**(1)**:** 211-218.

66. Moussy F, Reichert W. Biomaterials community examines biosensor biocompatibility. *Diabetes Technology and Therapeutics* 2000, **2**(3)**:** 473-477.

67. Dungel P, Long N, Yu B, Moussy Y, Moussy F. Study of the effects of tissue reactions on the function of implanted glucose sensors. *Journal of Biomedical Materials Research Part A* 2008, **85**(3)**:** 699-706.

68. Rebrin K, Fischer U, Hahn von Dorsche H, Von Woetke T, Abel P, Brunstein E. Subcutaneous glucose monitoring by means of electrochemical sensors: fiction or reality? *Journal of Biomedical Engineering* 1992, **14**(1)**:** 33-40.

69. Sharkawy AA, Klitzman B, Truskey GA, Reichert WM. Engineering the tissue which encapsulates subcutaneous implants. I. Diffusion properties. *Journal of Biomedical Material Research* 1997, **37**(3)**:** 401-412.

70. Wisniewski N, Rajamand N, Adamsson U, Lins PE, Reichert WM, Klitzman B, *et al.* Analyte flux through chronically implanted subcutaneous polyamide membranes differs in humans and rats. *American Journal of Physiology-Endocrinology Metabolism* 2002, **282**(6)**:** E1316-E1323.

71. Novak MT, Yuan F, Reichert WM. Modeling the relative impact of capsular tissue effects on implanted glucose sensor time lag and signal attenuation. *Analytical and Bioanalytical Chemistry* 2010, **398**(4)**:** 1695-1705.

72. Chang H-I, Wang Y. Cell responses to surface and architecture of tissue engineering scaffolds. *Regenerative Medicine and Tissue Engineering—Cells and Biomaterials, InTech: Rijeka, Croatia* 2011**:** 569-588.

73. O'Brien FJ, Harley B, Yannas IV, Gibson LJ. The effect of pore size on cell adhesion in collagen-GAG scaffolds. *Biomaterials* 2005, **26**(4)**:** 433-441.

74. Anderson JM. Biological responses to materials. *Annual Review of Materials Research* 2001, **31**(1)**:** 81-110.

75. Ratner BD, Bryant SJ. Biomaterials: where we have been and where we are going. *Annual Review of Biomedical Engineering* 2004, **6:** 41-75.

76. Morais JM, Papadimitrakopoulos F, Burgess DJ. Biomaterials/tissue interactions: possible solutions to overcome foreign body response. *Journal of American Association of Pharmaceutical Scientists* 2010, **12**(2)**:** 188-196.

77. Vroman L, Adams AL. Findings with the recording ellipsometer suggesting rapid exchange of specific plasma proteins at liquid/solid interfaces. *Surface Science* 1969, **16:** 438-446.

78. Vroman L, Adams AL, Klings M, Fischer GC, Munoz PC, Solensky RP. Reactions of Formed Elements of Blood with Plasma Proteins at Interfaces. *Annals of the New York Academy of Sciences* 1977, **283**(1)**:** 65-76.

79. Jung S-Y, Lim S-M, Albertorio F, Kim G, Gurau MC, Yang RD, *et al.* The Vroman effect: a molecular level description of fibrinogen displacement. *Journal of the American Chemical Society* 2003, **125**(42)**:** 12782-12786.

80. Ostuni E, Chapman RG, Holmlin RE, Takayama S, Whitesides GM. A survey of structure-property relationships of surfaces that resist the adsorption of protein. *Langmuir* 2001, **17**(18)**:** 5605-5620.

81. Thevenot P, Hu W, Tang L. Surface chemistry influence implant biocompatibility. *Current Topics in Medicinal Chemistry* 2008, **8**(4)**:** 270.

82. Israelachvili J, Wennerström H. Role of hydration and water structure in biological and colloidal interactions. 1996.

83. Noh H, Vogler EA. Volumetric interpretation of protein adsorption: mass and energy balance for albumin adsorption to particulate adsorbents with incrementally increasing hydrophilicity. *Biomaterials* 2006, **27**(34)**:** 5801-5812.

84. Xu L-C, Siedlecki CA. Effects of surface wettability and contact time on protein adhesion to biomaterial surfaces. *Biomaterials* 2007, **28**(22)**:** 3273-3283.

85. Tamada Y, Ikada Y. Effect of preadsorbed proteins on cell adhesion to polymer surfaces. *Journal of Colloid and Interface Science* 1993, **155**(2)**:** 334-339.

86. Goddard JM, Hotchkiss J. Polymer surface modification for the attachment of bioactive compounds. *Progress in Polymer Science* 2007, **32**(7)**:** 698-725.

87. Wei J, Igarashi T, Okumori N, Igarashi T, Maetani T, Liu B, *et al.* Influence of surface wettability on competitive protein adsorption and initial attachment of osteoblasts. *Biomedical Materials* 2009, **4**(4)**:** 045002.

88. Keselowsky BG, Collard DM, García AJ. Surface chemistry modulates focal adhesion composition and signaling through changes in integrin binding. *Biomaterials* 2004, **25**(28)**:** 5947-5954.

89. Tidwell CD, Ertel SI, Ratner BD, Tarasevich BJ, Atre S, Allara DL. Endothelial cell growth and protein adsorption on terminally functionalized, self-assembled monolayers of alkanethiolates on gold. *Langmuir* 1997, **13**(13)**:** 3404-3413.

90. Ohya Y, Matsunami H, Ouchi T. Cell growth on the porous sponges prepared from poly (depsipeptide-co-lactide) having various functional groups. *Journal of Biomaterials Science, Polymer Edition* 2004, **15**(1)**:** 111-123.

91. Jung H, Kwak B, Yang HS, Tae G, Kim J-S, Shin K. Attachment of cells to poly (styrene-co-acrylic acid) thin films with various charge densities. *Colloids and Surfaces A: Physicochemical and Engineering Aspects* 2008, **313:** 562-566.

92. Kim S, English AE, Kihm KD. Surface elasticity and charge concentration-dependent endothelial cell attachment to copolymer polyelectrolyte hydrogel. *Acta Biomaterialia* 2009, **5**(1)**:** 144-151.

93. Lestelius M, Liedberg B, Tengvall P. In vitro plasma protein adsorption on ω-functionalized alkanethiolate self-assembled monolayers. *Langmuir* 1997, **13**(22)**:** 5900-5908.

94. Kidoaki S, Matsuda T. Adhesion forces of the blood plasma proteins on self-assembled monolayer surfaces of alkanethiolates with different functional groups measured by an atomic force microscope. *Langmuir* 1999, **15**(22)**:** 7639-7646.

95. Altankov G, Richau K, Groth T. The role of surface zeta potential and substratum chemistry for regulation of dermal fibroblasts interaction. *Materialwissenschaft und Werkstofftechnik* 2003, **34**(12)**:** 1120-1128.

96. Faucheux N, Schweiss R, Lützow K, Werner C, Groth T. Self-assembled monolayers with different terminating groups as model substrates for cell adhesion studies. *Biomaterials* 2004, **25**(14)**:** 2721-2730.

97. Liu L, Chen S, Giachelli CM, Ratner BD, Jiang S. Controlling osteopontin orientation on surfaces to modulate endothelial cell adhesion. *Journal of Biomedical Materials Research Part A* 2005, **74**(1)**:** 23-31.

98. Blakney AK, Swartzlander MD, Bryant SJ. The effects of substrate stiffness on the in vitro activation of macrophages and in vivo host response to poly(ethylene glycol)-based hydrogels. *Journal of Biomedical Materials Research Part A* 2012, **100**(6)**:** 1375-1386.

99. Kim M-H, Kino-oka M, Kawase M, Yagi K, Taya M. Response of human epithelial cells to culture surfaces with varied roughnesses prepared by immobilizing dendrimers with/without D-glucose display. *Journal of Bioscience and Bioengineering* 2007, **103**(2)**:** 192-199.

100. Dalby MJ. Topographically induced direct cell mechanotransduction. *Medical Engineering & Physics* 2005, **27**(9)**:** 730-742.

101. Brauker JH, Carr-Brendel VE, Martinson LA, Crudele J, Johnston WD, Johnson RC. Neovascularization of synthetic membranes directed by membrane microarchitecture. *Journal of Biomedical Materials Research* 1995, **29**(12)**:** 1517-1524.

102. Sharkawy AA, Klitzman B, Truskey GA, Reichert WM. Engineering the tissue which encapsulates subcutaneous implants. II. Plasma–tissue exchange properties. *Journal of Biomedical Materials Research* 1998, **40**(4)**:** 586-597.

103. Sharkawy AA, Klitzman B, Truskey GA, Reichert WM. Engineering the tissue which encapsulates subcutaneous implants. III. Effective tissue response times. *Journal of Biomedical Materials Research* 1998, **40**(4)**:** 598-605.

104. Clowes AW, Kirkman TR, Reidy MA. Mechanisms of arterial graft healing. Rapid transmural capillary ingrowth provides a source of intimal endothelium and smooth muscle in porous PTFE prostheses. *American Journal of Pathology* 1986, **123**(2)**:** 220-230.

105. Clowes AW, Zacharias RK, Kirkman TR. Early endothelial coverage of synthetic arterial grafts: porosity revisited. *American Journal of Surgery* 1987, **153**(5)**:** 501-504.

106. Salzmann DL, Kleinert LB, Berman SS, Williams SK. The effects of porosity on endothelialization of ePTFE implanted in subcutaneous and adipose tissue. *Journal of Biomedical Materials Research* 1997, **34**(4)**:** 463-476.

107. Curran JM, Chen R, Hunt JA. The guidance of human mesenchymal stem cell differentiation in vitro by controlled modifications to the cell substrate. *Biomaterials* 2006, **27**(27)**:** 4783-4793.

108. Fujioka K, Maeda M, Hojo T, Sano A. Protein release from collagen matrices. *Advanced Drug Delivery Reviews* 1998, **31**(3)**:** 247-266.

109. Geiger M, Li R, Friess W. Collagen sponges for bone regeneration with rhBMP-2. *Advanced Drug Delivery Reviews* 2003, **55**(12)**:** 1613-1629.

110. de Vos P, Hoogmoed CG, Busscher HJ. Chemistry and biocompatibility of alginate-PLL capsules for immunoprotection of mammalian cells. *Journal of Biomedical Materials Research* 2002, **60**(2)**:** 252-259.

111. Draye J-P, Delaey B, Van de Voorde A, Van Den Bulcke A, De Reu B, Schacht E. In vitro and in vivo biocompatibility of dextran dialdehyde cross-linked gelatin hydrogel films. *Biomaterials* 1998, **19**(18)**:** 1677-1687.

112. Vercruysse KP, Prestwich GD. Hyaluronate derivatives in drug delivery. *Critical Reviews™ in Therapeutic Drug Carrier Systems* 1998, **15**(5).

113. Borchard G, Junginger H. Modern drug delivery applications of chitosan. *Advanced Drug Delivery Reviews* 2001, **52**(2)**:** 103-103.

114. Uchegby IF, Schatzlein AG, Tetley L, Gray AI, Sludden J, Siddique S, *et al.* Polymeric Chitosan-based Vesicles for Drug Delivery. *Journal of Pharmacy and Pharmacology* 1998, **50**(5)**:** 453-458.

115. Ward WK, Slobodzian EP, Tiekotter KL, Wood MD. The effect of microgeometry, implant thickness and polyurethane chemistry on the foreign body response to subcutaneous implants. *Biomaterials* 2002, **23**(21)**:** 4185-4192.

116. Anderson JM, Shive MS. Biodegradation and biocompatibility of PLA and PLGA microspheres. *Advanced Drug Delivery Reviews* 2012, **64:** 72-82.

117. Athanasiou KA, Niederauer GG, Agrawal C. Sterilization, toxicity, biocompatibility and clinical applications of polylactic acid/polyglycolic acid copolymers. *Biomaterials* 1996, **17**(2)**:** 93-102.

118. Lynn AD, Kyriakides TR, Bryant SJ. Characterization of the in vitro macrophage response and in vivo host response to poly(ethylene glycol)-based hydrogels. *Journal of Biomedical Materials Research Part A* 2010, **93**(3)**:** 941-953.

119. Crooks CA, Douglas JA, Broughton RL, Sefton MV. Microencapsulation of mammalian cells in a HEMA-MMA copolymer: effects on capsule morphology and permeability. *Journal of Biomedical Materials Research* 1990, **24**(9)**:** 1241-1262.

120. Mokry J, Karbanova J, Lukas J, Paleckova V, Dvorankova B. Biocompatibility of HEMA copolymers designed for treatment of CNS diseases with polymer-encapsulated cells. *Biotechnology Progress* 2000, **16**(5)**:** 897-904.

121. Bota PC, Collie AM, Puolakkainen P, Vernon RB, Sage EH, Ratner BD, *et al.* Biomaterial topography alters healing in vivo and monocyte/macrophage activation in vitro. *Journal of Biomedical Materials Research Part A* 2010, **95**(2)**:** 649-657.

122. Abraham AA, Fei R, Cote GL, Grunlan MA. Self-cleaning membrane to extend the lifetime of an implanted glucose biosensor. *ACS Applied Material Interfaces* 2013, **5**(24)**:** 12832-12838.

123. Fei R, George JT, Park J, Grunlan MA. Thermoresponsive nanocomposite double network hydrogels. *Soft Matter* 2011.

124. Gant RM, Hou Y, Grunlan MA, Cote GL. Development of a self-cleaning sensor membrane for implantable biosensors. *Journal of Biomedical Materials Research Part A* 2008.

125. Hou Y, Matthews AR, Smitherman AM, Bulick AS, Hahn MS, Hou H, *et al.* Thermoresponsive nanocomposite hydrogels with cell-releasing behavior. *Biomaterials* 2008, **29**(22)**:** 3175-3184.

126. Laurencin C, Elgendy H. The biocompatibility and toxicity of degradable polymeric materials: implications for drug delivery. *Site Specific Drug Delivery New York: Wiley* 1994**:** 27-46.

127. Williams D. Tissue-biomaterial interactions. *Journal of Materials Science* 1987, **22**(10)**:** 3421-3445.

128. Murthy N, Campbell J, Fausto N, Hoffman AS, Stayton PS. Bioinspired pH-responsive polymers for the intracellular delivery of biomolecular drugs. *Bioconjugate Chemistry* 2003, **14**(2)**:** 412-419.

129. Kopeček J. Hydrogel biomaterials: a smart future? *Biomaterials* 2007, **28**(34)**:** 5185-5192.

130. Ottenbrite RM, Huang SJ, Park K. Hydrogels and biodegradable polymers for bioapplications. 1996.

131. Shimoboji T, Larenas E, Fowler T, Hoffman AS, Stayton PS. Temperature-induced switching of enzyme activity with smart polymer-enzyme conjugates. *Bioconjugate Chemistry* 2003, **14**(3)**:** 517-525.

132. Shimoboji T, Larenas E, Fowler T, Kulkarni S, Hoffman AS, Stayton PS. Photoresponsive polymer–enzyme switches. *Proceedings of the National Academy of Sciences* 2002, **99**(26)**:** 16592-16596.

133. Chilkoti A, Dreher MR, Meyer DE. Design of thermally responsive, recombinant polypeptide carriers for targeted drug delivery. *Advanced Drug Delivery Reviews* 2002, **54**(8)**:** 1093-1111.

134. Jeong B, Kim SW, Bae YH. Thermosensitive sol–gel reversible hydrogels. *Advanced Drug Delivery Reviews* 2002, **54**(1)**:** 37-51.

135. Kim B, La Flamme K, Peppas NA. Dynamic swelling behavior of pH-sensitive anionic hydrogels used for protein delivery. *Journal of Applied Polymer Science* 2003, **89**(6)**:** 1606-1613.

136. Wang Y, Papadimitrakopoulos F, Burgess DJ. Polymeric “smart” coatings to prevent foreign body response to implantable biosensors. *Journal of Controlled Release* 2013, **169**(3)**:** 341-347.

137. Perretti M, Ahluwalia A. The microcirculation and inflammation: site of action for glucocorticoids. *Microcirculation* 2000, **7**(3)**:** 147-161.

138. Patil SD, Papadmitrakopoulos F, Burgess DJ. Concurrent delivery of dexamethasone and VEGF for localized inflammation control and angiogenesis. *Journal of Controlled Release* 2007, **117**(1)**:** 68-79.

139. Zhang L, Cao Z, Bai T, Carr L, Ella-Menye J-R, Irvin C, *et al.* Zwitterionic hydrogels implanted in mice resist the foreign-body reaction. *Nature Biotechnology* 2013, **31**(6)**:** 553-556.

140. Freitag R. *Synthetic Polymers for Biotechnology and Medicine*. Eurekah: Austin, TX, 2003.

141. Kumar A, Srivastava A, Galaev IY, Mattiasson B. Smart polymers: Physical forms and bioengineering applications. *Progress in Polymer Science* 2007, **32**(10)**:** 1205-1237.

142. Takahashi H, Nakayama M, Itoga K, Yamato M, Okano T. Micropatterned thermoresponsive polymer brush surfaces for fabricating cell sheets with well-controlled orientational structures. *Biomacromolecules* 2011, **12**(5)**:** 1414-1418.

143. Yamato M, Akiyama Y, Kobayashi J, Yang J, Kikuchi A, Okano T. Temperature-responsive cell culture surfaces for regenerative medicine with cell sheet engineering. *Progress in Polymer Science* 2007, **32**(8-9)**:** 1123-1133.

144. Yang J, Yamato M, Nishida K, Ohki T, Kanzaki M, Sekine H, *et al.* Cell delivery in regenerative medicine: The cell sheet engineering approach. *Journal of Controlled Release* 2006, **116**(2)**:** 193-203.

145. Hirokawa Y, Tanaka T. VOLUME PHASE-TRANSITION IN A NON-IONIC GEL. *Aip Conference Proceedings* 1984(107)**:** 203-208.

146. Huffman AS, Afrassiabi A, Dong LC. Thermally reversible hydrogels: II. Delivery and selective removal of substances from aqueous solutions. *Journal of Controlled Release* 1986, **4**(3)**:** 213-222.

147. Erbil C, Aras S, Uyanik N. Investigation of the effect of type and concentration of ionizable comonomer on the collapse behavior of N-isopropylacrylamide copolymer gels in water. *Journal of Polymer Science Part a-Polymer Chemistry* 1999, **37**(12)**:** 1847-1855.

148. Feil H, Bae YH, Feijen J, Kim SW. Effect of Comonomer Hydrophilicity and Ionization on the Lower Critical Solution Temperature of N-Isopropylacrylamide Copolymers. *Macromolecules* 1993, **26**(10)**:** 2496-2500.

149. Gant RM, Abraham AA, Hou Y, Cummins BM, Grunlan MA, Cote GL. Design of a self-cleaning thermoresponsive nanocomposite hydrogel membrane for implantable biosensors. *Acta Biomaterial* 2010.

150. Frost M, Meyerhoff ME. *In vivo* chemical sensors: Tackling biocompatibility. *Analytical Chemistry* 2006, **78**(21)**:** 7370-7377.

151. Wisniewski N, Reichert M. Methods for reducing biosensor membrane biofouling. *Colloids Surface, B* 2000, **18**(3-4)**:** 197-219.

152. Marshall AJ, Ratner BD. Quantitative characterization of sphere-templated porous biomaterials. *American Institute of Chemical Engineers Journal* 2005, **51:** 1221-1232.

153. Bota PCS, Collie AMB, Puolakkainen P, Vernon RB, Sage EH, Ratner BD, *et al.* Biomaterial topography alters healing *in vivo* and monocyte/macrophage activation *in vitro*. *Journal of Biomedical Materials Research Part A* 2010, **95:** 649-657.

154. Brauker JH, Carr-Brendel VE, Martinson LA, Crudele J, Johnston WD, Johnson RC. Neovascularization of synthetic membranes directed by membrane architecture. *Journal of Biomedical Materials Research Part A* 1995, **29:** 1517-1524.

155. Okano T, Yamada N, Okuhara M, Sakai H, Sakurai Y. Mechanism of cell detachment from temperature-modulated, hydrophilic-hydrophobic polymer surfaces. *Biomaterials* 1995, **16**(4)**:** 297-303.

156. Kobayashi J, Okano T. Fabrication of a thermoresponsive cell culture dish: a key technology for cell sheet tissue engineering. *Science Technology Advanced Materials* 2010, **11**(1)**:** 014111.

157. Yang J, Yamato M, Nishida K, Ohki T, Kanzaki M, Sekine H, *et al.* Cell delivery in regenerative medicine: The cell sheet engineering approach. *Journal of Controlled Release* 2006, **116**(2)**:** 193-203.

158. Tang Z, Akiyama Y, Okano T. Temperature-Responsive Polymer Modified Surface for Cell Sheet Engineering. *Polymers* 2012, **4**(3)**:** 1478-1498.

159. Gant RM, Hou Y, Grunlan MA, Cote GL. Development of a self-cleaning sensor membrane for implantable biosensors. *Journal of Biomedical Materials Research Part A* 2009, **90**(3)**:** 695-701.

160. Haraguchi K, Li H-J. Mechanical properties and structure of polymer-clay nanocomposite gels with high clay content. *Macromolecules* 2006, **39:** 1898-1905.

161. Zhang X-Z, Xu X-D, Cheng S-X, Zhuo R-X. Strategies to improve the response rate of thermosensitive PNIPAAm hydrogels. *Soft Matter* 2008, **4:** 385-391.

162. Fei R, George JT, Park J, Grunlan MA. Thermoresponsive nanocomposite double network hydrogels. *Soft Matter* 2011, **8:** 481-487.

163. Montgomery LD, Williams BA. Effect of ambient temperature on the thermal profile of the human forearm, hand, and fingers. *Annals of Biomedical Engineering* 1976, **4**(3)**:** 209-219.

164. Werner J, Buse M. Temperature profiles with respect to inhomogeneity and geometry of the human body. *Jounral of Appled Physiology* 1988, **65**(3)**:** 1110-1118.

165. Erbil C, Aras S, Uyanik N. Investigation of the effect of type and concentration of ionizable comonomer on the collapse behavior of *N*-isopropylacrylamide copolymer gels in water. *Journal of Polymer Science Part A: Polymer Chemistry* 1999, **37**(12)**:** 1847-1855.

166. Feil H, Bae YH, Feijen J, Kim SW. Effect of comonomer hydrophilicity and ionization on the lower critical solution temperatur of *N*-isopropylacrylamide copolymers. *Macromolecules* 1993, **26**(10)**:** 2496-2500.

167. Gant RM, Abraham AA, Hou Y, Cummins BM, Grunlan MA, Cote GL. Design of a self-cleaning thermoresponsive nanocomposite hydrogel membrane for implantable biosensors. *Acta Biomaterial* 2010**:** 2903-2910.

168. Wu C, Zhou S. Volume phase transition of swollen gels: Discontinuous or continuous? *Macromolecules* 1997, **30:** 574-576.

169. Bao L-R, Cheng X, Huang XD, Guo LJ, Pang SW, Yee AF. Nanoimprinting over topography and multilayer three-dimensional printing. *Journal of Vaccum Science and Technology B* 2002, **20**(6)**:** 2881-2886.

170. Hannoun BJ, Stephanopoulos G. Diffusion coefficients of glucose and ethanol in cell-free and cell-occupied calcium alginate membranes. *Biotechnology and Bioengineering* 1986, **28**(6)**:** 829-835.

171. Teixeira JA, Mota M, Ven,ncio A. Model identification and diffusion coefficients determination of glucose and malic acid in calcium alginate membranes. *Chemical Engineering Journal* 1994, **56**(1)**:** B9-B14.

172. Venancio A, Teixeira JA. Characterization of sugar diffusion coefficients in alginate membranes. *Biotechnology Tech* 1997, **11**(3)**:** 183-185.

173. Zhang W, Furusaki S. On the evaluation of diffusivities in gels using the diffusion cell technique. *Biochemistry Engineering Journal* 2001, **9**(1)**:** 73-82.

174. Khalil E, Kretsos K, Kasting GB. Glucose partition coefficient and diffusivity in the lower skin layers. *Pharmaceutical Research* 2006, **23**(6)**:** 1227-1234.

175. Russell RJ, Axel AC, Shields KL, Pishko MV. Mass transfer in rapidly photopolymerized poly(ethylene glycol) hydrogels used for chemical sensing. *Polymer* 2001, **42**(11)**:** 4893-4901.

176. Quinn CP, Pishko MV, Schmidtke DW, Ishikawa M, Wagner JG, Raskin P, *et al.* Kinetics of glucose delivery to subcutaneous tissue in rats measured with 0.3-mm amperometric microsensors. *The American Journal of Physiology* 1995, **269**(1 Pt 1)**:** E155-161.

177. Aussedat B, Dupire-Angel M, Gifford R, Klein JC, Wilson GS, Reach G. Interstitial glucose concentration and glycemia: implications for continuous subcutaneous glucose monitoring. *The American Journal of Physiology* 2000, **278**(4)**:** E716-728.

178. Baker DA, Gough DA. Dynamic delay and maximal dynamic error in continuous biosensors. *Analytical Chemistry* 1996, **68**(8)**:** 1292-1297.

179. Heise T, Koschinsky T, Heinemann L, Lodwig V. Hypoglycemia warning signal and glucose sensors: requirements and concepts. *Diabetes Technology and Therapeutics* 2003, **5**(4)**:** 563-571.

180. Rebrin K, Steil GM. Can interstitial glucose assessment replace blood glucose measurements? *Diabetes Technology and Therapeutics* 2000, **2**(3)**:** 461-472.

181. Rebrin K, Steil GM, van Antwerp WP, Mastrototaro JJ. Subcutaneous glucose predicts plasma glucose independent of insulin: implications for continuous monitoring. *The American Journal of Physiology* 1999, **277**(3 Pt 1)**:** E561-571.

182. Renner K, Amberger A, Konwalinka G, Kofler R, Gnaiger E. Changes of mitochondrial respiration, mitochondrial content and cell size after induction of apoptosis in leukemia cells. *Biochemistry and Biophysics Acta, Molecular Cell Research* 2003, **1642**(1)**:** 115-123.

183. Grinnell F, Feld MK. Fibronectin adsorption on hydrophilic and hydrophobic surfaces detected by antibody binding and analyzed during cell adhesion in serum-containing medium. *Journal of Biological Chemistry* 1982, **257**(9)**:** 4888-4893.

184. Gombotz WR, Guanghui W, Hoffman AS. Protein adsorption to poly(ethylene oxide) surfaces. *Journal of Biomedical Materials Research* 1991, **25:** 1547-1562.

185. Jeon SI, Andrade JD. Protein-surface interactions in the presence of polyethylene oxide. *Journal of Colloid Interface Science* 1991, **142:** 159-166.

186. Patenaude M, Hoare T. Injectable, mixed natural-synthetic polymer hydrogels with modular properties. *Biomacromolecules* 2012, **13**(2)**:** 369-378.

187. Klouda L, Mikos AG. Thermoresponsive hydrogels in biomedical applications. *European Journal of Pharmaceutical Biopharmacy* 2008, **68**(1)**:** 34-45.

188. Sin ML, Mach KE, Wong PK, Liao JC. Advances and challenges in biosensor-based diagnosis of infectious diseases. *Expert Review of Molecular Diagnostics* 2014, **14**(2)**:** 225-244.

189. Prevel C, Pellerano M, Van TN, Morris MC. Fluorescent biosensors for high throughput screening of protein kinase inhibitors. *Biotechnology Journal* 2014, **9**(2)**:** 253-265.

190. Mazzei F, Antiochia R, Botre F, Favero G, Tortolini C. Affinity-based biosensors in sport medicine and doping control analysis. *Bioanalysis* 2014, **6**(2)**:** 225-245.

191. Hamers D, van Voorst Vader L, Borst JW, Goedhart J. Development of FRET biosensors for mammalian and plant systems. *Protoplasma* 2014, **251**(2)**:** 333-347.

192. Abe K, Yoshida W, Ikebukuro K. Electrochemical biosensors using aptamers for theranostics. *Advanced Biochemistry Engineering and Biotechnology* 2014, **140:** 183-202.

193. Rippel RA, Ghanbari H, Seifalian AM. Tissue-engineered heart valve: future of cardiac surgery. *World Journal of Surgery* 2012, **36**(7)**:** 1581-1591.

194. Sawa Y, Tatsumi E, Tsukiya T, Matsuda K, Fukunaga K, Kishida A, *et al.* Journal of Artificial Organs 2013: the year in review : Journal of Artificial Organs Editorial Committee. *Journal of Artificial Organs : The Official Journal of the Japanese Society for Artificial Organs* 2014.

195. Salvatori M, Peloso A, Katari R, Orlando G. Regeneration and bioengineering of the kidney: current status and future challenges. *Current Urology Reports* 2014, **15**(1)**:** 379.

196. Malchesky PS. Artificial organ technologies around the world. *Artifical Organs* 2014, **38**(2)**:** 99-100.

197. Requicha JF, Viegas CA, Munoz F, Azevedo JT, Leonor IB, Reis RL, *et al.* A tissue engineering approach for periodontal regeneration based on a biodegradable double layer scaffold and adipose-derived stem cells. *Tissue Engineering Part A* 2014.

198. Moglia RS, Robinson JL, Muschenborn AD, Touchet TJ, Maitland DJ, Cosgriff-Hernandez E. Injectable PolyMIPE Scaffolds for Soft Tissue Regeneration. *Polymer (Guildf)* 2014, **56**(1)**:** 426-434.

199. Li X, Wang Y, Chen J, Wang Y, Ma J, Wu G. Controlled Release of Protein from Biodegradable Multi-sensitive Injectable Poly(ether-urethane) Hydrogel. *ACS Applied Material Interfaces* 2014.

200. Kim Y, Seol DR, Mohapatra S, Sunderland JJ, Schultz MK, Domann FE, *et al.* Locally Targeted Delivery of a Micron-Size Radiation Therapy Source Using Temperature-Sensitive Hydrogel. *International Journal of Radiation Oncology Biological Physics* 2014.

201. Dou QQ, Liow SS, Ye E, Lakshminarayanan R, Loh XJ. Biodegradable Thermogelling Polymers: Working Towards Clinical Applications. *Advanced Healthcare Materials* 2014.

202. Boopathy AV, Davis ME. Self-assembling Peptide-based delivery of therapeutics for myocardial infarction. *Methods of Molecular Biology* 2014, **1141:** 159-164.

203. Anderson JM, Rodriguez A, Chang DT. Foreign body reaction to biomaterials. *Semin Immunology* 2008, **20**(2)**:** 86-100.

204. Jung SY, Lim SM, Albertorio F, Kim G, Gurau MC, Yang RD, *et al.* The Vroman effect: a molecular level description of fibrinogen displacement. *Journal of American Chemistry Society* 2003, **125**(42)**:** 12782-12786.

205. Anderson JM. Inflammatory response to implants. *American Society for Artifical Internal Organs Transactions* 1988, **34**(2)**:** 101-107.

206. Woodward SC. How fibroblasts and giant cells encapsulate implants: considerations in design of glucose sensors. *Diabetes Care* 1982, **5**(3)**:** 278-281.

207. Mitchell RS, Kumar V, Abbas AK, Fausto N. Robbins Basic Pathology. *Philadelphia, PA: Saunders* 2007, **8:** 72-79.

208. Kovacs EJ. Fibrogenic cytokines: the role of immune mediators in the development of scar tissue. *Immunology Today* 1991, **12**(1)**:** 17-23.

209. Labat-Robert J, Bihari-Varga M, Robert L. Extracellular matrix. *Federation of European Biochemical Societies Letters* 1990, **268**(2)**:** 386-393.

210. Swartzlander MD, Lynn AD, Blakney AK, Kyriakides TR, Bryant SJ. Understanding the host response to cell-laden poly(ethylene glycol)-based hydrogels. *Biomaterials* 2013, **34**(4)**:** 952-964.

211. Gant RM, Hou Y, Grunlan MA, Cote GL. Development of a self-cleaning sensor membrane for implantable biosensors. *Journal of Biomedical Materials Research Part A* 2009, **90**(3)**:** 695-701.

212. Kobayashi J, Okano T. Fabrication of a thermoresponsive cell culture dish: a key technology for cell sheet tissue engineering. *Science and Technology of Advanced Materials* 2010, **11**(1)**:** 014111.

213. Ratner BD. Reducing capsular thickness and enhancing angiogenesis around implant drug release systems. *Journal of Controlled Release* 2002, **78**(1-3)**:** 211-218.

214. Sieminski AL, Gooch KJ. Biomaterial-microvasculature interactions. *Biomaterials* 2000, **21**(22)**:** 2232-2241.

215. Padera RF, Colton CK. Time course of membrane microarchitecture-driven neovascularization. *Biomaterials* 1996, **17**(3)**:** 277-284.

216. Jensen JA, Hunt TK, Scheuenstuhl H, Banda MJ. Effect of lactate, pyruvate, and pH on secretion of angiogenesis and mitogenesis factors by macrophages. *Laboratory Investigation* 1986, **54**(5)**:** 574-578.

217. Knighton DR, Fiegel VD. Macrophage-derived growth factors in wound healing: regulation of growth factor production by the oxygen microenvironment. *American Review of Respiratory Disease* 1989, **140**(4)**:** 1108-1111.

218. Knighton DR, Hunt TK, Scheuenstuhl H, Halliday BJ, Werb Z, Banda MJ. Oxygen tension regulates the expression of angiogenesis factor by macrophages. *Science* 1983, **221**(4617)**:** 1283-1285.

219. Polverini PJ, Cotran PS, Gimbrone MA, Jr., Unanue ER. Activated macrophages induce vascular proliferation. *Nature* 1977, **269**(5631)**:** 804-806.

220. Sunderkotter C, Goebeler M, Schulze-Osthoff K, Bhardwaj R, Sorg C. Macrophage-derived angiogenesis factors. *Pharmacology and Therapeautics* 1991, **51**(2)**:** 195-216.

221. Sunderkotter C, Steinbrink K, Goebeler M, Bhardwaj R, Sorg C. Macrophages and angiogenesis. *Journal of Leukocemia Biology* 1994, **55**(3)**:** 410-422.

222. Berse B, Brown LF, Van de Water L, Dvorak HF, Senger DR. Vascular permeability factor (vascular endothelial growth factor) gene is expressed differentially in normal tissues, macrophages, and tumors. *Molecular Biology of the Cell* 1992, **3**(2)**:** 211-220.

223. Shweiki D, Itin A, Soffer D, Keshet E. Vascular endothelial growth factor induced by hypoxia may mediate hypoxia-initiated angiogenesis. *Nature* 1992, **359**(6398)**:** 843-845.

224. Ghezzi P, Dinarello CA, Bianchi M, Rosandich ME, Repine JE, White CW. Hypoxia increases production of interleukin-1 and tumor necrosis factor by human mononuclear cells. *Cytokine* 1991, **3**(3)**:** 189-194.

225. Leibovich SJ, Polverini PJ, Shepard HM, Wiseman DM, Shively V, Nuseir N. Macrophage-induced angiogenesis is mediated by tumour necrosis factor-α. *Nature* 1987, **329**(6140)**:** 630-632.

226. Fan X, Nosov M, Carroll W, Gorelov A, Elvira C, Rochev Y. Macrophages behavior on different NIPAm-based thermoresponsive substrates. *Journal of Biomedical Materials Research Part A* 2013.

227. dos Reis IGM, de Araujo GG, Gobatto CA. Maximal lactate steady state in swimming rats by a body density-related method of workload quantification. *Comparative Exercise Physiology* 2010, **7**(04)**:** 179-184.

228. Gillooly JF, Brown JH, West GB, Savage VM, Charnov EL. Effects of size and temperature on metabolic rate. *Science* 2001, **293**(5538)**:** 2248-2251.

229. Meerlo P, De Boer SF, Koolhaas JM, Daan S, Van den Hoofdakker RH. Changes in daily rhythms of body temperature and activity after a single social defeat in rats. *Physiological Behaviors* 1996, **59**(4-5)**:** 735-739.

230. Refinetti R. Metabolic heat production, heat loss and the circadian rhythm of body temperature in the rat. *Experimental Physiology* 2003, **88**(3)**:** 423-429.

231. Gowrishankar TR, Stewart DA, Martin GT, Weaver JC. Transport lattice models of heat transport in skin with spatially heterogeneous, temperature-dependent perfusion. *Biomedical Engineering Online* 2004, **3**(1)**:** 42.

232. Torvi DA, Dale JD. A finite element model of skin subjected to a flash fire. *Journal of Biomechanical Engineering* 1994, **116**(3)**:** 250-255.

233. Cohen ML. Measurement of the thermal properties of human skin. A review. *Journal of Investigation Dermatology* 1977, **69**(3)**:** 333-338.

234. Grinberg VY, Dubovik AS, Kuznetsov DV, Grinberg NV, Grosberg AY, Tanaka T. Studies of the thermal volume transition of poly (N-isopropylacrylamide) hydrogels by high-sensitivity differential scanning microcalorimetry. 2. Thermodynamic functions. *Macromolecules* 2000, **33**(23)**:** 8685-8692.

235. Cummin BM, Lim J, Simanek EE, Pishko MV, Cote GL. Encapsulation of a Concanavalin A/dendrimer glucose sensing assay within microporated poly (ethylene glycol) microspheres. *Biomedical Optics Express* 2011, **2**(5)**:** 1243-1257.

236. Ibey BL, Beier HT, Rounds RM, Cote GL, Yadavalli VK, Pishko MV. Competitive binding assay for glucose based on glycodendrimer-fluorophore conjugates. *Analytical chemistry* 2005, **77**(21)**:** 7039-7046.

237. Russell RJ, Pishko MV, Gefrides CC, McShane MJ, Coté GL. A Fluorescence-Based Glucose Biosensor Using Concanavalin A and Dextran Encapsulated in a Poly(ethylene glycol) Hydrogel. *Analytical Chemistry* 1999, **71**(15)**:** 3126-3132.

238. Locke AK, Cummins BM, Abraham AA, Cote GL. PEGylation of Concanavalin A to improve its stability for an in vivo glucose sensing assay. *Analytical Chemistry* 2014.

239. Becker JW, Reeke G, Wang JL, Cunningham BA, Edelman GM. The covalent and three-dimensional structure of concanavalin A. III. Structure of the monomer and its interactions with metals and saccharides. *Journal of Biological Chemistry* 1975, **250**(4)**:** 1513-1524.

240. Hardman KD, Agarwal RC, Freiser MJ. Manganese and calcium binding sites of concanavalin A. *Journal of Molecular Biology* 1982, **157**(1)**:** 69-86.

241. Hardman KD, Ainsworth CF. Structure of concanavalin A at 2.4-Ang resolution. *Biochemistry* 1972, **11**(26)**:** 4910-4919.

242. Mandal D, Brewer C. Lectin-glycoconjugate cross-linking interactions. *Lectins and Glycobiology*. Springer, 1993, pp 117-128.

243. Cummins BM, Coté GL. A fluorescence polarization based assay for glucose sensing. 2012; 2012.

244. Cummins BM, Garza JT, Coté GL. Optimization of a Concanavalin A-Based Glucose Sensor Using Fluorescence Anisotropy. *Analytical Chemistry* 2013.

245. Cummins BM, Lim J, Simanek EE, Pishko MV, Coté GL. Understanding the mechanism and optimizing a competitive binding fluorescent glucose sensor. 2011; 2011.

246. Cummins BM, Lim J, Simanek EE, Pishko MV, Coté GL. Encapsulation of a concanavalin A/dendrimer glucose sensing assay within microporated poly (ethylene glycol) microspheres. *Biomedical Optics Express* 2011, **2**(5)**:** 1243-1257.

247. Ibey BL, Beier HT, Rounds RM, CotÃ© GL, Yadavalli VK, Pishko MV. Competitive binding assay for glucose based on glycodendrimer-fluorophore conjugates. *Analytical Chemistry* 2005, **77**(21)**:** 7039-7046.

248. Cummins BM, Li M, Locke AK, Birch DJ, Vigh G, Coté GL. Overcoming the aggregation problem: A new type of fluorescent ligand for ConA-based glucose sensing. *Biosensors and Bioelectronics* 2015, **63:** 53-60.

249. Kim JJ, Park K. Modulated insulin delivery from glucose-sensitive hydrogel dosage forms. *Journal of Controlled Release* 2001, **77**(1-2)**:** 39-47.

250. Kim JJ, Park K. Glucose-binding property of pegylated concanavalin A. *Pharmaceutical Research* 2001, **18**(6)**:** 794-799.

251. Wen Z, Niemeyer B. Preparation and characterization of PEGyated Concanavalin A for affinity chromatography with improved stability. *Journal of Chromatography B Analytical Technology Biomedical Life Science* 2011, **879**(20)**:** 1732-1740.

252. Bhat R, Timasheff SN. Steric exclusion is the principal source of the preferential hydration of proteins in the presence of polyethylene glycols. *Protein Science* 1992, **1**(9)**:** 1133-1143.

253. Sharma S, Popat KC, Desai TA. Controlling nonspecific protein interactions in silicon biomicrosystems with nanostructured poly (ethylene glycol) films. *Langmuir* 2002, **18**(23)**:** 8728-8731.

254. Rounds RM, Ibey BL, Beier HT, Pishko MV, Cote GL. Microporated PEG spheres for fluorescent analyte detection. *Journal of Fluorescence* 2007, **17**(1)**:** 57-63.

255. Aloraefya M, Pfeferb J, Ramella-Romana J, Sapsfordb K. Development and testing of a fluorescence biosensor for glucose sensing. Proc. of SPIE Vol; 2012; 2012. p. 83670H-83671.

256. Cheung KY, Mak WC, Trau D. Reusable optical bioassay platform with permeability-controlled hydrogel pads for selective saccharide detection. *Analytical Chemistry Acta* 2008, **607**(2)**:** 204-210.

257. Zhou QZ, Wang LY, Ma GH, Su ZG. Preparation of uniform-sized agarose beads by microporous membrane emulsification technique. *Journal of Colloid Interface Science* 2007, **311**(1)**:** 118-127.

258. Russell R, Pishko M, Gefrides C, Cote G. A fluorescent glucose assay using poly-l-lysine and calcium alginate microencapsulated tritc-succinyl-concanavalin A and FITC-Dextran. Engineering in Medicine and Biology Society, 1998. Proceedings of the 20th Annual International Conference of the IEEE; 1998: IEEE; 1998. p. 2858-2861.

259. Chaudhary A, Raina M, Harma H, Hanninen P, McShane MJ, Srivastava R. Evaluation of glucose sensitive affinity binding assay entrapped in fluorescent dissolved-core alginate microspheres. *Biotechnology and Bioengineering* 2009, **104**(6)**:** 1075-1085.

260. Peyratout CS, Daehne L. Tailor-made polyelectrolyte microcapsules: from multilayers to smart containers. *Angewandte Chemie International Edition* 2004, **43**(29)**:** 3762-3783.

261. Selina O, Belov SY, Vlasova N, Balysheva V, Churin A, Bartkoviak A, *et al.* Biodegradable microcapsules with entrapped DNA for development of new DNA vaccines. *Russian Journal of Bioorganic Chemistry* 2009, **35**(1)**:** 103-110.

262. Dahne L, Baude B. adsorbing active drug in porous templates, coating a primer layer and forming a capsule shell, alternately coating the charged poly-electrolyte layers and nanoparticle layers; sustained release; dosage forms; cosmetics; as diagnosis, sensors; water treatment. Google Patents; 2011.

263. Gaponik N, Radtchenko IL, Gerstenberger MR, Fedutik YA, Sukhorukov GB, Rogach AL. Labeling of biocompatible polymer microcapsules with near-infrared emitting nanocrystals. *Nano Letters* 2003, **3**(3)**:** 369-372.

264. Antipov AA, Shchukin D, Fedutik Y, Petrov AI, Sukhorukov GB, Möhwald H. Carbonate microparticles for hollow polyelectrolyte capsules fabrication. *Colloids and Surfaces A: Physicochemical and Engineering Aspects* 2003, **224**(1)**:** 175-183.

265. Gao G, Moya S, Lichtenfeld H, Casoli A, Fiedler H, Donath E, *et al.* The decomposition process of melamine formaldehyde cores: the key step in the fabrication of ultrathin polyelectrolyte multilayer capsules. *Macromolecular Materials and Engineering* 2001, **286**(6)**:** 355-361.

266. Donath E, Sukhorukov GB, Caruso F, Davis SA, Möhwald H. Novel hollow polymer shells by colloid-templated assembly of polyelectrolytes. *Angewandte Chemie International Edition* 1998, **37**(16)**:** 2201-2205.

267. Shenoy DB, Antipov AA, Sukhorukov GB, Mohwald H. Layer-by-layer engineering of biocompatible, decomposable core-shell structures. *Biomacromolecules* 2003, **4**(2)**:** 265-272.

268. Nanocs I. Amine Pegylation PEG Derivatives. 2014 [cited 2014 January 27]Available from: http://www.nanocs.com/PEG/APEG.htm

269. Stocks SJ, Jones AJ, Ramey CW, Brooks DE. A fluorometric assay of the degree of modification of protein primary amines with polyethylene glycol. *Analytical Biochemistry* 1986, **154**(1)**:** 232-234.

270. Heyduk T, Ma Y, Tang H, Ebright RH. Fluorescence anisotropy: rapid, quantitative assay for protein-DNA and protein-protein interaction. *Methods in Enzymology* 1996, **274:** 492-503.

271. Thompson RB, Maliwal BP, Feliccia VL, Fierke CA, McCall K. Determination of picomolar concentrations of metal ions using fluorescence anisotropy: biosensing with a “reagentless” enzyme transducer. *Analytical Chemistry* 1998, **70**(22)**:** 4717-4723.

272. Weatherman RV, Kiessling LL. Fluorescence anisotropy assays reveal affinities of C-and O-glycosides for concanavalin A1. *The Journal of Organic Chemistry* 1996, **61**(2)**:** 534-538.